Università
Ca'Foscari
Venezia

Master's Degree programme – Second Cycle
(*D.M. 270/2004*)
in Science and Technology of Bio- and Nano-materials

Final Thesis

Ca' Foscari
Dorsoduro 3246
30123 Venezia

SILICA NANOPARTICLES: SYNTHESIS, CHARACTERIZATION AND BIOMEDICAL APPLICATIONS

Supervisor
Ch. Prof. Riello Pietro

Co-Supervisor
Giulio Fracasso

Graduand
Giulia Glorani
Matriculation Number 842634

Academic Year
2013 / 2014

Ad Enrico,
animo speciale tra migliaia,
sul quale ho avuto la fortuna di inciampare,
un giorno di molti anni fa.

Come un baco da seta
veste il suo leggero involucro,
prima di diventare farfalla,
cosí tu indossi le tue ali,
grandi e variopinte,
in questo percorso di rinascita
che ti porterá ad esplorare mondi e luoghi
in cui solo fantasia ed immaginazione
possono davvero giungere.

Contents

Chapter 1

Introduction

1.1 Nanomedicine: an overview

The European Medicines Agency (EMA) defines the nanomedicine as the application of structures and devices, that have size between 0.2 nm and 100 nm, in order to make prevention, diagnosis, monitoring and treatment of different diseases [1].
The early concept of nanomedicine was born in 1959 from the idea that small nanorobots can be introduced into the human body, in order to perform cell healing and repairing [2]. Some years later, this idea was supported by Richard Feynman in his outstanding lecture "There's Plenty of Room at the Bottom". Feynman proposed "using machine tools to make smaller machine tools, these to be used in turn to make still smaller machine tools, and so on all the way down to the atomic level". After discussing with his collegue Albert R. Hibbs, Feynman explains some interesting applications of the small machines in the surgical field, such as their introduction into the blood vessels in order to have a look around heart diseases [3].
However, the applications of nanoparticles to the nanomedicine field are multiple and different, to name few: drug delivery, gene delivery, and molecular imaging [4]. In the next section I will briefly discuss these medical fields with a rapid insight about the applicability of nanotechnology to each of them.

1.1.1 Drug delivery

Drug delivery refers to the synthesis of technologies that transport pharmaceutical compounds, in order to achieve a specific therapeutic effect into the human body, related to treating, preventing, or monitoring the diseases. A drug delivery system is a complex system composed of two elements: a pharmaceutical active ingrendient and a nanoparticle that carries it to a specific site [5]. Compared to a common drug preparation, a drug delivery system is not affected by the first pass effect, in which the bioavailability of the drug is reduced by the hepatic uptake, leading to the need for the administration of higher drug doses to the patient. A complex system like that also allows to obtain prolonged

drug effect, steady drug plasma levels, and good stability of the drug in serum [6]. In the light of above, during the design of a drug delivery system, several features should be necessarily considered:

- Targeting system;
- Biocompatibility and toxicity;
- Circulation time;
- Stability;
- Biodistribution and clearance.

The creation of a targeting system can be achieved exploiting the passive mechanism of the Enhanced Permeability and Retention (EPR) effect or by an active mechanism. The passive mechanism of the EPR effect is a direct consequence of the anatomy and physiology of the tumor, which is quite different from the healthy tissues. In addition to a high vascular density, due to the overproduction of angiogenic factors, a solid tumor has large gaps between its blood cell vessels, shows a selective retention of drugs, and lack of a lymphatic recovery system [7, 8].

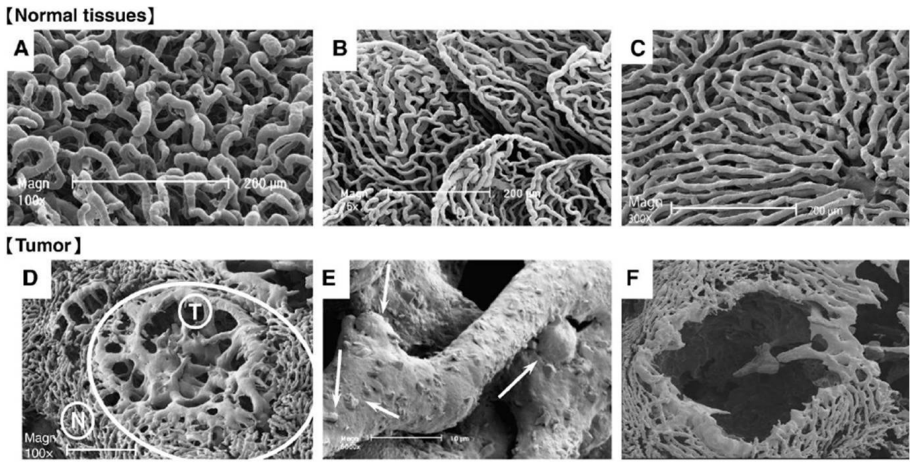

Figure 1.1: SEM images of blood vessels in healthy tissues (A-C) and cancer tissue (D-F). Images from A to C show the healthy tissues of pancreas, colon and liver. Images from D to F show a metastatic liver tumor, where "T" indicates the tumoral tissue, while "N" the healthy one [7].

Nanoparticles can be also actively targeted for the cellular binding, the intracellular transport, and the cellular uptake. Surface modifications and charge, nanoparticles size, and surface coating with polymers are factors influencing the drug targeting. In general, nanoparticles smaller than 20 nm are internalized into the cells without endocytic process [9]. The surface functionalization with polymers, like polyehtylene glycol (PEG), also improves an efficient internalization into the nuclear region and cytosol [5]. PEG is a compound prepared by the polimerization of ethylene oxide and could have different molecular

weight (MW), in a range between 100 Da and 20 000 Da. The MW is tightly related to the chain length, which determines the physical properties of the polymer, e.g. viscosity and melting point. On the contrary, the chemical properties of PEG are almost insensitive to its MW. Surface modification of nanoparticles with PEG, usually referred to as pegylation, also increases the half life in serum, tissue perfusion, and reduces the uptake by the reticuloendothelial system (RES) [10]. The RES, also referred to as Mononuclear Phagocyte System (MPS), is composed of all the cells which take part in the defense mechanisms of the human body. It involves three types of cells:

- Reticular cells;
- Macrophages;
- Kupffer cells.

The platforms employed as drug delivery systems during the last decades can be divided in two classes: organic and inorganic compounds. Organic compounds include immunoliposomes, in which a fragment of a monoclonal antibody (mAb) is conjugated to the liposome, micelles, polymeric nanoparticles (NPs), and dendrimers, while the inorganic compounds include gold NPs, superparamagnetic NPs, and carbon nanotubes [6, 11].

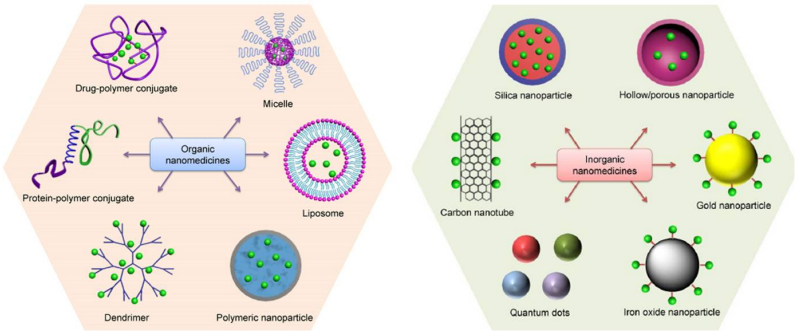

Figure 1.2: Two areas of nanomedicine for drug delivery. Reprinted from [11].

1.1.2 Gene delivery

Gene delivery refers to the introduction of genetic material into the cell, in order to alter, temporarily or permanently, the phenotype. A gene delivery system should allow to protect the genetic material to be delivered to the cell nucleus during its crossing of the cell barriers, making sure of the transcription of this deoxyribonucleic acid (DNA) cargo, as shown in figure 1.3 [12].

Differently from the common pharmaceutical preparations, hereditary and acquired diseases can be treated easily with this method. During the last decades, many gene delivery methods were developed and they can be conveniently divided into three classes:

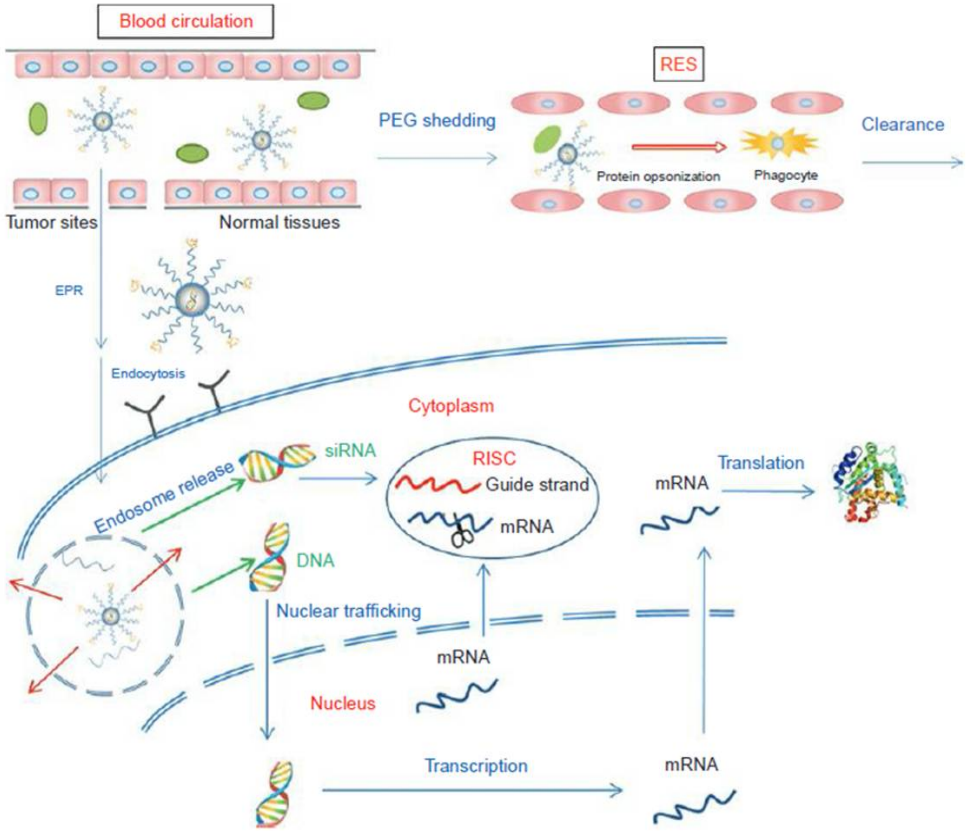

Figure 1.3: Scheme in which the in vivo cell barriers are depicted. Reprinted from [12].

- physical methods;
- viral vector based;
- non-viral vector based.

Needle injection, ballistic injection, electroporation, sonoporation, hydroporation, and magnetoporation belonged to the physical methods, in which a physical force is used to overcome the cell barriers. Virus based methods take advantage of a replication-deficient virus, which contains the gene of interest (GOI), like retroviral vectors, adenoviral vectors, and herpes simplex viral vectors. Non-virus based methods rely on the use of synthetic or natural compounds, like proteins and polymers. Compared to the virus based methods, they are less toxic, have low *i*mmunogenicity, and allow to introduce genes of different sizes [13]. Non-viral based method are employed in soft engineering [14], bone regeneration [15], and systemic applications [16].

1.1.3 Molecular imaging

Molecular imaging includes non-invasive, painless, and totally safe techniques which allow to visualize, quantify, and characterize physiological and pathological processes into the

human body. Differently from the traditional imaging, in which an excised tissue is analysed with the aid of a microscope, the molecular imaging allows to work at the cellular and subcellular level in a living patient. Furthermore, the early diagnosis before the onset of symptoms is possibile with these techniques. There are different imaging modalities:

- Optical imaging,
- Magnetic resonance imaging (MRI),
- X-ray computed tomography (CT),
- Positron emission tomography (PET).

They are used in the diagnosis of brain disorders, like Parkinson and Alzheimer, heart and bone diseases, kidney and thyroid disordes, cancer and much more.

Optical imaging

Optical imaging is an imaging technique in which ultraviolet, infrared, and visible lights are used, and includes bioluminescence and fluorescence. The detection limit of this technique can reach probe concentrations in the order of pico and femtomolar. Bioluminescence imaging refers to the internal light production following the oxydative reaction of the luciferin, while fluorescence imaging uses the external light in order to excite fluorescent molecules, like green fluorescent protein (GFP), or endogenous targets (collagen and hemoglobin). Data are quantified by the analysis of the region of interest (ROI) efficency and photon flux are measured. In order to analyse deeper tissues, a near infrared (NIR) technique is used. The NIR techniques exploit the spectral range also know as the therapeutic window (650 nm-900 nm), in which the molecular adsorption and the tissue autofluorescence are lower (figure 1.4), leading to an enhanced sensitivity of the imaging (theoretical dephts of 7 cm-14 cm, using a femtosecond technique) [17].

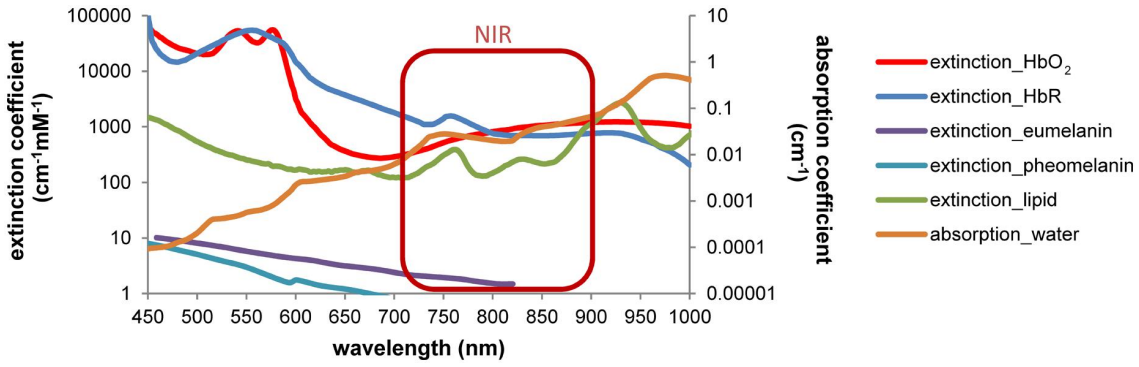

Figure 1.4: Light adsorption of the tissue in human body. Reprinted from [18].

During the last decades, a lot of organic fluorescent dyes were developed, but the emission in the visible part of the spectrum makes them useless for in vivo applications. In the light of the above considerations, inorganic dyes were synthesized, like quantum dots (QDs) and lanthanide complexes, mainly based on europium and terbium, which have long luminescence lifetime and a Stoke's shift higher than 200 nm. However, the inorganic dyes will be potentially toxic and have a complex surface chemistry [19].

Magnetic resonance imaging (MRI)

Magnetic resonance imaging is a technique in which an electromagnetic radiation is used. The patient is placed into the field generated by a large magnet, which causes the alignment of the spins of the atomic nuclei along the magnetic field direction. This process involves hydrogen as well, the most abundant atom in the human body. During the application of the external magnetic field a radio frequency (RF) signal is applied making the spins lose their alignment. The delay for the energy release, due to the regain of the initial orientation, is detected. All the atomic nuclei are composed of protons (positively charged), electrons (negatively charged), and neutrons (non-charged), which posses an intrinsic spin. Due to externally applied magnetic field, particles with net spin absorb a photon with a frequency ω_0, which is defined by the Larmor law:

$$\omega_0 = \gamma \times B_0 \tag{1.1}$$

where γ is the gyromagnetc ratio of the particles (for hydrogen $\gamma = 42.58\,\mathrm{MHz/T}$) [20].

After removing the magnetic field (B), the atoms nuclei relax to their initial energy state (figure 1.5) through two different pathways:

- T_2 trasversal relaxation (spin-spin);
- T_1 longitudinal relaxation (spin-lattice).

The description of these two pathways is beyond the scope of this thesis. It is sufficient to mention that in order to enhance the image contrast during the MRI exams, the relaxation time is altered through the use of a contrast agent, which can reduce or extend it. During the last decades, a lot of nanoparticles were developed for the MRI applications, like superparamagnetic iron oxide nanoparticles (SPIONs), gadolinium based contrast agents, FePt-Au nanoparticles, and magnetite nanocapsules [21].

X-ray computed tomography (CT)

X-ray computed tomography is a technique in which X-rays are used. Differently from the first CT scanners, which had a single photomultiplier detector and required long analysis

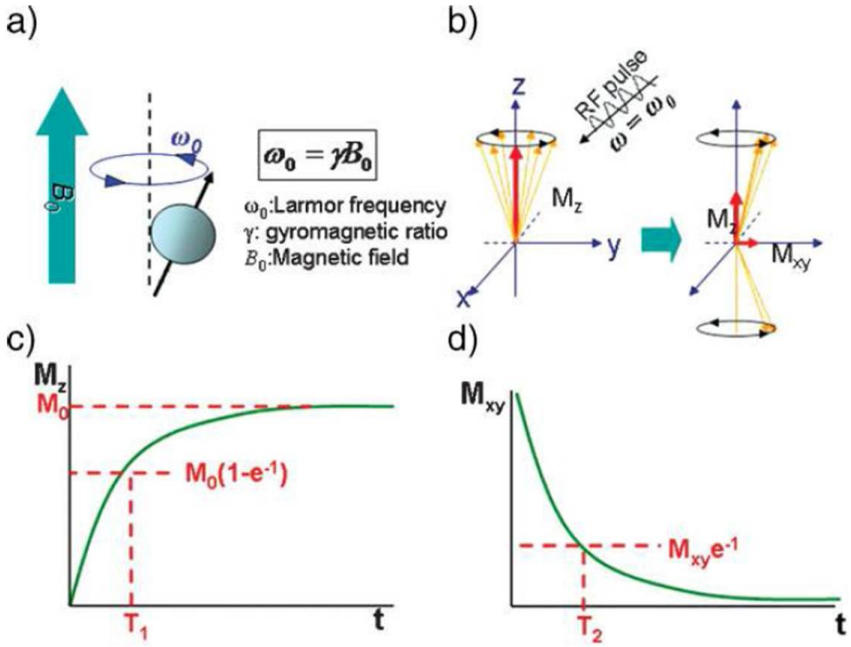

Figure 1.5: Magnetic resonance imaging (MRI) principles. a) Spin alignment under Larmor law. b) Changing in spins magnetization. c) Longitudinal and trasversal relaxations. Reprinted from [21].

time, today thin slices of the scanned object are swiftly acquired and then combined, in order to obtain a three-dimensional image. Bones and tissues absorb the radiation to a different extent, depending on the atomic number (Z), leading to a contrast, which is detected by CT technique. The advantages of CT are multiple:

- Rapid image acquisition;
- Clear images;
- Chance to scan a large portion of the human body.

In order to enhance the image contrast during the CT exams, heavy elements are used, which provide a high absorption cross section. A lot of nanoparticles were developed for the CT applications during last years. The first ones were the iodine based NPs, then the gold based agents and bismuth based agents. In some experiments also the bromine based agents were used, but they show weak contrast and low density of load. However, the NPs mentioned above, are well biocompatible and non toxic for the human body [22].

Positron emission tomography (PET)

Positron emission tomography (PET) is a technique in which a three dimensional image of the physiological process in the human body is obtained. The tracer, a compound in which one atom is replaced by a radio-isotope, is injected into the patient and, following

the positron emission decay, a pair of gamma rays is detected by a scintillator. Depending on the concentration of the tracer injected, the metabolic activity of different human tissues is shown in a three dimensional image. One of the most used active molecule during the PET exams is the fluorodeoxyglucose (FDG) - ^{18}F, which emits the radioactive isotope fluorine-18, detects the metabolic activity of the tissue, and is swiftly excreted by the patient. In a recent experimental work, lipid nanoparticles were used as diagnostic agents for the solid tumors visualization, because of their ability to encapsulate radioactive isotopes, specifically the ^{64}Cu-isotope [23]. During the last years, bromine-76, arsenic-64, and iodine-124 were also used as radionuclides in PET exams [24].

As described above, during the last decades a lot of nanoparticles for biomedical applications were developed. In the next section I will refer more specifically to one of them: silica NPs.

1.2 Silica Nanoparticles: the state of the art

1.2.1 Silica nanoparticles synthesis, features, and applications

Silica (SiO_2) is a silicon compound which is present in water as silicate ion $SiO_3{}^{2-}$, and in many biological structure, like diatomaceous and sponges. Because of its features, it is well suited for the NPs synthesis. Different synthetic approaches for the synthesis of porous or non porous silica NPs have been reported so far. Both porous and non porous display pros and cons, that can briefly summarized as follows.
The mesoporous silica NPs have pores from 2 nm to 50 nm, in which drugs and pharmaceutical preparations can be loaded efficently modifying the inner surface of these pores with suitable functional groups. These can also play a role in the controlled release of the cargo. Otherwise, a gatekeeper strategy can be applied. A gatekeeper can be a nanoparticle or a functional group which responds to different stimuli: pH, light, enzymes and temperature, in order to control the drug release. Drug delivery systems based on non-porous silica NPs can be obtained as well. The drug is encapsulated inside the nanoparticle or conjugated on the surface of it, as shown in figure 1.6 [11].
Non-porous silica NPs can be synthesized through a simple Stöber protocol [25], using cheap reagents, and non expensive facilities. The Stöber synthesis is composed of two steps, and takes advantage of an alkaline compound, usually ammonium hydroxide, as a catalyst:

- hydrolysis of organic silica precursors;
- condensation of silicic acid in alcholic solution.

The hydrolysis chemical reaction, in the case where the tetraethyl orthosilicate (TEOS) is used, is expressed as follows:

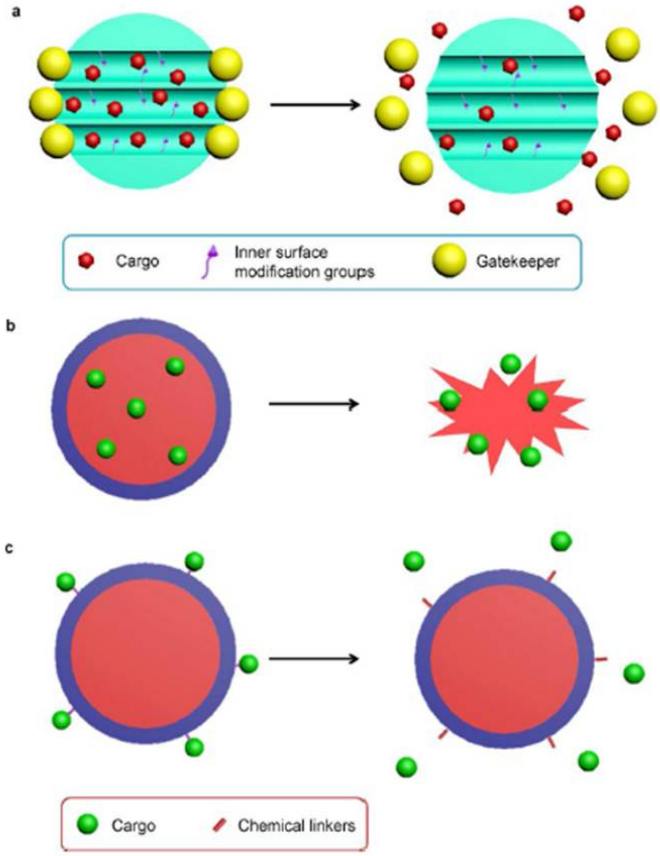

Figure 1.6: a) Mesoporous silica NPs loaded with drugs. b) Encapsulation of drugs in non-porous silica NPs. c) Conjugation of drugs on the surface of the non-porous silica NPs. Reprinted from [11].

$$Si(OC_2H_5)_4 + xH_2O \rightarrow Si(OC_2H_5)_{4-x}(OH)_x + xC_2H_5OH$$

The condensation reaction occurs immediatly after the hydrolysis, in which the hydroxyl groups of $Si(OC_2H_5)_{4-x}(OH)_x$ react with the ethoxy group of an other Tetraethyl orthosilicate (TEOS) molecule, in order to form the siloxane bridge Si–O–Si.
The complete chemical reaction, including hydrolysis and condensation, is expressed as follows:

$$\equiv Si{-}OC_2H_5 + HO{-}Si \equiv \rightarrow C_2H_2O_5 + \equiv Si{-}O{-}Si \equiv$$
$$\equiv Si{-}OH + HO{-}Si \equiv \rightarrow H_2O + \equiv Si{-}O{-}Si \equiv$$

Leading to the overall reaction:

$$Si(OC_2H_5)_4 + 2\,H_2O \rightarrow SiO_2 + 4\,C_2H_5OH$$

The size of the NPs can be controlled varying the ammonium hydroxide and TEOS contents in the reaction mixture. With the increase of the TEOS concentration, keeping the

ammonium hydroxide concentration fixed, the hydrolysis and condensation reactions become faster, leading to the formation of a less number of nucleation centers. As a result, silica NPs will be larger and less in number. The particles size increases also varying the ammonium hydroxyde amount, as shown in the SEM images of samples syntesized as a preliminary studies for this thesis (figure 1.7).

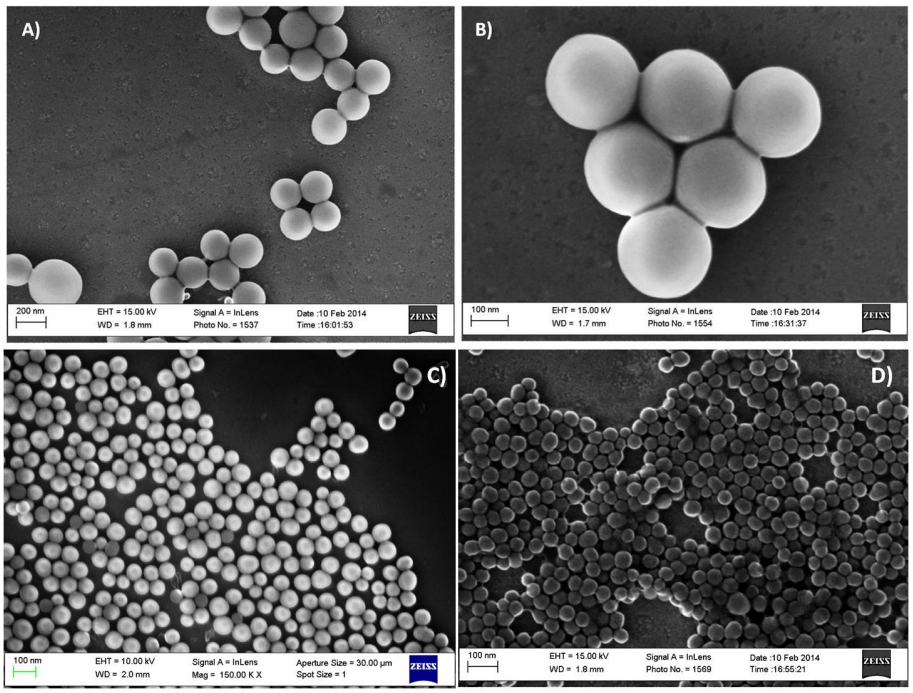

Figure 1.7: Different NPs sizes, varying the ammonium hydroxide concentration. A) Silica NPs of 220 nm, (experimental conditions: TEOS:NH_3:H_2O:EtOH=1:5:22:68). B) Silica NPs of 190 nm, (experimental conditions: TEOS:NH_3:H_2O:EtOH=1:8:20:68). C) Silica NPs of 100 nm, (experimental conditions: TEOS:NH_3:H_2O:EtOH=1:4:24:68). D) Silica NPs of 65 nm, (experimental conditions: TEOS:NH_3:H_2O:EtOH=1:2:25:68).

Also the shape of the silica NPs can be controlled using templates, leading to particles with longer blood circulation and tissues penetration [26]. Geng et al. demonstrated in their experimental work that worm-like micelles have longer circulation time than the spherical ones, because of their ability to escape from the phagocytosis. Moreover, due to the more efficient transport, the nanorods are able to penetrate the tumoral tissues faster than the spherical NPs.

Stöber silica nanoparticles were intensively studied during these decades, especially for their low toxicity, biocompatibily and biodegradability, which are some of the most important parameters to consider in the biomedical field. However the size and shape of silica NPs can easily influence the uptake and the biodistribution, as demonstrated by Gratton et al. in their experimental work [27, 28]. Another fundamental feature should be considered during the NPs synthesis: the surface chemistry, which is important for the

interactions with the biologycal systems, the internalization, the biodistribution, and the tissues penetration. Silica NPs surface can be easily modified, by adsorption or by covalent conjugation, exploiting the well-known silanes chemistry. The surface charge of the NPs can be easily changed (positive, negative or zwitterionic), and also a lot of polymers can be grafted on their surface, either chemically or physically, in order to achieve this surface modification.
To sum up the behavior of silica NPs in a biological system is mainly influenced by the following factors:

- Size;
- Shape;
- Surface chemistry.

In the next section I will briefly describe one of this parameters, that is to say the polymer grafting strategies on silica NPs surface.

1.2.2 Silica nanoparticles surface grafting with polymers

During the last decades, a lot of polymers were used in order to cover silica NPs surface and obtain the properties enumerated above: the poly(amidoamine), poly(urethane), poly(dimethylsiloxane), and vinyl polymers, to name a few [29]. Also the poly-L-glutamic acid was used for the same purpose, because of its biodegradability and the presence of the carboxyl groups, which can be modified in order to encapsulate organic biomolecules [30]. Another polymer which can be used for the NPs surface coverage is the poly(ethylen)glycol (PEG). PEG is an organic compound that is really useful for biological applications, because it allows to make the NPs stealth to the immune system, leading to an easier blood circulation of them [11]. In addition to promote the steric stabilization, the surface functionalization with PEG also allows to reduce or even avoid the opsonisation process and the macrophages uptake [31]. However, during the polymers grafting to the NPs, some parameters should be considered, in order to obtain a good coverage of the NPs surface:

- Chain length of the PEG;
- MW of the PEG;
- Chemistry of the PEG;
- PEG surface density.

Varying one of this parameters, the surface coverage of the NPs, their stability, and their stealth properties can be compromised [32].

Molecular weight and chains length of the polyethylene glycol

The PEG polymers have molecular weights (MWs) in the range between 100 Da and 20 000 Da and their physical properties can be different in response to the chains length, which can be indirectly indicated as the number of monomers in the chain (n= polymerization degree). At low values of n, the PEG is liquid and have low viscosity, while at high n, is solid and waxy. On the other hand, the chemical properties of the PEG are not influenced by this parameter. Also the NPs functionalization is affected by the polymerization degree of the PEG; Xu et al. in their experimental work demonstrate that using a higher MW PEG the proteins adsorption on the NPs surface is reduced [33].

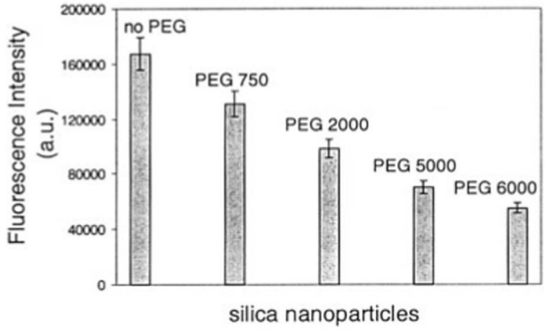

Figure 1.8: Proteins adsorption on bare and PEGylated silica NPs, derived indirectly from the fluorescence of the BSA-dye conjugated. Reprinted from [33].

Also He et al. reported the protein adsorption on the mesoporous NPs surface (150 nm ±20 nm). They show that the coverage density of mesoporous silica NPs is inversely proportional to the MW of the PEG used. Using different MWs PEG (from 4K to 20K) the chains density onto the outer surface of the NPs varies in a range between 0.05 wt % and 3.75 wt % [34].

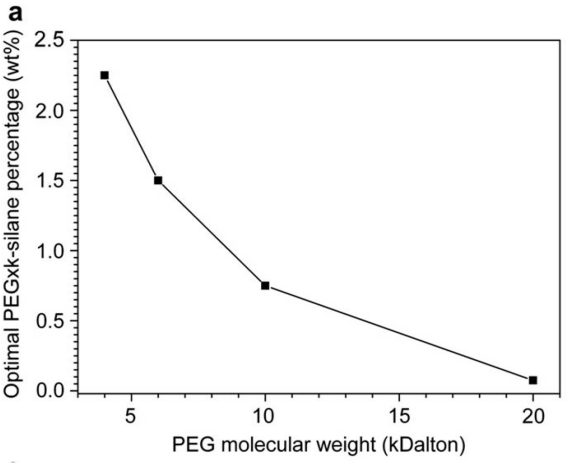

Figure 1.9: Graphical representation of the PEG-silane percentage versus the MW of it. Reprinted from [34].

Moreover, the MW of the PEG is important for the NPs steric stabilization. Differently from the low MW PEG, the high MW PEG create a thick layer around the NPs, leading to a better stability in solution [33]. However, PEG with long and flexible chains has a repulsion character, which is good for avoiding the cellular uptake, but can lead to a difficult bioconjugation, due to the chains interactions. All this considered, the stability of the NPs seems to be better obtained using a mixture of different molecular weights PEG [35]. Sadzuka et al. in their experimental work demonstrate that the functionalization of the liposomes surface with a mixture of PEG2000 and PEG500 (2:1) shows a maximun FALT (Fixed Aqueous Layer Thickness), that is to say the thickness of the adsorbed polymer layer. Because of the insertion of short chains PEG, the mushroom conformation of the PEG2000 on the liposomes surface became larger, leading to a better stabilization in solution.

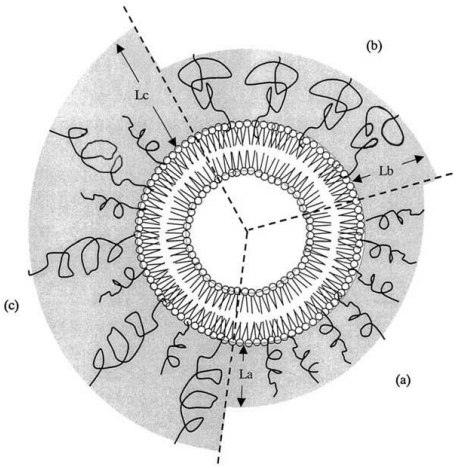

Figure 1.10: Representation of surface PEG-modifications. a) Single modification with short chains PEG. b) Single modification with PEG2000. c) Double modifications with short chains PEG and PEG2000. Reprinted from [35].

In general the stability of the NPs in solution, i.e. the colloidal stability, can be measured by a zeta potential analysis (ζ), in which the potential of the double electronic layer is evaluated. This analysis allows to obtain information about the surface charge of the NPs. During a zeta potential analysis, only a fraction of the total surface charge is measured, at the shear plane level, which is an imaginary plane placed next to the Stern layer (figure 1.11). Specifically, each charged particle of the colloidal suspension is surrounded by an oppositely charged ion layer, which is called Stern layer or fixed layer. Beyond this layer, there is a cloud of positively and negatively charged ions that together with the Stern layer ions forms the electrical double layer. The zeta potential is measured at this interface between the particles and the liquid in which they are dispersed. High values of zeta potential (both positive and negative) indicate a good colloidal stability, due to the electrostatic repulsion between the NPs, which avoid their aggregation. Conversely, low values of zeta potential lead to a poor colloidal stability, aggregation phenomena, and flocculation of the NPs. However, by covering the NPs surface with polymers, the stability

in solution is obtained through the steric hindrance, rather than the charge effect. Thanks to the surface convering with polymers, also the NPs having zeta potential close to zero are stable in solution. Manson et al. in their experimental work affirm that an increased amount of PEG on the NPs surface, dramatically enhance their stability in all media [36].

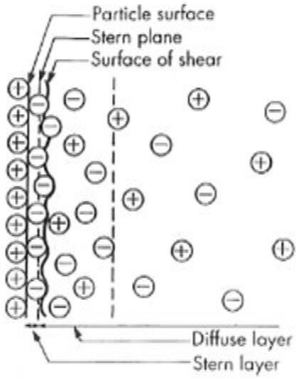

Figure 1.11: Schematic representation of the Stern layer.

Chemistry of the polyethylene glycol

The terminal ends of the PEG molecules grafted onto the NPs surface can influence the proteins binding. There are a lot of commercially available PEGs, having different terminal groups (shown in figure as R_2), like methoxy, alcohol or thiol terminus, to name a few.

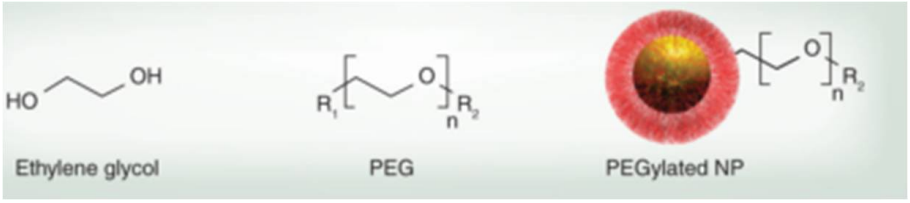

Figure 1.12: Schematic representation of PEG, in which there are the linkage groups (R_1) and the terminus groups (R_2). Reprinted from [37].

The negative charge on the NPs surface, like in the case of the carboxyl or the thiol terminus groups of the PEG, lead to fewer phagocytosis by the macrophages than the positive charge (amine groups). Also the hydroxyl terminus group is used to reduce the proteins binding onto the NPs surface.
Moreover, there are a lot of terminus groups which are used for the target binding, like the -maleimide, the -succimide, and the alkyl-reactive groups, to name a few. Using a PEG with these terminal ends, the click chemistry, the amine group, and the thiol group can be used to obtain the selective binding to the target [37].
In general, NPs which have negative or neutral charge, show a lower cellular uptake than

the positively charged ones. Moreover, the latter ones have a short half-life in the blood stream [38].

Polyethylene glycol surface density

The density of the PEG chains is defined as the number of the surface groups, calculated in a reference area. In general, the pegylation density is described by the size of an expandend chain, also known as the Flory radius (R_f), by the distance of the PEG chains (D) or the length of them (L) [39]. The Flory radius (R_f), can be calculated as follows:

$$R_f = (aN)^{3/5} \tag{1.2}$$

where a is the size of the monomer units of the PEG;
N is the number of the monomer units of the PEG.

Depending on the surface density, different chains conformations can be assumed by the PEG. At low density, where D is greater than R_f, the molecules of PEG are organized into a mushroom conformation, in which the chains are folded back on themselves. Conversely, at high density, where D is minor than R_f, a brush conformation is assumed by the PEG chains, which allows a lower packing density, and a better steric repulsion of the proteins. When L is greater than $2R_f$, a dense brush conformation can be obtained [40].

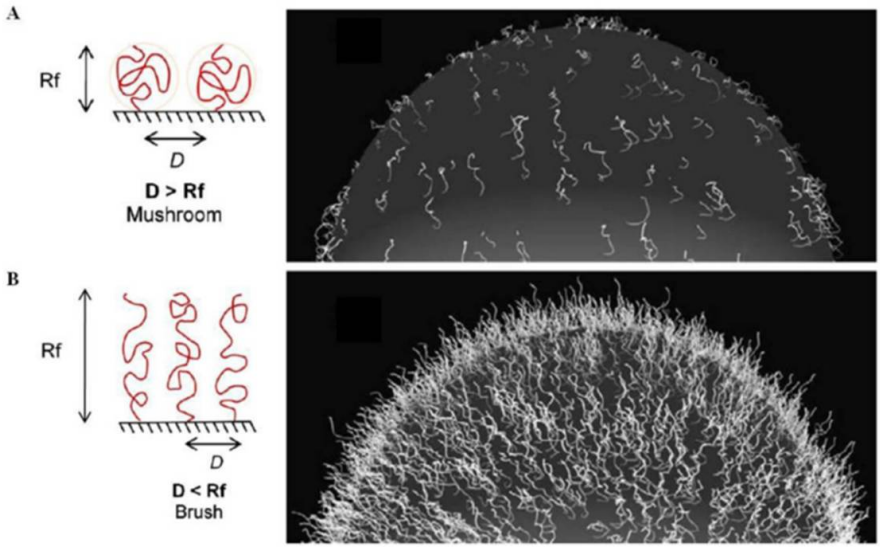

Figure 1.13: Different PEG conformations, brush (B) and mushroom (A). R_f represents the volume occupied by a single PEG chain. Reprinted from [41].

In spite of the advantages described above, both of these conformations have some disadvantages: the mushroom conformation can possibly lead to the presence of some holes in the surface covering, while the brush one may be able to reduce the binding affinity

towards the molecular targets [42]. As a general rule, in order to obtain a good pharmacokinetic and biodistribution, the PEG shell should be smaller than the 10 % of the nanoparticle (NP) diameter.

Definitively, in order to obtain a NP for the biological applications, the MW of the PEG used, its surface density, and its terminus groups, should be considered. In the next section I will briefly describe the effect of the pegylation towards the proteins adsorption, and the immune system response.

1.3 Immune system: a general view

In order to understand the "in vivo" NPs behavior, during the last decades, the relationship between the NPs surface and the adsorbed proteins on it, and also the immune system response towards them were deeply studied. There are a lot of proteins in the human organism and particularly in the body fluids: plasmatic proteins and serum proteins, among these the albumin is the most expressed protein. It is worth nothing that a complex protection system against the "non-self" compounds is put in place by the immune system. In addition to the tissues barrier, which prevents the entry of "non-self" entities, also the immune cells in the bloodstream, such as the leukocytes, the platelets, and the phagocytic cells, have a propensity to eliminate the "non-self" NPs.
After the injection, the inhalation, or the ingestion of NPs, an interaction among them, the plasma proteins, and the blood proteins, is triggered which can cause changes in the cellular uptake, biodistribution, drug delivery efficiency, and phagocytosis. The formation of a shell corona on the NPs surface, due to the interactions with these proteins, can change the NPs physical-chemical properties, leading to different "in vivo" behaviors [43].

Moreover the human immune system has developed an efficient method to mark the "non-self" compounds, whose surface is decorated by the opsonins, which enhance the phagocytic process. The opsonins family includes a lot of macromolecules, especially the antibodies (IgG) and the molecules which activate the complement system, an important component of the innate immune system. The complement system is composed of about twenty proteins; they interact reciprocally and with the cell membranes, enhancing the lysis of cells whose membrane is tagged by the complement proteins.
Before the opsonins binding, the membrane of the phagocytic cells and the targets are both negatively charged, avoiding their interaction. When the target is decorated by the opsonins, the charge on its surface is masked, leading to an easier phagocytic process. Moreover the opsonization process, the reaction with the antibodies or the complement activation, improve the phagocytosis of the "non-self" entities, because the phagocytic cells express three types of receptors to increase their scavenger properties:

- Receptor for opsonin molecules;
- Receptor for activate complement;
- Receptor for the Fc region of the antibodies.

An antibody (Ab), is a "Y"-shaped molecule, composed by four chains: two heavy chains and two light chains, linked by disulfide bonds. Each heavy chain can be divided in two regions: the constant region, which is identical for all the Ab, and the variable one, as shown in figure 1.14. The arms of the "Y" include the regions that bind the antigens, called the Fragment antigen binding (Fab). On the other hand, the base of the "Y" contains the Fragment crystallizable region (Fc), which modulates the immune cell activity.

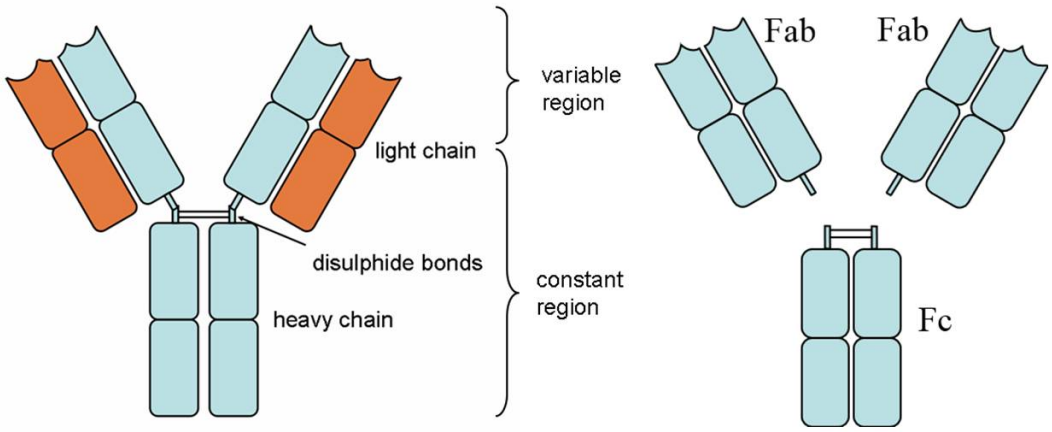

Figure 1.14: Schematic representation of an antibody and their domains.

An Ab binds an epitope of the antigen; specifically, the FAb portion of the Ab binds the antigen, while the Fc portion binds the receptor onto the phagocytic cell surface. This type of bond is also enhanced by the complement molecules (C3b), which are deposited onto the "non-self" compound surface, promoting the phagocytosis and the distruction process (figure 1.15). However, the "non-self" elements can also be destroyed following a different pathway, in which the bond between the Ab and the effector cells (neutrophilis and eosinophilis), lead to the production of lysis products.

As stated in Ref. [44] by Aggarwal et al. "Generally, hydrophobic particles are opsonized more quickly than hydrophilic particles, due to the enhanced adsorption of plasma proteins onto the surface of hydrophobic particles" [44]. Aggarwal et al. compared in their experimental study a less hydrophobic copolymer, composed by a molar ratio of 85:15 NIPAM/BAM (poly(N-isopropylacrylamide) /Aluminum magnesium boride), with its more hydrophobic counterpart (50:50). The first does not seem to adsorb proteins, except for a

little amount of albumin, while the second one binds the apolipoproteins and the fibrinogen.

In the light of above, a meticulous study of the proteins adsorption onto the NPs surface, and of the parameters affecting it, is demanding. In the next sections I will briefly describe the most important binding proteins, like the albumin and the other serum proteins. I will also describe the formation mechanism of a biomolecules layer around the NPs, also known as the protein corona complex, which can alter the size and the surface composition of the a nanomaterial [45].

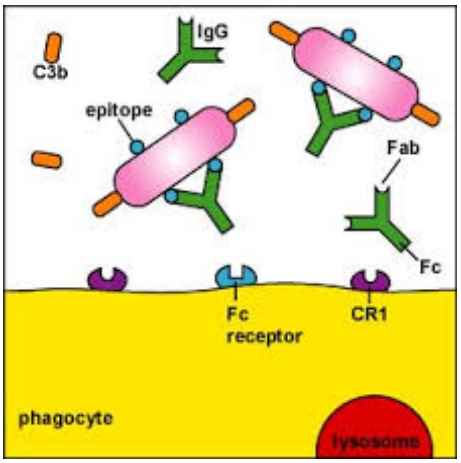

Figure 1.15: Schematic representation of the opsonization process.

Protein Corona complex

As described above, the corona complex formation is due to the biomolecules adsorption to the NPs surface. The most abundant biomolecules in the human body which display adsorbing capabilities are the proteins and the lipids. The adsorption mechanism is guided by the binding affinity between the NP and the proteins, in the same way of the protein-protein bond. Depending on the affinity, the proteins bond can be strong (hard corona) or weak (soft corona). However, the protein corona complex is not a fixed layer but its composition, can be influenced by the rate of desorption and adsorption of the molecules (figure 1.16). As a rule of thumb, the most abundant plasma proteins are firstly adsorbed on the NPs surface, followed by their replacing with the lower abundant proteins, which have, however, higher affinity.
The size of the proteins, their surface chemistry, and the concentration, can influence the thickness of the protein corona layer. Because of the size of the plasma proteins (3 nm-15 nm), Simberg et al. proposed a protein corona model composed by multiple layers, consisting of the primary binders and the secondary binders [46]. The former ones are directly bound to the NPs surface, while the latter ones are bound to the NPs, via protein-protein interactions. The presence of the secondary binders prevents the interactions with the surroundings and can influence the behavior of the primary binders, or even masks them.

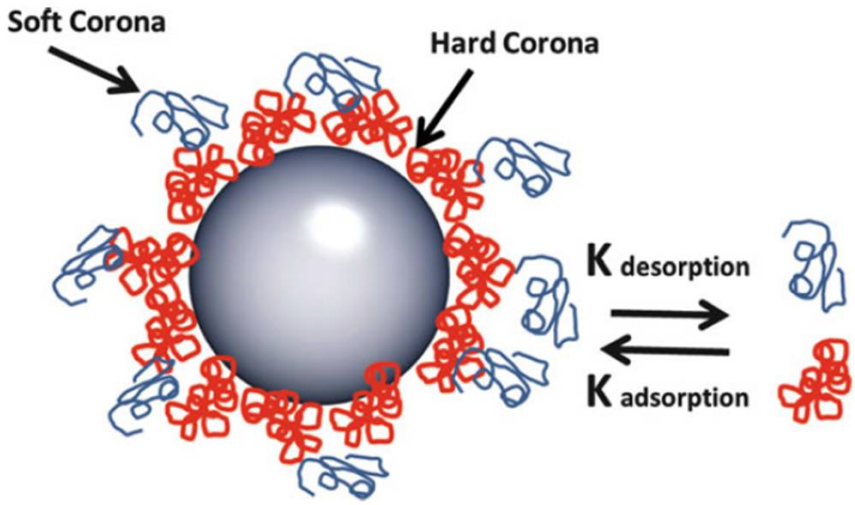

Figure 1.16: Schematic representation of the corona proteins (soft and hard).

An adsorption process can be divided in two steps:

- The early stage;
- The late stage.

The fibrinogen, the IgG, and the albumin adsorption are involved in the first stage, and they are replaced by the coagulation factors and the apolipoproteins in the second one. This sequential adsorption is partly due to the high dissociation rate of fibrinogen and albumin, and partly due to the slow dissociation rate of apolipoproteins.

Albumin and human serum

Mass spectroscopy analyses on NPs soaked in biological media have revealed that the albumin (figure 1.17) is one of the most abundant compounds of the protein corona layer ($3,5$ g/dl - $5,5$ g/dl) [47, 48]. Bovine Serum Albumin (BSA) is a water-soluble monomeric protein, composed of 583 aminoacids and having MW of about 66 KDa. "BSA contains tryptophan residues, which makes it absorb and fluoresce light at characteristic wavelengths. These characteristics are useful for studying protein binding using spectroscopic measurements." [49]. BSA behavior and structure depends on multiple interactions such as the hydrogen bonding, Van der Waals forces, electrostatic interactions, and the hydrophobic effect. Moreover, some reactions on the BSA surface, can alter the secondary structure, as described in Tsai et al. experimental work: "In addition, the reaction of the free thiol on the external surface of globular (N form) BSA with the AuNP surface could potentially weaken or alter the tertiary or secondary structure of the BSA molecule, which would likely result in the unfolding of BSA from its compact, globular structure." [50].

Because of its isoelectric point (Ip<5.5), the albumin mainly adsorbs on positively charged NPs, as described by Marsalek in his experimental work. Marsalek studied the BSA bond to the cerium oxide NPs (positively charged), which is enhanced at acidic pH. On the other hand, the negatively charged NPs better adsorb proteins with an isoelectric point higher than 5.5 (i.e. the IgG) [44].

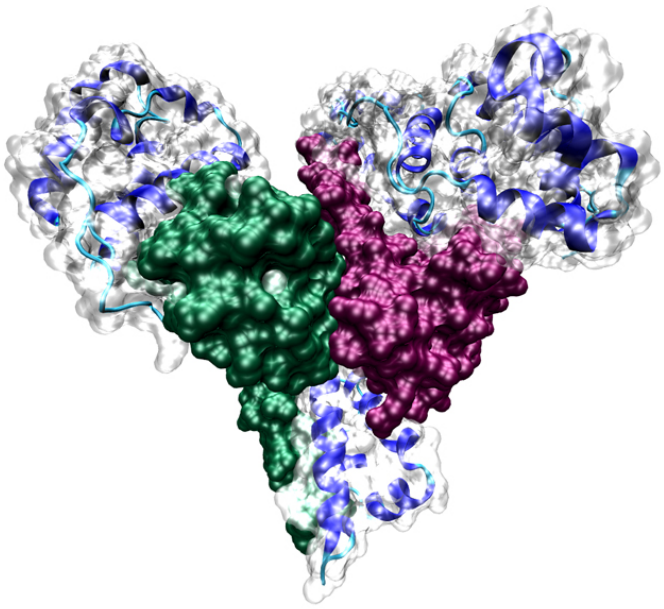

Figure 1.17: Schematic three-dimensional representation of human serum albumin.

As said in the previous section, when a material enters a biological enviroment, the initial event is the protein adsorption. The composition of the protein layer, the amount of the protein, and the conformational changes can influence the tissues response against the materials. Moreover protein adsorption can modulate the toxicity of some NPs. The specific bound proteins can affect the NPs biodistribution, the internalization process, the ζ potential, and also enhance the macrophages recognition. Rezwan et al. in their experimental work studied the interaction between some metal oxide particles (alumina, silica, titania, and zirconia) and albumin. In this study the zeta potential of the NPs, and their isoelectric point, are changed by the albumin adsorption [51]. Moreover, the adsorption of BSA can influence the NPs stability in solution. Shi et al. in their experimental work affirm that gold NPs can be stabilized in phospate buffer (PBS) after BSA adsorption. They observed also that after the binding to gold NPs, the secondary structure of BSA is altered, leading to a less compact structure. Then the solvent can penetrate the BSA cavity, increasing the polarity of the microenviroment around Trp-122 residue [52].

However the proteins adsorption onto the NPs has some disadvantages. Because of the bonds with fibrinogen and IgG, actually the NPs accumulate into the RES organs, specifically the liver and the spleen. As demonstrated by Liu et al. in their experimental work, the NPs accumulation is due mainly to the proteins, which increase the hepatocyte and

macrophage uptake [53]. On the other hand, the albumin bond seems to prolong the blood circulation time [54, 55]. Moreover, recent studies have shown that the patients with albuminuria are prone to develop a thrombotic attack [56].

It is therefore clear that a great amount of proteins adsorbed onto the NPs surface is not always good. In order to avoid excessive proteins adsorption, a pegylation step after the NPs sythesis is required. In the following section I will briefly describe the pegylation effects on the protein adsorption.

Nanoparticles pegylation and proteins adsorption

As described in the previous sections, the surface covering with PEG molecules not only promotes the internalization process, improves the stability and makes the NPs stealth, but also limits the proteins adsorption and the phagocytic process. During the last decade, a lot of pegylation methods were developed. One of the first pegylation reports studied the attachment of two different MWs PEGs to BSA and liver catalase. In this study mPEG-1900 and mPEG-5000 were covalently attached to the protein described above, with the use of the coupling agent 2,4,6-trichloro-s-triazine [57]. After the PEG attachment, mice better tolerate multiple injections of the catalase, suggesting the possibility to use the pegylation in enzyme therapy. Some years later, Li et al. demonstrated that the half-time circulation of latex particles can be enhanced using a PEG coating. A PEG with MW higher than 5000 kDa is used to pegylate the particles, leading to a 40-times longer circulation time in rats [58]. In 1999, Petros et al. used a pegylated liposomal delivery vehicle in order to transport the doxorubicin into the human body. This system, called Doxil®, enhanced the doxorubicin bioavailability of about 90-times [59]. Because of the large sizes of the liposomes, some years later pegylated poly(lactic-co-glycolic acid) (PLGA) NPs, were synthesized by Park and collegues. They demonstrated that coating the NPs with PEG, the circulation is enhanced and also the doxorubicin cardiotoxicity is dramatically reduced [60].
Also the silica NPs pegylation was studied during the last decades. Gu et al. synthesized a delivery doxorubicin system, in which mesoporous silica NPs are used. Using a silane-free chemistry, a PEG-galactose is attached onto the NPs surface, while the inner surface of the silica, is used to load the doxorubicin. Due to the thick PEG layer, this type of NPs are shielded from the proteins adsorption [61]. Moreover the pegylation also affect the NPs capture by the organs. Actually, He et al. demonstrate that pegylated mesoporous silica NPs escape more easily from the capture by some organs: such as the spleen, the lung, and the liver. In addition they have prolonged blood circulation time, and are more slowly excreted in the urine [62].

However, the PEGylation is not the standard procedure for avoiding the proteins adsorption and the escape from the RES capture. “It has some limitations. Although the common belief is that PEGylation can prevent immune recognition, recent studies have suggested

that the PEGylated nanoparticles would induce production of specific anti-PEG IgM that is responsible for accelerated blood clearance (ABC) of nanoparticles after repeated injection. It also results in hypersensitivity reaction by complement cascade activation in blood." [63].

Definitively, a lot of studies around the NPs synthesis and pegylation should be done, in order to reach the perfect optimum between the biological applications and the organic synthesis. Also the temperature effects on the synthesis, the purification step, the reaction time, and the molar ratio of different MWs PEG should be study.

1.4 Aim of thesis

This work will focus on the complete characterization, from a physo-chemical and biological point of view, of non-porous silica NPs either pegylated or not. Silica NPs are prepared using the one-pot protocol, in which the synthesis and the pegylation steps are carried out together, without the intermediate washing step, leading to bare and pegylated NPs from the same reation mixture. Using the same method, also bare and pegylated NPs incorporating different dyes were synthesized.
In order to evaluate the optimum method to cover the NPs surface with PEG, different MWs PEGs are used. Specifically a high MW PEG (mPEG-silane 5000) and a low MW PEG (mPEG-silane 550) are used, in order to check the effect on the stability, protein adsorption, and viability of the NPs.

The NPs are physically and chemically characterized. In order to check the different amount of PEG attached onto the samples surface, thermogravimetric (TG) and differential scanning calorimetry (DSC) curves are acquired. Moreover, to confirm the PEG grafting onto the NPs surface, and also to evaluate the complete removal of the organic solvents, infrared spectroscopy is used. In order to check the fluorescence of the NPs synthesized the emission and the absorption spectra were acquired.
The size, the shape, and the size distribution of the NPs are of paramount importance for the biological applications, and here they are evaluated using scanning electron microscope (SEM) and small angle X-ray scattering analyses. Using a colorimetric assay (the molybdate assay) also the dissolution rate of bare and pegylated NPs is evaluated.

Concerning the biological characterization, the viability, the proteins adsorption, and the macrophages uptake of the NPs are evaluated. Specifically, samples pegylated with different MWs PEG and different amount of it, plus the bare silica NPs, are tested. The viability assay test are conducted on three different cell lines: healthy cells, cancer cells, and fibroblast, in order to evaluate the different response against the NPs. Moreover, wanting to understand the different behavior of pegylated and bare NPs against the protein adsorption, BSA and human serum proteins adsorption are evaluated. In order to evaluate the macrophages uptake, fluorescent bare and pegylated NPs were analyzed using flow cytometry.

Chapter 2

Experimental Part

2.1 Materials

Reagent	**Supplier**	**Purity** %	**Density** g/cm^3	**M.W.** u.m.a.
Ammonia	Fluka	28	0.9	17.03
TEOS	Aldrich	98	0.933	208.33
Ethanol	Fluka	99.8	0.789	46.07
Poly(ethylene glycol) methyl ether (mPEG)	Aldrich			550
Poly(ethylene glycol) methyl ether (mPEG)	Aldrich			5000
Dibutyltin dilaurate (DBTL)	Aldrich	95	1.066	631.56
3-isocyanatopropyl triethoxysilane (IPTS)	Aldrich	95	0.99	247.36
Toluene	Fluka	> 99	0.867	92.14
Tetrahydrofuran (THF)	Sigma	>99.9	0.89	72.11
Cyclohexane	Fluka	99.5	0.81	84.16
Sodium hydrogen phospate	Aldrich	> 99	1.68	141.96
Sodium dihydrogen phospate	Aldrich	1.7	99	140.95
Amino-naphthol-sulfonic acid	Aldrich	> 90		239.25
Sodium sulfite	Aldrich	98	2.63	126.04
Sodium hydrogen sulfite	Aldrich	98	1.48	104.061
4-Amino-3-hydroxy-1-naphthalenesulfonic acid	Aldrich	> 90		239.25
Ammonium molybdate (VII)	Sigma	83	2.498	1235.86
Oxalic acid	Sigma	> 99	1.9	126.07
Hydrocloric acid	Merck	37	1.19	36.461
Sodium silicate solution	Sigma	27	1.39	
Acrylamide/Bis	Bio-Rad	30 (1:9)	1.13	71.08
Comassie staining	Bio-Rad			
Sodium dodecyl sulfate (SDS)	Sigma	99	1.01	288.38
Ammonium persulfate (APS)	Sigma	98		228.20
N,N,N',N-tetramethylethylenediamine (TEMED)	Sigma	99		116.20
BSA	Sigma	>96	0.775	66.000
Fetal bovine serum (FBS)	Lonza			
Rodamine 590	Aldrich	95		479.02
Coumarin 6	Aldrich	> 99		350.44
$Ru(bby)_3Cl_2$*$6H_2O$	Aldrich	99.5	748.62	

Table 2.1: Reagents and solvents used in the experimental part of the thesis.

Cell line	Cell type	Supplier
RAW 264.7 murine macrophages	cancer cells	ATCC
HEK 293 human embrional kidney	healthy cells	ATCC
Human fibroblast	healthy cells	derived from a primary culture

Table 2.2: Cells lines used for the biological test.

2.1.1 Cells culture and storage

RAW 264.7 is a murine macrophage cell line derived from an ascites of an Abelson murine leukaemia virus-induced tumor; HEK 293 cells originate from human embryonic kidney. Fibroblasts derived from a primary culture. All the cell lines used were cultured in DMEM, containing glucose (4.5 g/L) and sodium bicarbonate. The medium was supplemented with 10 % heat-inactivated FBS, streptomycin (10 mg/ml, penicillin G (100 units/ml)), L-Glutamine (2 mM) and HEPES (0.01 M). Then the cells were maintained in culture flasks at 37 °C, in a humidified atmosphere with 5 % of CO_2.

2.2 Methods

2.2.1 Nanoparticles synthesis

mPEG-silane 5000 **synthesis**

The synthesis was adapted from Jo et al. [64], with slight modifications. In a round bottom flask 35 g of mPEG 5000 (7 mmol) were added and stirred at 90 °C for 3.5 hours under vacuum. To the reaction mixture 40 ml of toluene, 1.3 ml of IPTS (10.5 mmol) and 0.43 ml of DBTL (0.7 mmol) were added. After adding chemical reagents the mixture was stirred for 48 hours under nitrogen atmosphere. Then 150 ml of n-hexane were added to make PEG precipitate. The white precipitate was filtered with a gooch filter (porosity G5) and washed with cold hexane. The product was purified by means of recrystallization from THF and cyclohexane (1:4).

mPEG-silane 550 **synthesis**

The synthesis was carried out in the same way as reported above, except for the fact that 7.58 ml of mPEG 550 (15 mmol), 3.74 ml of IPTS (30 mmol) and 0.924 ml of DBTL (1.5 mmol), were used. The purification step was also the same, except for the THF:cyclohexane ratio which was 1:9. The synthesis is shown as follows, in figure 2.1.

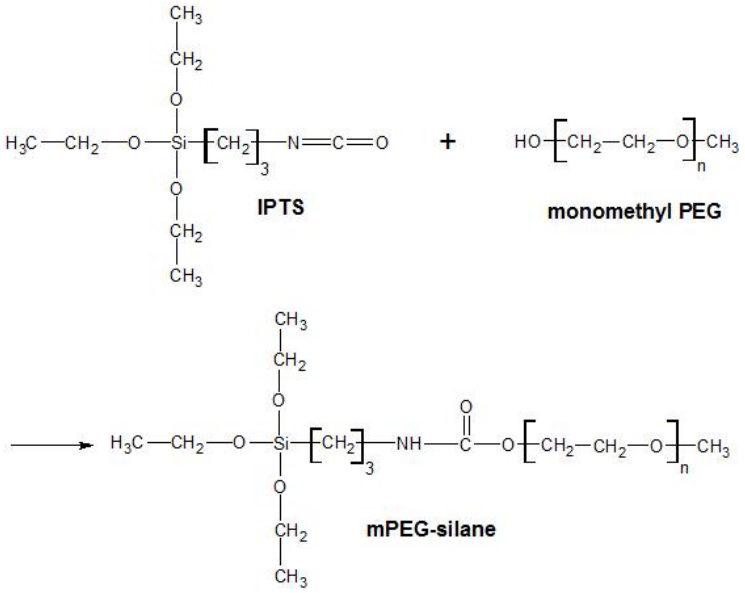

Figure 2.1: Representative scheme of mPEG-silane synthesis.

ONE POT SYNTHESIS AND PEGYLATION

Silica nanoparticles synthesis (for 500 mg)

Silica nanoparticles were synthesized through a modified one-pot Stöber synthesis [25]. In a round bottom flask 30 ml of ethanol and 1.9 ml of TEOS (0.009 mol) were introduced and the mixture was stirred for 10 minutes at room temperature. A solution of 0.25 ml of ammonium hydroxide (28 %) (0.014 mol) in 7.5 ml of distilled water was swiftly injected in the round bottom flask and the mixture was stirred continuously for 24 hours. In order to obtain bare and pegylated silica NPs from the same batch, after 24 hours the reaction mixture was split in two aliquots. The first one was collected by centrifugation (20000 g for 45 minutes) and washed once with ethanol and twice with water. Then silica NPs were resuspended in a known amount of water and stored at 4 °C for further usage and characterization. The second aliquot of the reaction mixture was pegylated, as described in the next paragraph. The scheme of the reaction is shown as follows in figure 2.2.

Silica nanoparticles pegylation with mPEG-silane (for 500 mg)

In order to obtain pegylated silica NPs, a known amount of different MW mPEG-silane was added to the pristine silica NPs suspension obtained after 24 hours of reaction and further stirred for 24 hours. After this time, the precipitate was collected by centrifugation (20000 g for 45 minutes) and washed once with ethanol and twice with water. Then silica NPs were resuspended in a known amount of water and stored at 4 °C. One batch of bare silica NPs and three batches of pegylated silica NPs, from the same synthesis, were prepared:

- Bare silica NPs;
- Silica NPs pegylated with mPEG-silane 5000 (table 2.3);
- Silica NPs pegylated with mPEG-silane 550 (table 2.4);
- Silica NPs pegylated with mPEG-silane 5000 and 550 (table 2.5);

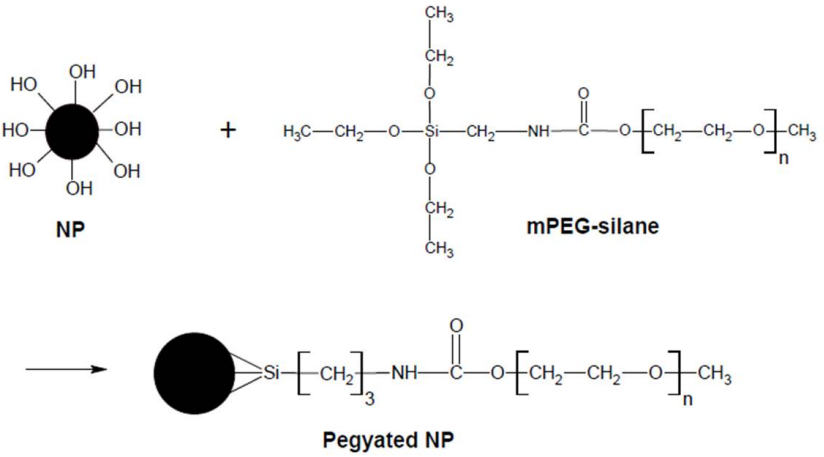

Figure 2.2: Representative scheme of silica NPs pegylation.

Sample	Amount of mPEG-silane 5000 (mg)	Molar ratio mPEG-silane 5000 ($mmol$)
S2y800a	800	0.152
S2y500a	500	0.095
S2y200a	200	0.038
S2y100a	100	0.019
S2y50a	50	0.095
S2y25a	25	0.0475

Table 2.3: Known amount of mPEG-silane 5000 added to 550 mg of NPs.

Sample	Amount of mPEG-silane 550 (mg)	Molar ratio mPEG-silane 550 ($mmol$)
S2y120b	120	0.152
S2y75b	75	0.095
S2y30b	30	0.038
S2y15b	15	0.019
S2y8b	8	0.095
S2y4b	4	0.0475

Table 2.4: Known amount of mPEG-silane 550 added to 550 mg of NPs.

Sample	Amount of mPEG-silane 5000 (mg)	Amount of mPEG-silane 550 (mg)	Molar ratio mPEG-silane 5000 ($mmol$)	Molar ratio mPEG-silane 550 ($mmol$)
S2y100a0b	800	/	0.152	/
S2y75a25b	600	30.8	0.114	0,038
S2y50a50b	400	61.6	0.076	0.076
S2y25a75b	200	92.45	0.038	0.114
S2y10a90b	79.9	110.9	0.0152	0.140
S2y0a100b	/	123	/	0.152

Table 2.5: Known amount of mPEG-silane 5000 and 550 added to 500 mg of NPs.

Fluorescent silica nanoparticles synthesis

Silica NPs were synthesized and washed through the same Stöber approach, described above. In order to make the NPs fluorescent, three different dyes (table 2.6) were added to the reaction mixture, to a final concentration of 0.1 mM. The product was washed with water and recovered by centrifugation, at 20000 g for 45 minutes, until the dye was completely removed from the surnatant. This was checked by analyzing the absorption spectra of the surnatant after each washing cycle.

Dye	Molecular weight (g/mol)
Rhodamine 590	479.02
Coumarin 6	350, 44
$Ru(bby)_3Cl_2$*$6H_2O$	748.62

Table 2.6: Dyes used to make the NPs fluorescent.

2.2.2 Nanoparticles characterization

For the thermogravimetric (TG) analyses a Netzsch STA 409 was used. The analyses were performed in air and nitrogen (air flow rate 40 ml/min, nitrogen flow rate 80 ml/min) with a scan rate of 20 °C/min in a range between 40 °C and 1000 °C.
For the SEM analyses a Zeiss sigma VP microscope was used. Samples were prepared diluiting 5 µl of NPs suspension to 995 µl of ethanol. The solution was sonicated for 15 minutes and one drop was deposited on a silicon wafer allowing the solvent to evaporate prior to observations. The images acquired were then processed using ImageJ, which allows to calculate the distribution of the NPs areas (nm^2), evaluating the contrast of each image. Specifically, the image acquired was imported into the graphical interface of the program, converted to a black and white image, and then grey amount was evaluated. For each sample, a statistical average of ten NPs were analyzed.
The infrared spectra were recorded with a NEXUS-FT-IR instrument implementing a

Nicolet AVATAR Diffuse Reflectance accessory. 500 µl of NPs solution were dried on a heating block, in order to let the water evaporate and 20 mg of NPs were used for the IR analyses. The spectra were recorded between 500 cm^{-1} and 4000 cm^{-1}, using a resolution of 2 cm^{-1} and 64 cycles of aquisition.
The diffraction pattern was recorded with a Small angle X-ray scattering (SAXS) Kratky camera (Cu Kα = 0.154 nm equipped with a proportional detector for intensity recording. The samples were prepared by adjusting the concentration to approximately 20 mg/ml. The suspension was introduced in a glass capillary (1.5 mm internal radius). Data were acquired as a function of the scattering vector modulus $h = (4\pi \times sin\theta)/\lambda$, where 2θ is the angle between the incident and the scattered beams. The SAXS curves were obtained by step scanning in a range from 0.06 nm to 0.4 nm.
For the Dynamic light scattering (DLS) analyses a Zetasizer Nano ZS (standard laser beam wavelength= 632.8 nm) was used. Samples were prepared diluiting the NPs solution to a final concentration in a range from 0.1 mg/ml to 1.0 mg/ml and were sonicated for 30 seconds with a Microson™ultrasonic cell disruptor XL.
For the UV-visible analysis, a UV Agilent 8453 spectrophotometer was used. The spectra were recorded in a range from 100 nm to 1000 nm.
For the NPs uptake by the macrophages, a BD FACSCanto™II (Becton Dickinson), with a BD FACSDiva™Software, was used. The analyses were conduct using the PE channel: excitation with Blue laser (488 nm, air-cooled, 20-mW solid state) emission$_{max}$ 575 nm, dichroic mirror 556LP, band pass filter 585/42.
For the viability analysis, a VersaMax Microplate Reader, from Molecular Devices was used.

Silica NPs dissolution test

In order to evaluate the NPs dissolution in water, 2 ml of silica NPs solution (15 mg/ml), were dialyzed in a plastic becker against 500 ml of milliQ water. At different times, a known amount of the solution outside the dialysis tube was collected, stored at −10 °C and the same volume of milliQ water was reintroduced into the dialysis becker. Collected samples were analyzed with molybdate assay test [65]. Molybdate assay test is a colorimetric method which allows to determine the concentration of soluble SiO_2 in water. In order to avoid filtration and dilution, milliQ water was used. The only specific substance known to interfere in the color reaction is phospate, that is eliminated by the addition of oxalic acid. The reliability concentration range of this method is from 5 mg/ml to 0.019 mg/ml when monitoring the absorption at the wavelength 815 nm. The solutions used for the molybdate assay test are shown in table 2.7 and were prepared the day before, in order to allow a complete dissolution of the powders in milliQ water. Then they were stored in plastic bottle, in dark, at 4 °C.

In order to obtain the standards for the calibration curve, the sodium silicate stock solution (200 mg/ml) was diluted (from 5 mg/ml to 0.019 mg/ml) and the absorbance checked

Reagent	Quantity weighed (g)	Final volume (ml)
Amino-naphthol-sulfonic acid	0.5	50
Ammonium molybdate	7.5	100
Oxalic acid dihydrate	10	100
Sodium silicate	0.0473	100
Hydrochloric acid	25 ml	50

Table 2.7: Solutions used for molybdate assay test.

through a spectrophotometer. In a cuvette, 500 µl of silica solution, 10 µl of hydrochloric acid and 20 µl of ammonium molybdate solution were added. After gentle hand swirling, the reaction mix was allowed to stand for 5 minutes and than 15 µl of oxalic acid were added. After 1 minute, 20 µl of amino-naphthol-sulfonic acid were added to the solution. The absorbance was monitored at 815 nm. The same protocol described above was used to check the absorbance of the samples.

Viability test

In order to test the cell viability after the incubation with silica nanoparticles, the XTT cell viability assay was used. XTT cell viability assay provides a simple method for determining live cell numbers. XTT is a tetrazolium derivative and measures cell viability based on the activity of mitochondrial enzymes, that are activated only in live cell. XTT in live cells is reduced to a highly orange-colored and water-soluble product. The amount of this product will be proportional to the number of living cells in the sample and can be photometrically quantified, probing the absorption at 475 nm. XTT cell viability assay works in most cells lines and 0.2-2x10^4 cells/well should be sufficient for most experiments.

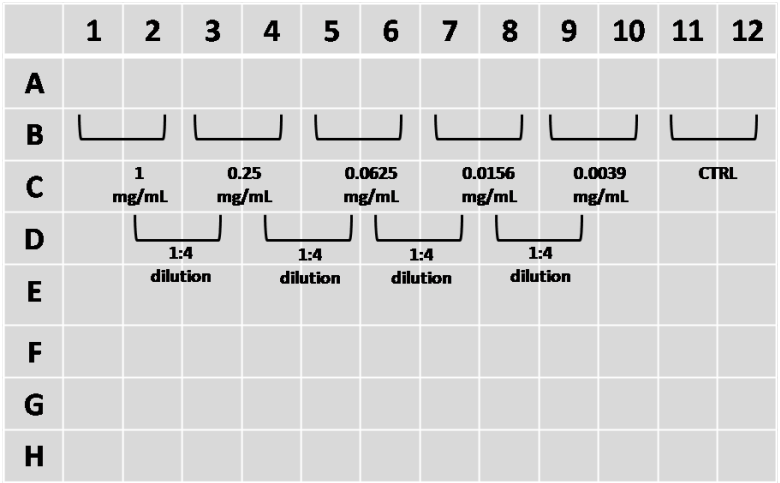

Figure 2.3: Example of a 96-well plate used for the Cell Viability Assay.

Three different cells lines were used in order to test the NPs toxicity: RAW 264.7 murine macrophages, human fibroblasts and human embrional kidney (HEK) 293 wild type (WT) cells. In a 96-well plate, cells were seeded at appropriate concentration in 90 µl of complete medium. The next day 10 µl of NPs, properly diluted, was added in duplicate and the cells were incubated at 37 °C for 48 hours. The dilution used for the experiments are shown in figure 2.3. The viability of the cells was evaluated at 24 hours and 48 hours using a microplate reader, as described above. Using the same protocol described above, the viability cell was evaluated after the incubation of NPs with BSA.

Proteins absorption test

BSA is a globular protein, having a MW of approximately 66.000 Da and it is used in numerous biochemical applications, including enzyme-linked immunosorbent assay (ELISA), immunoblots and immunochemistry. It is also used as nutrient in microbial culture, stabilizer during digestion of DNA and as a standard for quantitative assay, like Bradford protein assay. To evaluate the absorption of this protein to bare and pegylated silica NPs, an SDS electrophoresis gel was prepared, as shown in table 2.8.

Reagent	Stacking gel µl	Running gel µl
SDS	2310	7000
TRIS	5000	9000
Acrylamide	1700	14500
MilliQ Water	1300	38500
APS	80	210
TEMED	7.5	17.5

Table 2.8: Reagents used to make two SDS electrophoresis gel.

A stock solution of BSA diluited in PBS (50 mg/ml), and three standards (5 µg, 2 µg, 1 µg) were also prepared at the same time. The PBS recipe is shown in table 2.9. In order to obtain 170 µg of NPs for each reaction mix, a known amount of the sample was transferred into an eppendorf tube (table 2.10) and incubated with 200 µl of the BSA solution at 37 °C for 1 hour. Samples were than washed with PBS five times, centrifuged (15.000 g for 20 minutes) and the pellet was resuspended into 1 ml of PBS.

An eppendorf tube containing the resuspended pellet (40 µg of NPs) and the sample buffer concentrated 4 times (4X) was prepared, in order to obtain 20 µl of the sample to load in each well of SDS electrophoresis gel. The last washing of each sample be loaded into a well of the SDS electrophoresis gel, in order to check the eventual presence of residual BSA. Three standards of BSA solution and a marker, as a molecular-weight size standard, were also loaded in the wells of SDS electrophoresis gel. The loading order is shown in figure

Reagent	Molar concentration (mM)	M.W. (g/mol)	Quantity weighed (g)
Sodium chloride	150	58.44	8.766
Sodium hydrogen phospate	2.5	177.99	0.445
Sodium dihydrogen phospate	2.5	137.99	0.345

Table 2.9: Recipe of PBS.

Sample	Concentration (mg/ml)	Amount of sample (µl)
S2y	38.55	4.64
S2y800a	24.10	7.43
S2y25a	46.85	3.82
S2y120b	19.75	9.06
S2y4b	17.90	10.00
S2y75a25b	32.55	5.5
S2y25a75b	21.10	8.48

Table 2.10: Amount of sample added to each well during the electrophoresis gel

2.4. Using the same protocol described above, the protein absorption was evaluated after the incubation of NPs with human serum.

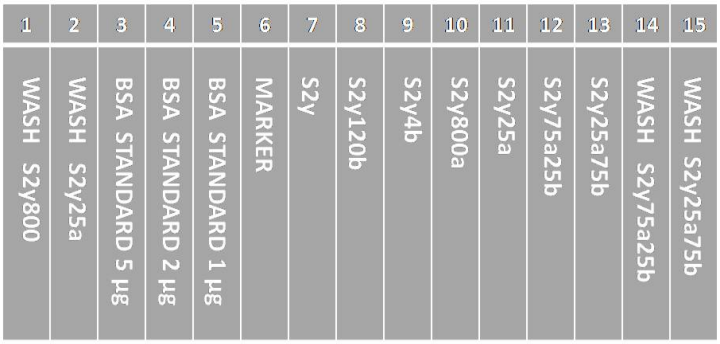

Figure 2.4: Loading order of the SDS electrophoresis gel.

Uptake test

In order to obtain the data related to the NPs uptake, a flow cytometer BD FACSCanto™II, with BD FACSDiva™software were used. In a 24-well plate the macrophages RAW 264.7 were sedeed ($3x10^5$ cells/well) and left to spread overnight. Then the cells were incubated with different concentrations of fluorescent NPs for 24 hours at 37 °C. After the incubation the cells were washed with PBS and detached from the plate. The fluorescence was acquried using the phycoerytrin (PE) channels of a BD FACSCanto™II flow cytometer.

Chapter 3

Results and discussions

3.1 Physical and chemical characterization

3.1.1 mPEG-silane

Infrared spectroscopy analyses

In order to recognize the characteristic vibrations of the PEG chemical groups, the mPEG-silane 5000 and mPEG-silane 550 infrared spectra were acquired. To let all the water evaporate, about 20 mg of the dry samples (500 µl) are placed on a heating block overnight. The mPEG-silane chemical structure is also depicted, in order to make clearer where the IR vibrations originate from.

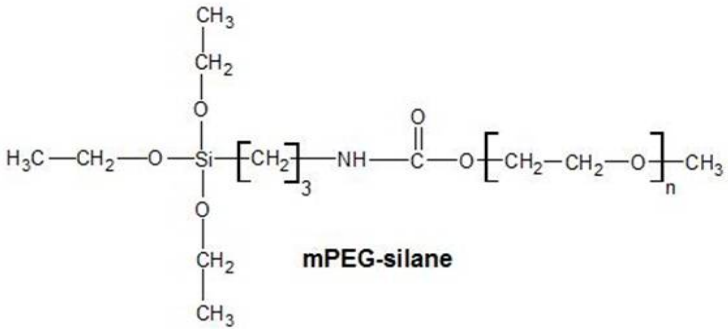

Figure 3.1: Chemical structure of mPEG-silane.

In figure 3.2 the characteristics peaks of mPEG-silane are shown. The peak centered at 1715 cm^{-1} is characteristic of the urethane carbonyle group vibration (C=O) [66], while the peak at 1537 cm^{-1} is attribuited to the amine group in the urethane bond (NH) [67]. The vibrations of the $-CH_2$ groups are centered at 1466 cm^{-1}, 1348 cm^{-1}, and 1279 cm^{-1} [68]. The peak centered at 943 cm^{-1} is characteristic of the –CH group. The peaks centered at 1240 cm^{-1} and 1105 cm^{-1} belong respectively to the C–O and Si–O bond [69, 70]. The peaks in the range between 2934 cm^{-1} and 2865 cm^{-1}, show the absorption of asymmetric

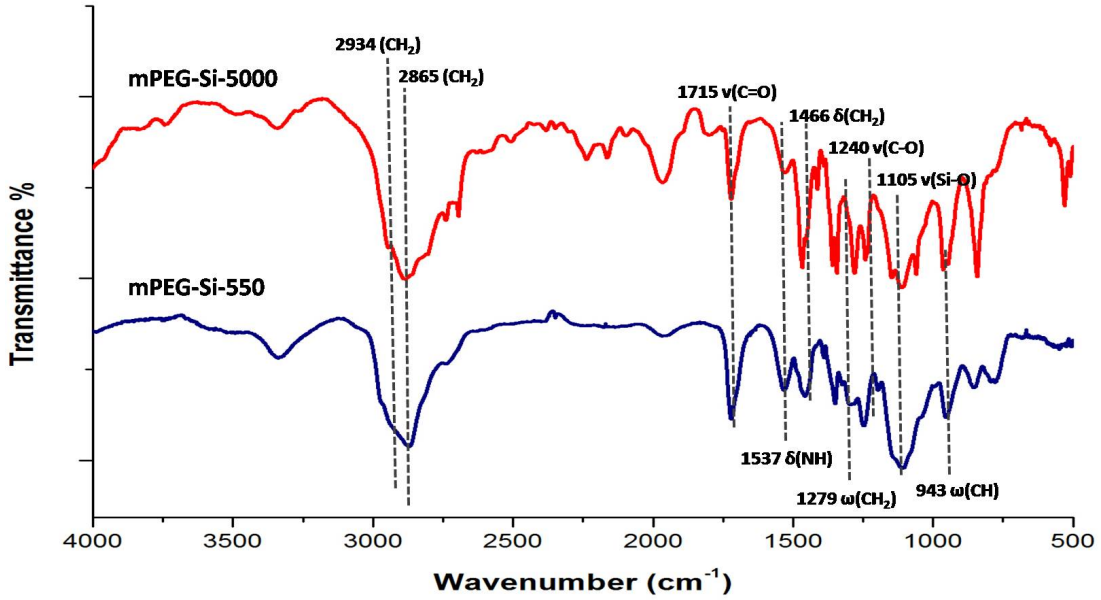

Figure 3.2: IR spectra of mPEG-silane 550 and mPEG-silane 5000.

and symmetric $-CH_2$ adjacent to a carbonyl group [71].

As shown in figure 3.2, the vibrations between 1466 cm^{-1} and 1279 cm^{-1}, related to the $-CH_2$ groups, are more intense for mPEG-silane 5000 than for mPEG-silane 550. The reason should be searched in the chain length of the PEG. Actually, mPEG-silane 5000 is composed of more $-CH_2$ units than the mPEG -silane 550, leading to an enhanced signal intensity.

Definitely, the correct synthesis of the mPEG-silane 5000 and mPEG-silane 550 were confirmed by the IR analyses. In the light of above, both of the polymer were chosen for the pegylation step of the silica NPs synthesized.

3.1.2 Thermogravimetric analyses

Differently from the mPEG-silane 550, which is liquid, the mPEG-silane 5000 can be analyzed by means of thermogravimetric analysis. In figure 3.3 the results are shown. The weight loss due to the polyethylene chain can be recognized in the TG curves, according to the literature [72].

As shown in figure 3.3, the TG curve of the mPEG weight loss does not reach the zero, because of the remaining fraction of SiO_2 after the polyehtylene chain weight loss, of about 1.3 weight percentage. According to the stoichiometry of the compound, from each

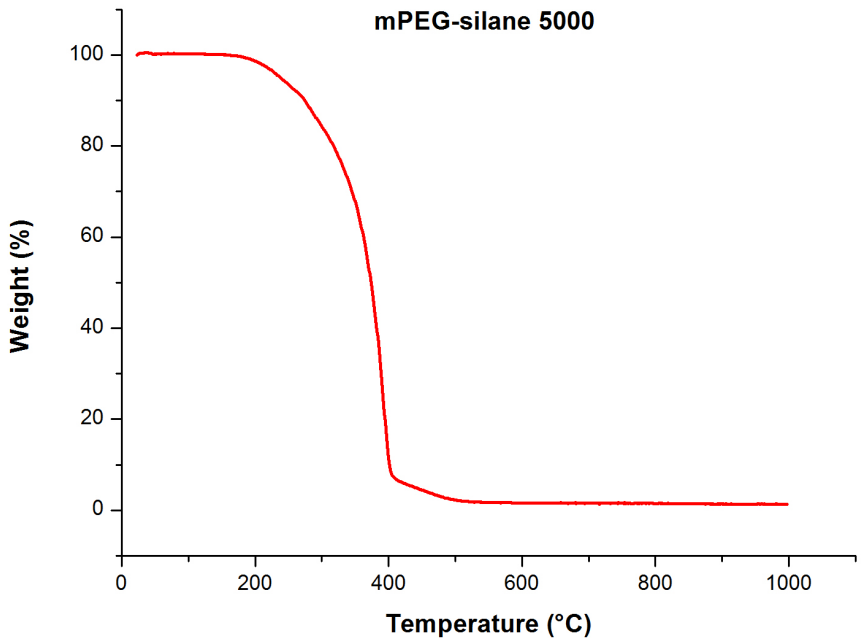

Figure 3.3: TG curves of mPEG-silane 5000.

mPEG-silane mole a mole of SiO_2 is generated after the thermal treatment. From these calculations, one should observe a 1,14 % of remaining weight in the sample, in fairly good agreement with the experimental value obtained.

3.1.3 Silica nanoparticles

Infrared spectroscopy anlyses

In order to verify the PEG grafting onto the pegylated silica NPs, an infrared spectrum of each sample was acquired. Before the analysis, about 20 mg of the dry samples (500 µl) are placed on a heating block overnight, in order to let all the water evaporate. In figure 3.4 the spectra acquired are shown, from the less pegylated to the more pegylated one.

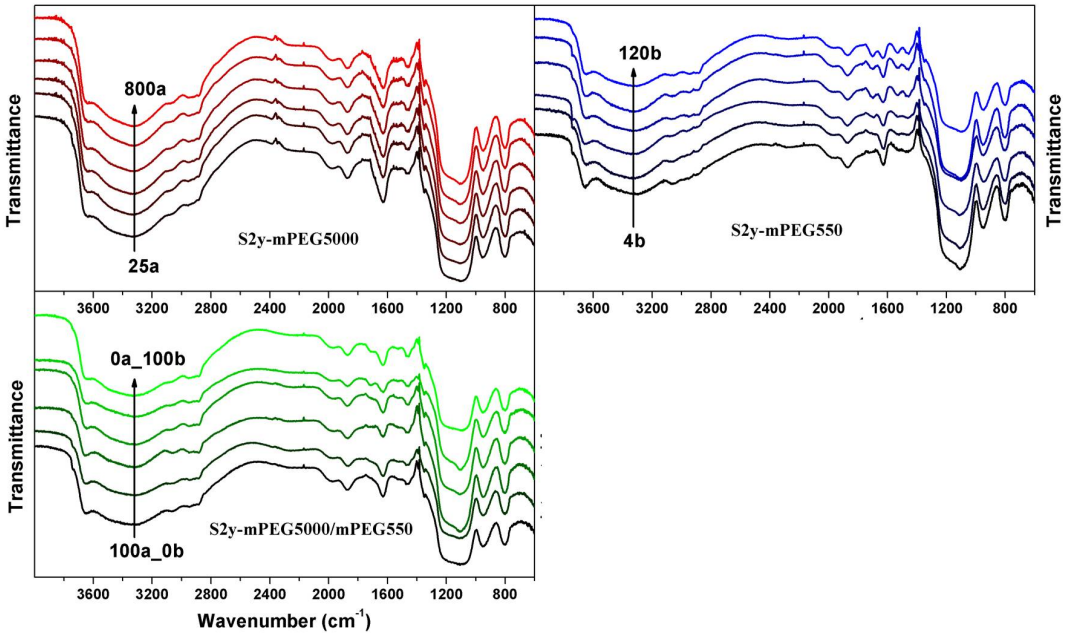

Figure 3.4: IR spectra pegylated NPs. Spectra of pegylated NPs with mPEG-silane 5000 (red). Spectra of pegylated NPs with mPEG-silane 550 (blue). Spectra of pegylated NPs with mPEG-silane 5000 and 550 (green).

In order to make clearer the PEG grafting onto pegylated silica samples, a comparison between the pegylated and bare samples (S2Y, S2Y800a, S2Y120b, S2Y50a50b) was done.

As shown in figure 3.5, all the pegylated samples display the characteristic peaks of the mPEG-silane. Specifically, the peaks centered at 1348 cm^{-1}, 1452 cm^{-1}, and 1285 cm^{-1} belonging to the vibrations of the CH_2 group, while peak centered at 943 cm^{-1} is attribuited to the out of plane bending vibration of –CH group. Moreover, the vibrations of the C=O bond, –NH group, and C–O bond, can be well appreciated in figure 3.5, centered at 1715 cm^{-1}, 1537 cm^{-1} and 1246 cm^{-1} respectively. Both pegylated and bare samples, show the characteristics peaks of the Si–O–Si bond, centered at 806 cm^{-1} and 1087 cm^{-1}. All the characteristic vibrations are summarized in the correlation table 3.1.

In order to verify the different PEG amount grafted onto the NPs, the IR spectra were

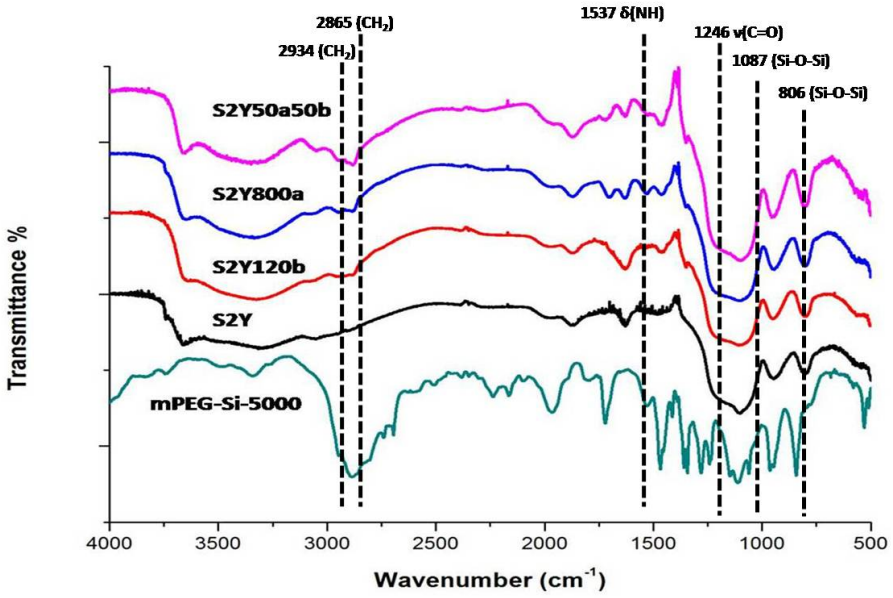

Figure 3.5: IR spectra of bare, pegylated NPs and mPEG-silane 5000.

Number	Wavenumber cm^{-1}	Vibration
1	806, 1087	Si–O–Si
2	1105	Si–O stretching
3	1246	C–O stretching
4	1348	$-CH_2$ twisting
5	1466	$-CH_2$ scissoring
6	1537	–NH scissoring
7	1715	C=O stretching
8	2934, 2865	$-CH_2$ stretching

Table 3.1: Correlation table related to the vibrations of mPEG-silane.

processed using Origin. Specifically, for all the samples of the same batch, the area under the curve of the vibration of the –CH alifatic groups under 3000 cm^{-1}, was evaluated and plotted against the PEG/Si molar ratio.
In figure 3.6 it is shown the increase of the area under the curve according to the increase of the PEG/Si molar ratio. This phenomenon is preserved for both of the pegylated batches, with mPEG-silane 5000 and mPEG-silane 550.

To sum up, the pegylation step has been succesful for all the samples synthesized. Three pegylated batches of NPs were succesfully synthesized: with mPEG-silane 5000, mPEG-silane 550, and a mixture of two PEGs. Differently from the bare samples, the pegylated samples show the characteristic vibrations of the PEG groups, allowing to confirm the polymer grafting. Moreover, also the pegylation using different amount of the same MW mPEG-silane has been succesful, proved by the increase of the area under the curve.

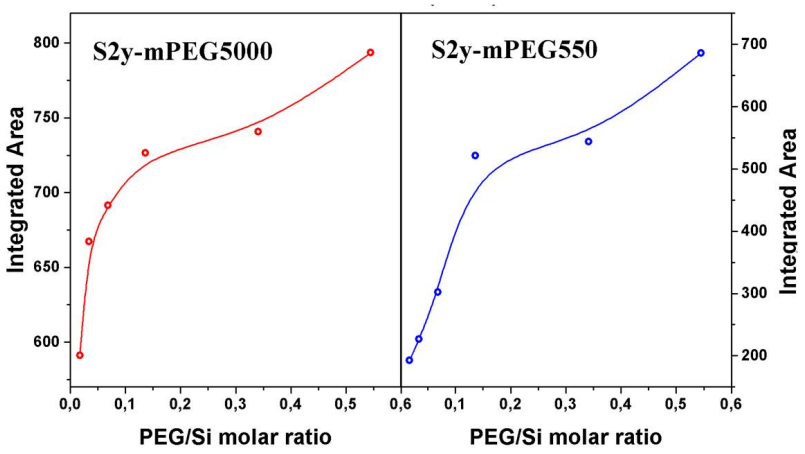

Figure 3.6: Evaluation of the PEG amount of pegylated samples. The integrated area of the IR spectra is plotted versus the PEG/Si ratio.

Thermogravimetric analyses

Four of the pegylated silica NPs, respectively the less and the most pegylated of the singly doped series (S2y25a, S2y500a, S2y4b, S2y120b), and the bare silica sample (S2y) were analyzed by means of thermogravimetric analysis. The day before the analysis, all the samples were put on a heating block at 80 °C overnight, in order to let the water evaporate. Than the TG and the DSC curves were acquired in air and nitrogen (air flow rate 40 ml/min, nitrogen flow rate 80 ml/min), in a range between 40 °C and 1000 °C, with a scan rate of 20 °C/min.

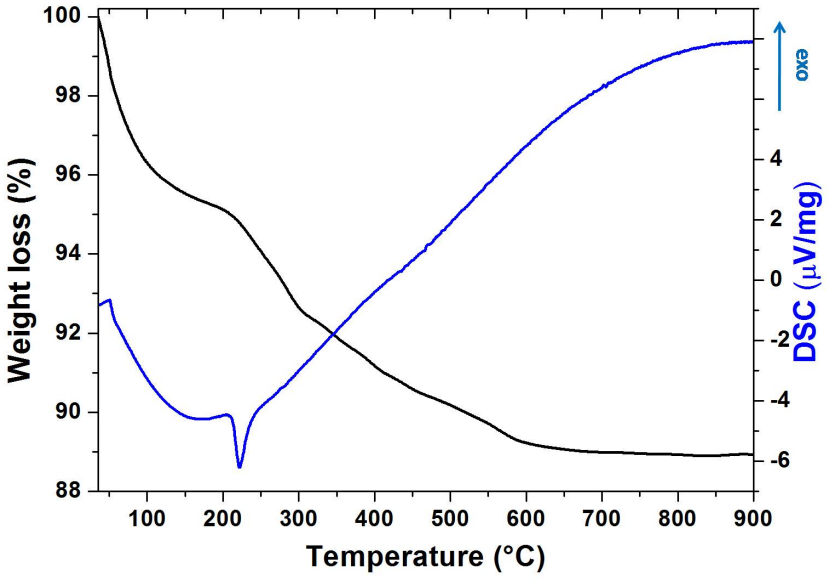

Figure 3.7: TG curves of a pegylated samples (S2Y120b).

Because of the remaining solvents in the samples pegylated with mPEG-silane 550 (figure 3.7), the first weight loss occurs up to 100 °C. Moreover, an additional weight loss is observed in figure 3.7, between 100 °C and 500 °C, due to the decomposition of the organic groups and the dehydroxylation of the silanol groups. The DSC curve shows an endothermic peak around 220 °C, which is the boiling point of the mPEG-silane, according to the commercial data [73].
In order to evaluate the different weight losses related to the amount of PEG used in the pegylation steps, the TG curves were processed. After the data processing, the total weight loss in the range between 250 °C and 1000 °C was evaluated for all the samples. The results are shown in figure 3.8 and summarized in table 3.2. The % of PEG grafted shown in table 3.2 is related to the total amount of PEG added to the reaction mixture during the pegylation step.

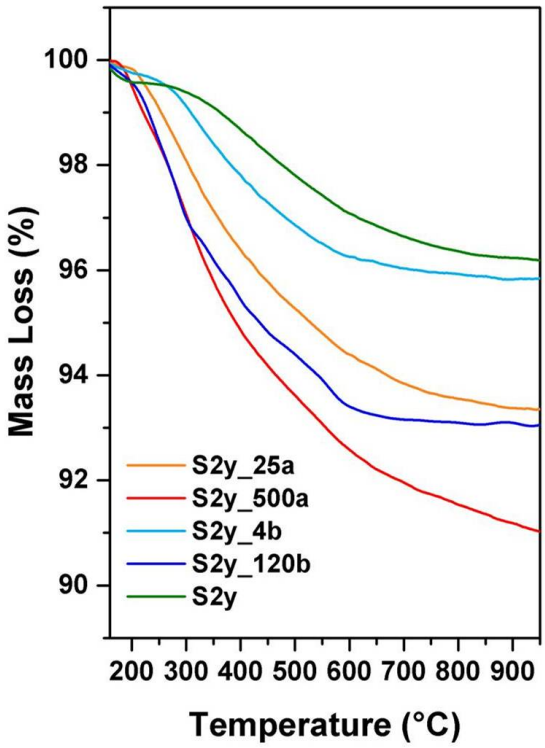

Figure 3.8: Weight losses of bare and pegylated NPs.

As shown in figure 3.8 the weight loss is proportional to the amount of PEG used. Specifically, samples pegylated with a higher amount of PEG show a higher weight loss, according to the objective of this study.

Analyzing the data about the PEG percentage grafted onto the silica NPs some considerations should be done. Increasing the PEG amount added to the reaction mixture, during the pegylation step, the percentage of PEG grafted to the silica NPs also increases, up to a limit value, in which the saturation point is reached. This situation is shown for both the MWs PEG. Moreover, comparing the two MWs PEG, the saturation point is

Sample	PEG/SiO_2 mg/500mg	PEG added %	PEG grafted %
S2Y25a	25	50	6
S2Y500a	500	5	3.5
S2Y120b	120	19	3.7
S2Y4b	4	0.8	0.66

Table 3.2: Processed data related to the weight loss of the pegylated samples.

reached before for the mPEG-silane 5000, because of the higher molecular weight and steric hindrance, which allow a less grafting to the NPs.

Scanning electron microscope analyses

In order to evaluate the size, the shape and the distribution of the pegylated and the bare NPs, SEM images were acquired. In figure 1.7 one image for each batches synthesized is shown.

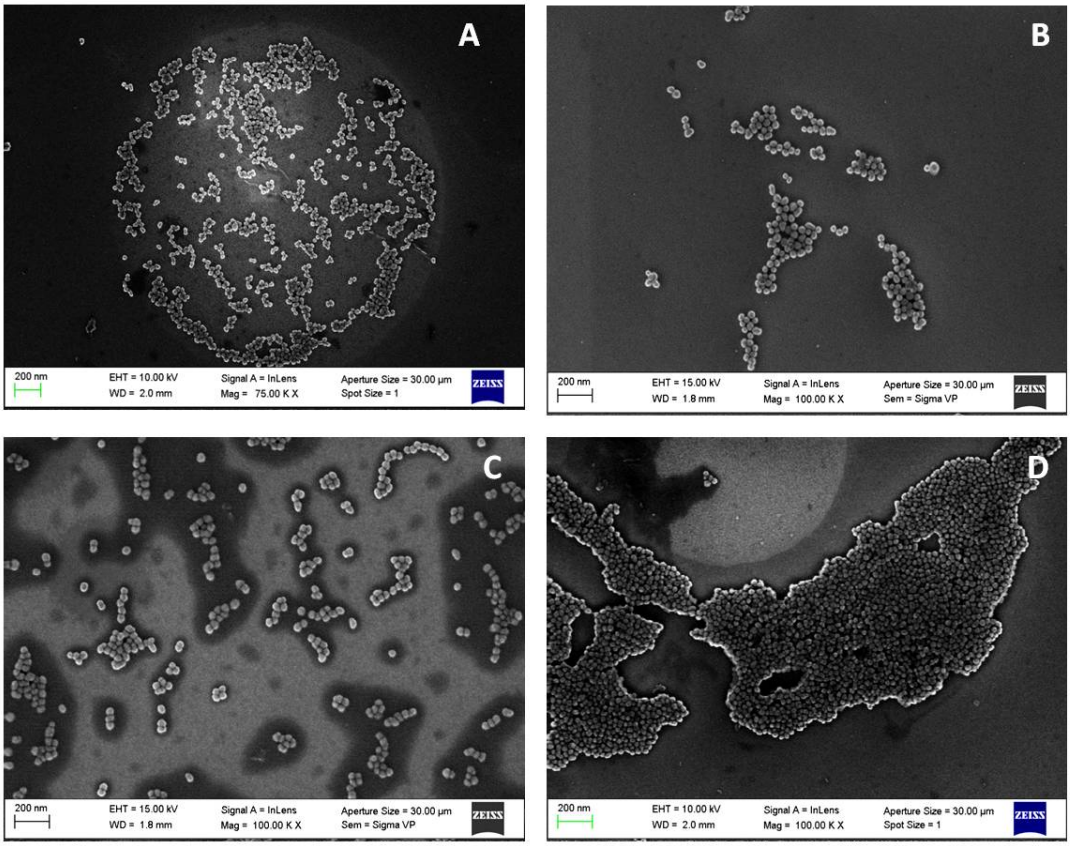

Figure 3.9: Images acquired by the SEM of the bare and pegylated silica NPs. A) Pegylated silica NPs with mPEG-silane 5000 (S2Y800a). B) Pegylated silica NPs with mPEG-silane 550 (S2Y120b). C) Pegylated silica NPs with a mixture of mPEG-silane 5000 and 550 (S2Y50a50b). D) Bare silica NPs (S2Y).

To allow a better analysis of the data, a SEM image was acquired for each sample of the four batches synthesized, as described in the previous sections. The images acquired were then processed using ImageJ software. The results for all the samples synthesized are shown in table 3.3.

Sample series **a**	Radius *nm*	Sample series **b**	Radius *nm*	Sample series **ab**	Radius *nm*
S2y800a	24 ± 1	S2y120b	20 ± 1	S2y100a0b	23 ± 1
S2y500a	18.0 ± 0.2	S2y75b	20 ± 2	S2y75a25b	18.6 ± 0.2
S2y200a	18.4 ± 0.1	S2y30b	18 ± 4	S2y50a50b	18.9 ± 0.1
S2y100a	23.2 ± 0.1	S2y15b	19.8 ± 0.8	S2y25a75b	22.2 ± 0.1
S2y50a	18.0 ± 0.1	S2y8b	17.3 ± 1.5	S2y10a90b	19.1± 0.1
S2y25a	20.4 ± 0.1	S2y4b	15.8 ± 0.2	S2y0a100b	21.4 ± 0.1
		S2y	18.0 ± 0.1		

Table 3.3: Radii of the NPs pegylated with mPEG-silane 5000, mPEG-silane 550, and a mixture of them, plus the bare silica NPs.

These NPs are well dispersed and have an average radius of about 20 nm. Due to the thin layer of PEG on the NPs surface, there are no evident differences in radius between the pegylated and the bare silica NPs.

The shape of the NPs can be well appreciated in figure 3.10 to be spherical, especially when the NPs are well dispersed. Actually a slight aggregation phenomenon is shown, maybe due to the poor sonication time.

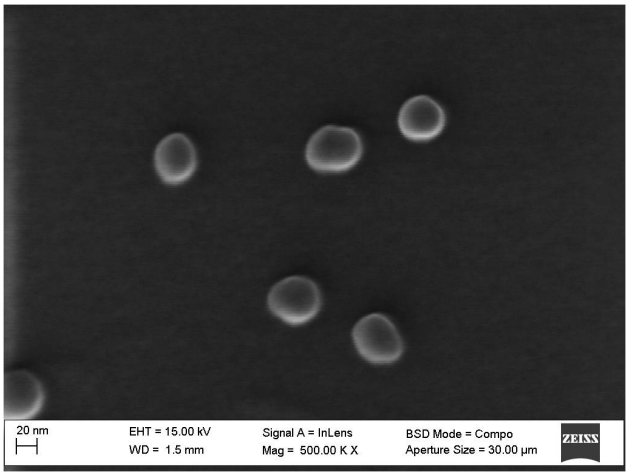

Figure 3.10: SEM images of pegylated silica NPs (S2Y800a).

These samples were used for the following studies because of their size below 100 nm, perfectly in accordance with the definitions of NPs. This type of NPs having small radius, good polydispersion, and stability in solution are optimally suited for biological applications, as described in the previous sections.

Small angle X-ray scattering analyses

The SAXS patterns of the samples confirm the SEM data obtained about the size and the shape of the NPs. We choose to display a single SAXS spectra as representative of the data of all the samples, which were dispersed in mPEG-silane 550 for the analyses. The NPs radius is centered around 20 nm.

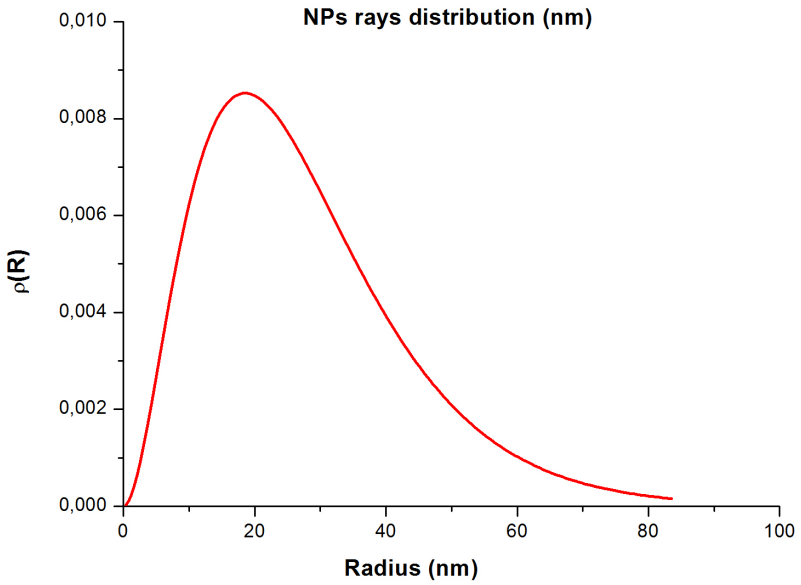

Figure 3.11: Volumetric distribution of silica NPs radii.

The SAXS curves were fitted considering a two phase system, where homogeneous spherical NPs are dispersed in a continuous medium. In order to calculate the SAXS of the distribution of spherical NPs, some considerations should be done. The NPs and the medium have respectively, scattering legth of ρ_p and ρ_m, which for X-ray scattering is the average electron density of the two phases. For a diluite system, in which the interparticle interferences can be neglected, only the sum of the scattering produced by the single NPs, is considered.

$$I(h) \propto (\rho_p - \rho_m)^2 \int_0^\infty N(r) r^6 I^0(h,r), dr \tag{3.1}$$

where $h{=}4\pi sin(\theta)/\lambda$,
$I^0(h,r)$ is the normalised form factor of the single particle of size r;
r is the size of the particle;
$N(r)$ is the size distribution density.

For a homgeneous spherical NP the form factor is:

$$I_0(h,r) = \left[3\frac{sin(hr) - hrcos(hr)}{(hr)^3}\right]^2 \tag{3.2}$$

Very often the $N(r)$ obtained by the inversion of the equation 3.1 presents large deviation in the small r region and this behaviour is evident when studying simulated data obtained by some previously chosen distribution. This is because the integrand in 3.1 depends on the sixth power of r (so it is more sensitive to the large particles) and because the experimental data are known only in a restricted region of the reciprocal space $h_{min}<h<h_{max}$ so we have a restricted resolution in the $N(r)$ function. This limits the meaningful support of the analysable distribution $N(r)$ that has to completely developed in the in the $r_{min}=h/2h_{max} <r<r_{max}=h/2h_{min}$ in order to obtain reliable results from the analysis of the scattering intensity [74].

However, the approach used in this thesis consider the shape of the size distribution as an a priori chosen function which depends of some refinable parameters: the most used are the log-normal, the Gaussian, the Shultz, and the Weibull distributions. In this thesis we analyse the data by using the non linear least squared method, and assuming the Shultz distribution as an a priori particle size distribution. The Shultz function (3.3), which allows the numerical integration of the function 3.1, depends of two refinable parameters: $< r >$ which is the mean value, and z which is the parameter that controls the shape and the width of the distribution.

In particular the distribution reduces to $\delta(r- < r >)$, with $z \leftarrow \infty$:

$$N(r) = \frac{1}{\Gamma(z+1)}\frac{z+1}{< r >}^{(z+1)} r^z e^{-\frac{z+1}{z}r} \tag{3.3}$$

where z >-1 and Γ is the gamma function.

$$I(h) = (\rho_p - \rho_m)^2 \frac{4\pi}{h^3}[I_1 + I_2 - 2I_3] \tag{3.4}$$

where:

$$I_1 = \frac{b^{z+1}(z+2)(z+1)}{2}\left[\frac{1}{b^{z+3}} + \frac{cos[(z+3)arctg(\frac{2}{b})]}{(4+b^2)^{\frac{(z+3)}{2}}}\right] \tag{3.5}$$

$$I_2 = \frac{b^{z+1}}{2}\left[\frac{1}{b^{z+1}} + \frac{cos[(z+1)arctg(\frac{2}{b})]}{(4+b^2)^{\frac{(z+1)}{2}}}\right] \tag{3.6}$$

$$I_2 = \frac{b^{z+1}(z+1)}{2}\left[\frac{sin[(z+2)arctg(\frac{2}{b})]}{(4+b^2)^{\frac{(z+2)}{2}}}\right] \tag{3.7}$$

with:

$$b = \frac{z+1}{h < r >} \tag{3.8}$$

$$\int_0^\infty N(r)r^n dr =< r > \frac{(z+1)(z+2)...(z+n)}{(z+1()^n)} \tag{3.9}$$

So the Guinier radius becomes:

$$(R_G)^2 = \frac{3 < r^8 >}{3 < r^6 >} = \frac{3(z+7)(z+8)}{5(z+1)^2} < r^2 > \tag{3.10}$$

Using the numerical approach, the data were processed as follows. In figure 3.12 the data fit are shown.

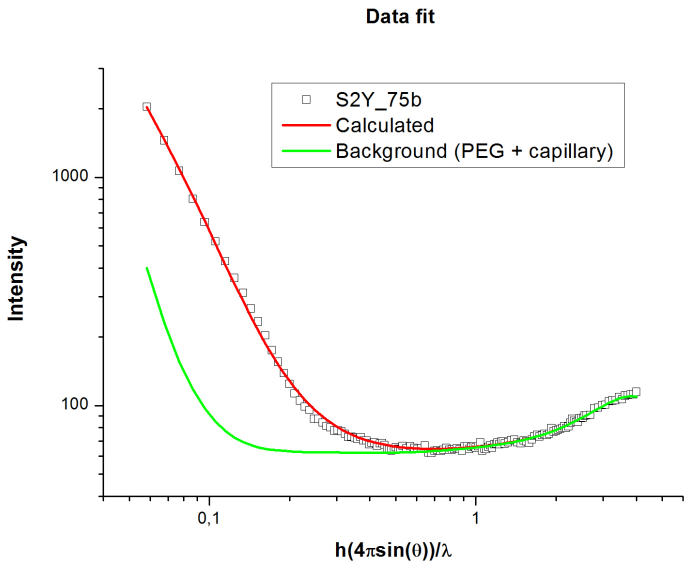

Figure 3.12: Small angle X-ray scattering for a distribution of spherical silica NPs.

Dynamic light scattering analyses

In order to evaluate the hydrodynamic radius of bare and pegyalted NPs, and their stability in solution, DLS and ζ potential curves were acquired. Specifically, the NPs size was measured evaluating the random changes in the scattering of the light from a solution. On the other hand, the ζ potential measures the magnitude of the electrostatic charges on the surface of the NPs in solution, leading to an evaluation of the aggregation phenomena. A characteristic DLS analysis, is shown as follows.

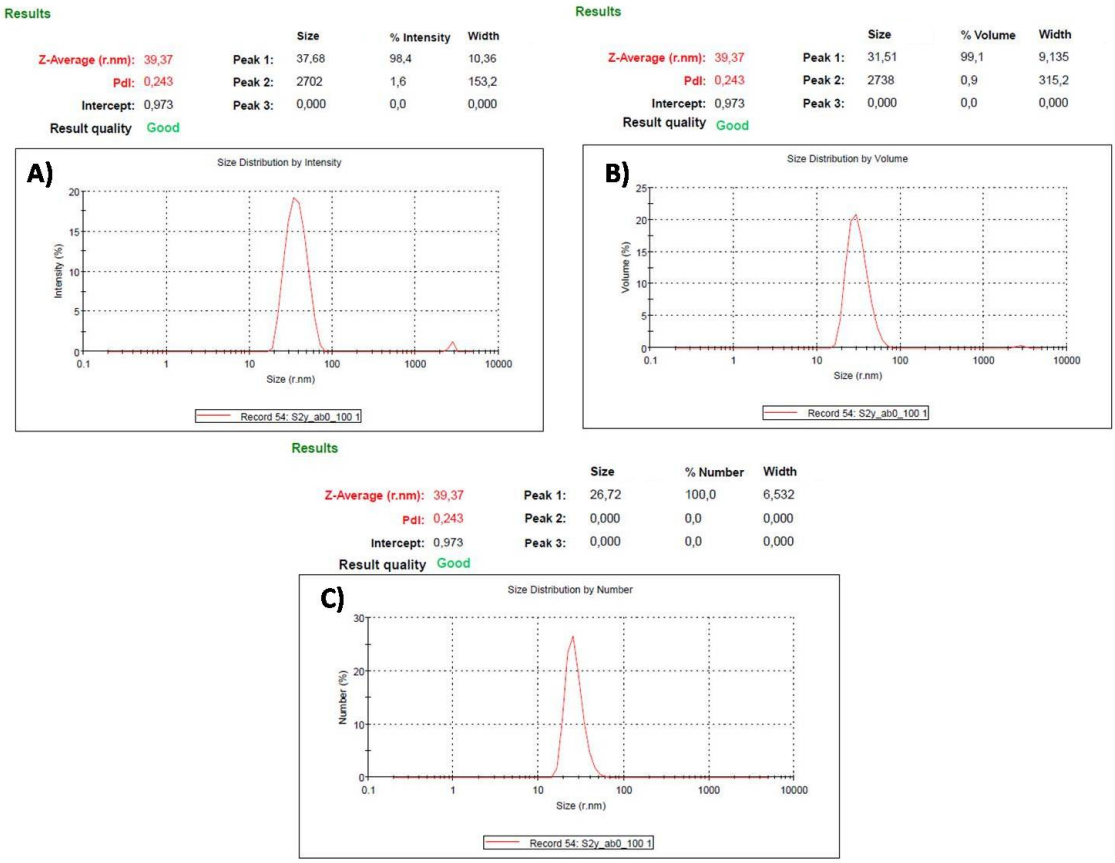

Figure 3.13: Data of a DLS analysis: intensity (A), volume (B), and number (C) weighted distributions.

As shown in figure 3.13, the instrument acquires three curves for each sample: intensity, volume, and number. The first one is a distribution weighted on the scattering intensity, while the second one show the distribution weighted for the volume of the NPs that have a specific size. Eventually the number weighted distribution is representative of the number of NPs which have the same hydrodynamic radius. Using an appropriate sonication time, a well dispersed NPs solution, with a small amount of aggregates can be obtained. The distribution based on the intensity is the only measure directly derived from the correlation function, while the other two, number and volume distribution, are derived from the z-average value. In the light of this, the best parameter to be chosen is the distribution based on the intensity. Moreover, another important parameter to check during a DLS analysis

is the polydispersion index (PDI), which is related to the distribution of the molecular mass in a sample, and it is calculated as follows:

$$PDI = M_w/M_n \tag{3.11}$$

where M_w is the weight average molecular weight;
and M_n is the number average molecular weight.

The size (intensity, volume, and number) and the ζ potential of all the samples were acquired three times, and then processed using Excel, in order to have an average of the samples data. In figures 3.14 and 3.15 the DLS data of a representative pegylated sample and bare silica NPs are shown.

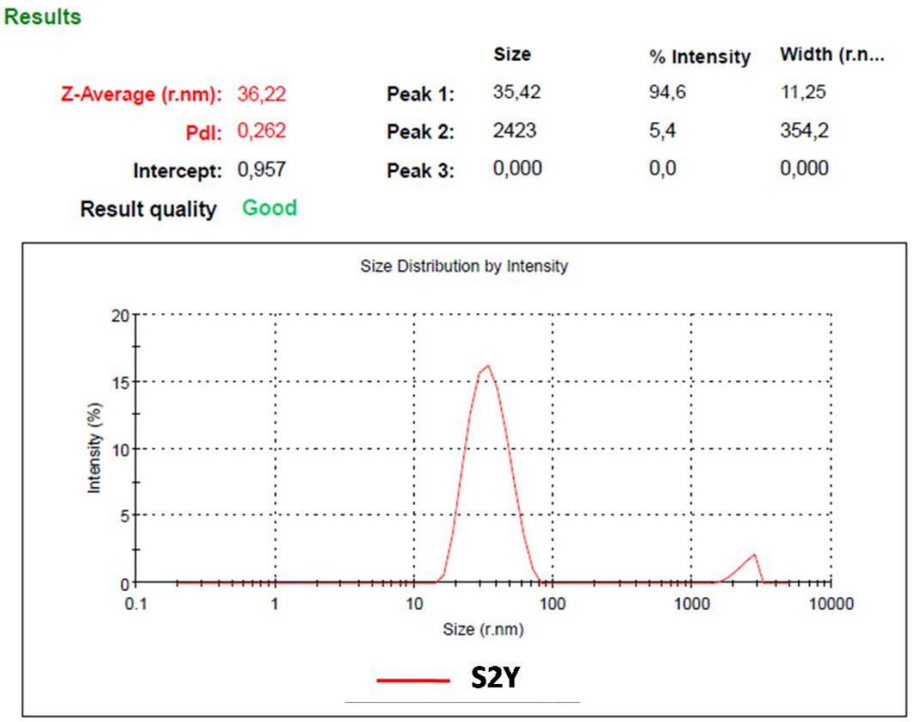

Figure 3.14: DLS data of bare silica NPs (S2Y).

As shown in the previous figures, all the samples, bare and pegylated NPs, show comparable hydrodynamic diameter, in the range between 30 nm and 40 nm. Moreover, a second peak with higher diameter is shown, which indicates a slight aggregation phenomenon of the NPs, maybe due the poor sonication time. However, the PDI have acceptable value and the result quality are good, proving an optimal NPs dispersion for the DLS analyses. The data of all the samples synthesized were acquired and then processed with Excel, in order to obtain a diameter distribution of the NPs, which are shown in table 3.4.

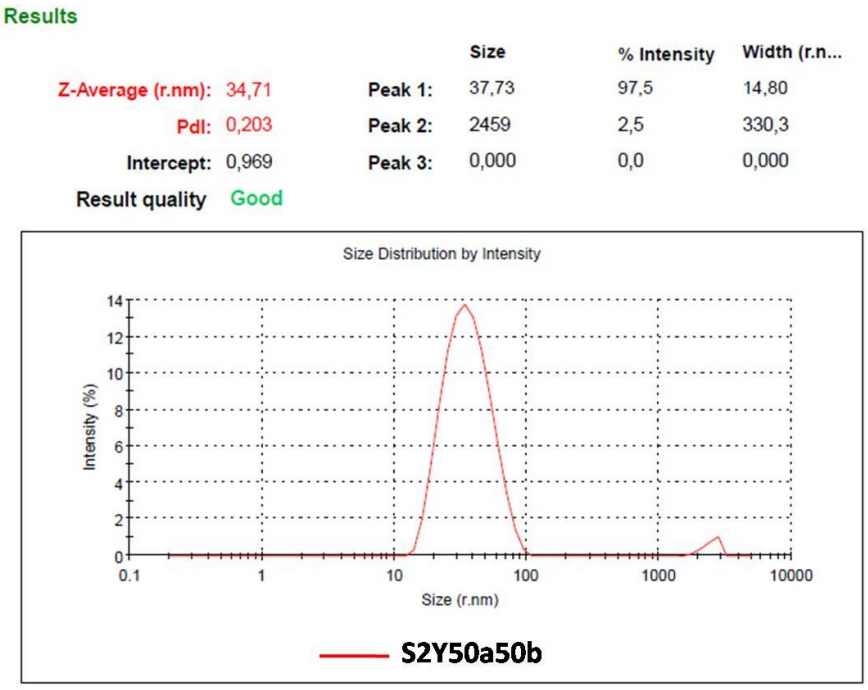

Figure 3.15: DLS data of pegylated silica NPs with mPEG-silane 5000 (S2Y500a).

Sample series **a**	Diameter (nm)	Sample series **b**	Diameter (nm)	Sample series **ab**	Diameter (nm)
S2y800a	35 ± 4	S2y120b	40 ± 4	S2y100a0b	30 ± 1
S2y500a	33 ± 2	S2y75b	39 ± 1	S2y75a25b	33.9 ± 0.4
S2y200a	33 ± 1	S2y30b	41 ± 4	S2y50a50b	34 ± 2
S2y100a	36 ± 1	S2y15b	39.6 ± 0.4	S2y25a75b	38 ± 2
S2y50a	40 ± 1	S2y8b	33 ± 4	S2y10a90b	45 ± 2
S2y25a	40 ± 2	S2y4b	39 ± 1	S2y0a100b	40 ± 3
		S2y	37.1 ± 0.2		

Table 3.4: Diameter distribution of pegylated and bare silica NPs, related to the DLS data.

As shown in table 3.4, the hydrodynamic radii of all the samples are mutually comparable. However there are no evident differences between bare and pegylated NPs. The reason should be searched in the thickness of the PEG layer around the NPs, too thin to be seen by this type of instrument. However, the size previously determined by SEM and SAXS analyses, are confirmed also by the DLS analysis. Moreover, in order to evaluate the NPs stability in solution, also the ζ potential was analyzed for all the samples synthesized, as shown in figures 3.16 and 3.17. In order to obtain a distribution of ζ potential, the data were then processed using Excel, as in the previous set of experiments.

The ζ potential of the pegylated silica NPs is more negative than the ζ potential of the bare NPs. This behaviour has already been reported in the literature, but no definitive interpretation have been proposed to explain it [32]. Specifically, the ζ potential values of

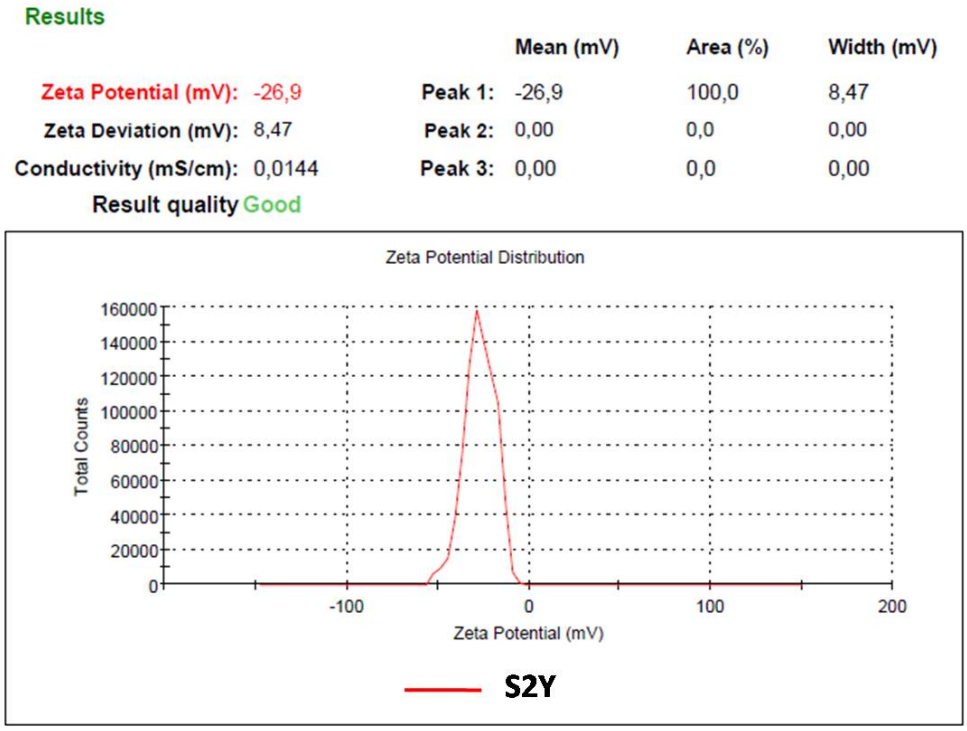

Figure 3.16: ζ potential data of bare silica NPs (S2Y).

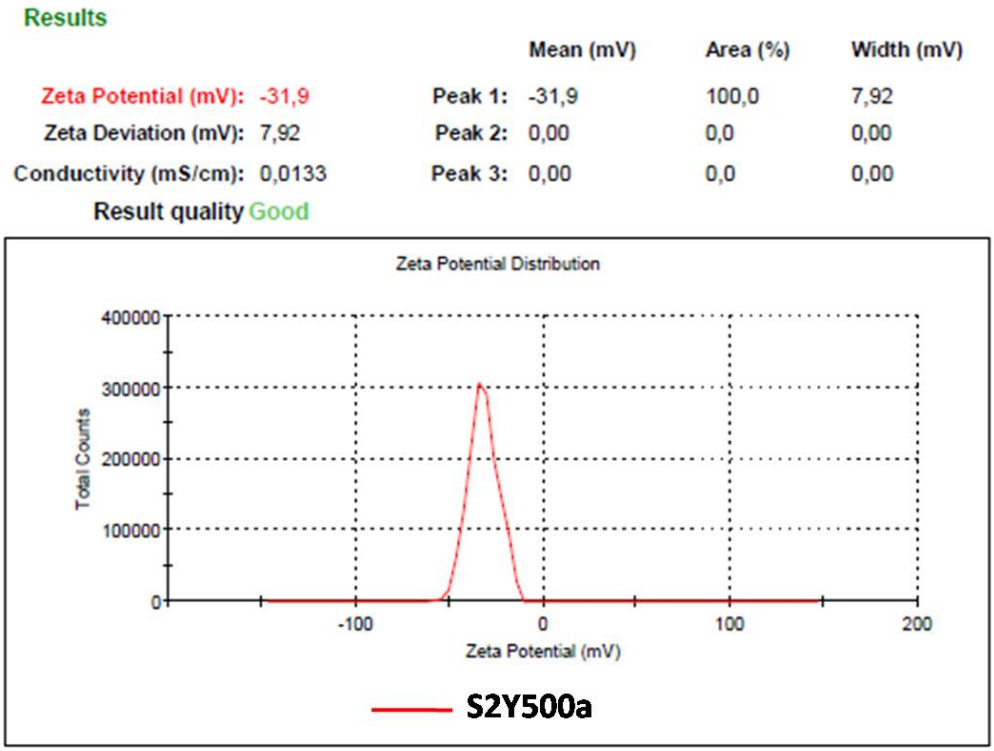

Figure 3.17: ζ potential data of pegylated silica NPs with mPEG-silane 5000 (S2Y500a).

all the samples are shown in table 3.5.

Sample series **a**	ζ potential (mV)	Sample series **b**	ζ potential (mV)	Sample series **ab**	ζ potential (mV)
S2y800a	−26.90	S2y120b	−22.90	S2y100a0b	−31.80
S2y500a	−31.90	S2y75b	−24.00	S2y75a25b	−32.90
S2y200a	−34.10	S2y30b	−24.40	S2y50a50b	−34.90
S2y100a	−34.90	S2y15b	−27.40	S2y25a75b	−33.00
S2y50a	−36.50	S2y8b	−28.00	S2y10a90b	−32.00
S2y25a	−39.50	S2y4b	−28.40	S2y0a100b	−40.50
		S2y	−24.10		

Table 3.5: ζ potential data of pegylated and bare silica NPs.

The ζ potential of the singly doped series are quite comparable. Moreover, samples pegylated with the mPEG-silane 550 show less negative ζ potential rather than the other pegylated samples, comparable with the ζ potential of the bare samples.
However, samples pegylated with different amount of the same MW PEG do not show variations in ζ potential values. The reason should be searched in the thickness of the PEG layer, too thin to affect the ζ potential value.

The NPs were also stable in water and PBS ([NaCl]=100 mM). In the light of above, bare and silica NPs can be used also in PBS, which is largely used in biological analyses because of its ability to mimick the pH and the salt concentration of the biological fluid.

Molybdate assay

In order to evaluate the pegylation effect on the NPs dissolution, the molybdate assay was used. Two samples, bare (S2Y) and pegylated (S2Y500a) NPs were analyzed as described in the experimental section, the data were processed using Origin and are shown as follows.

As shown in figures 3.18 and 3.19 the dissolution process of silica NPs occurs also in neutral solvent, such as the water. However the dissolution rate in deionized water should be far slower than in solution having an acidic or basic behaviour, or containing aggressive ions (e.g. phosphates), as shown in literature [75]. Moreover, the dissolution rate of pegylated silica NPs occurs faster rather than the dissolution of the bare sample. The reason should be searched in the PEG layer around the pegylated NPs, which bring away a first superficial layer of silica when detached from the NPs surface, leading to an enhanced silicate concentration in the solution detected by the molybdate assay.

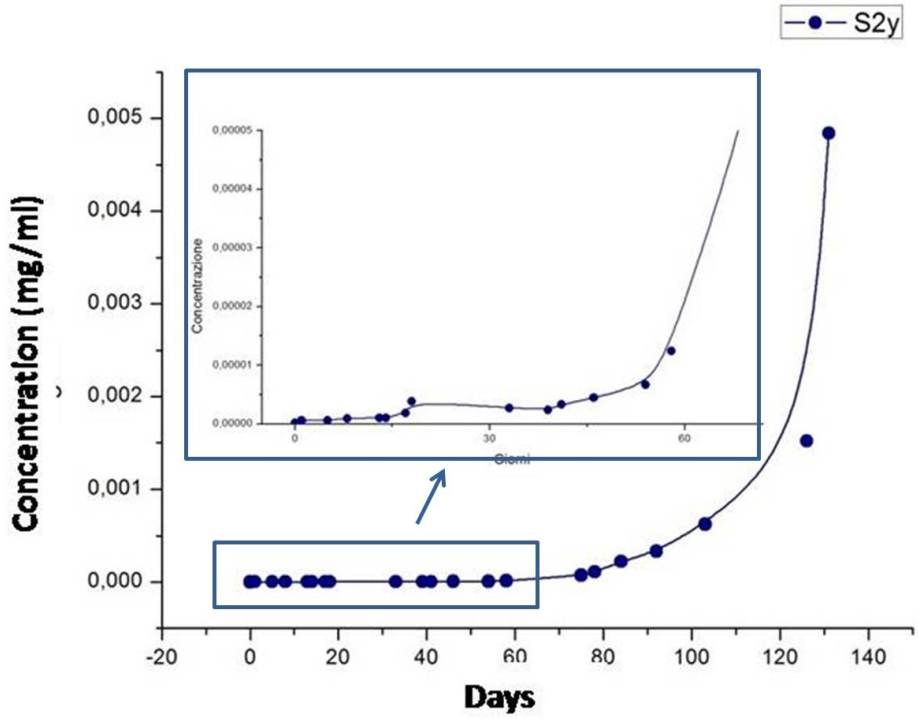

Figure 3.18: Dissolution data of bare silica NPs (S2Y), after 131 days.

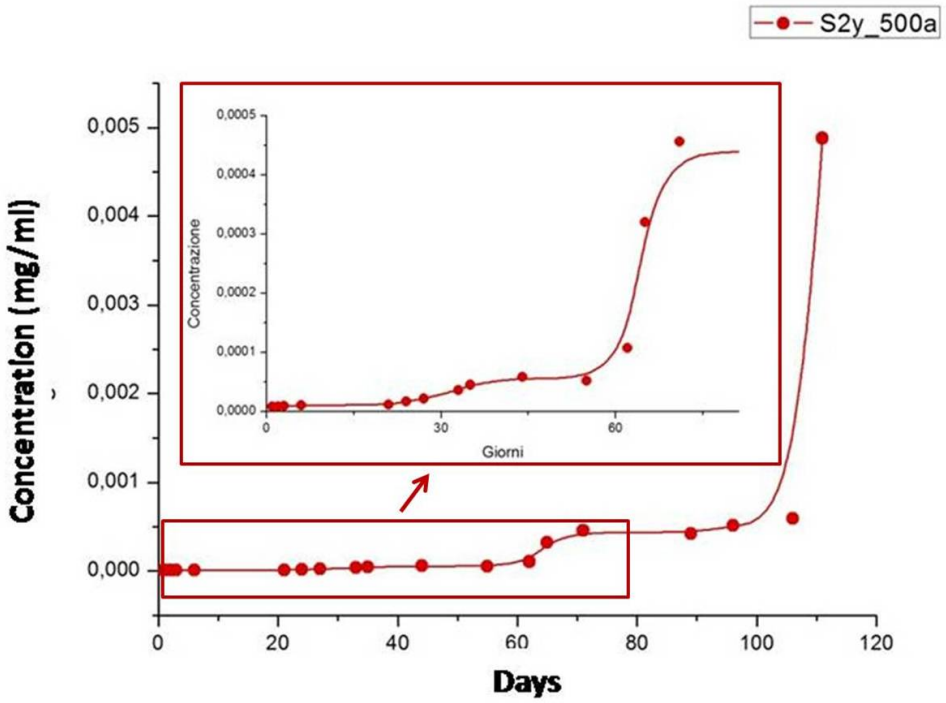

Figure 3.19: Dissolution data of pegylated silica NPs (S2Y500a), after 111 days.

3.1.4 Fluorescent silica nanoparticles

The fluorescent samples incorporating Rhodamine 590, Coumarin 6, and $Ru(bby)_3Cl_2*6H_2O$, synthesized as described in the experimental section, were also characterized using the physo-chemical techniques: such as the SEM and the UV-Visible spectrophotometry.
The emission and the excitation wavelength of the dyes, dissolved in ethanol, were evaluated. In figures 3.20, 3.21, and 3.22 the data are shown, and are summarized in table 3.6.

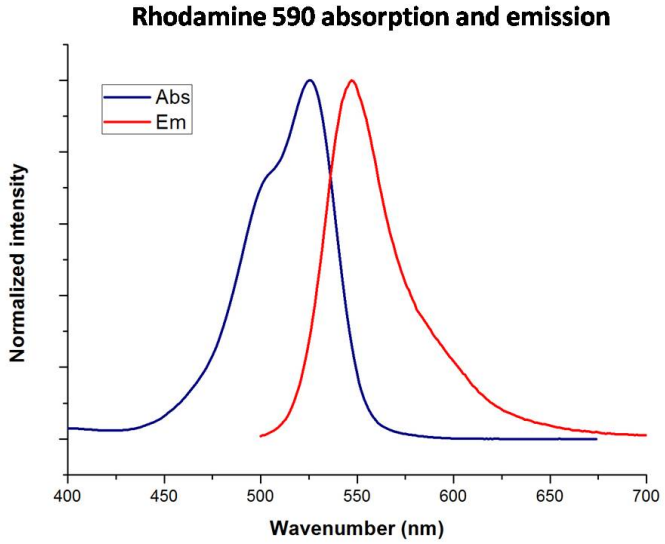

Figure 3.20: Rhodamine 590 emission and absorption spectra.

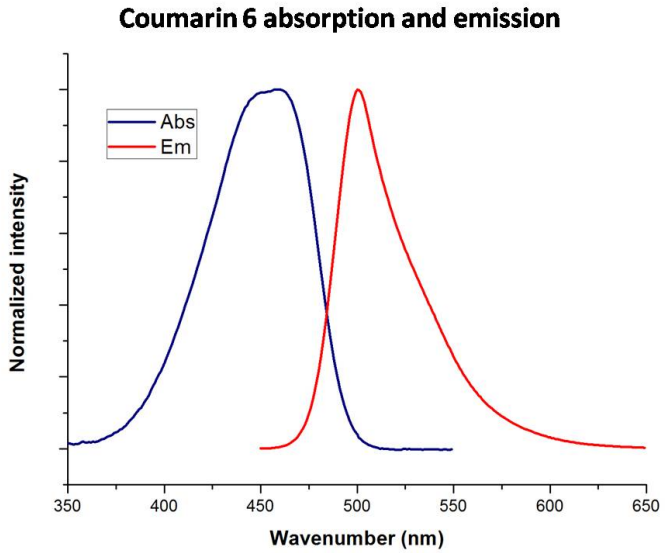

Figure 3.21: Coumarin 6 emission and absorption spectra.

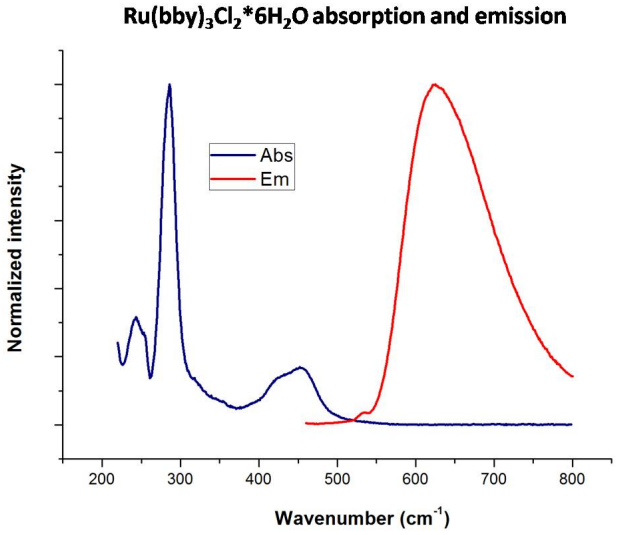

Figure 3.22: $Ru(bby)_3Cl_2*6H_2O$ emission and absorption spectra.

Dye	Absorption wavelength (nm)	Emission wavelength (nm)
Rhodamine 590	525	547
Coumarin 6	460	500
$Ru(bby)_3Cl_2*6H_2O$	286,452	625

Table 3.6: Emission and absorption of the dyes, dissolved in ethanol, used during the thesis.

Moreover, the fluorescence of the dyes embedded in the bare and pegylated NPs were measured and are shown as follows.

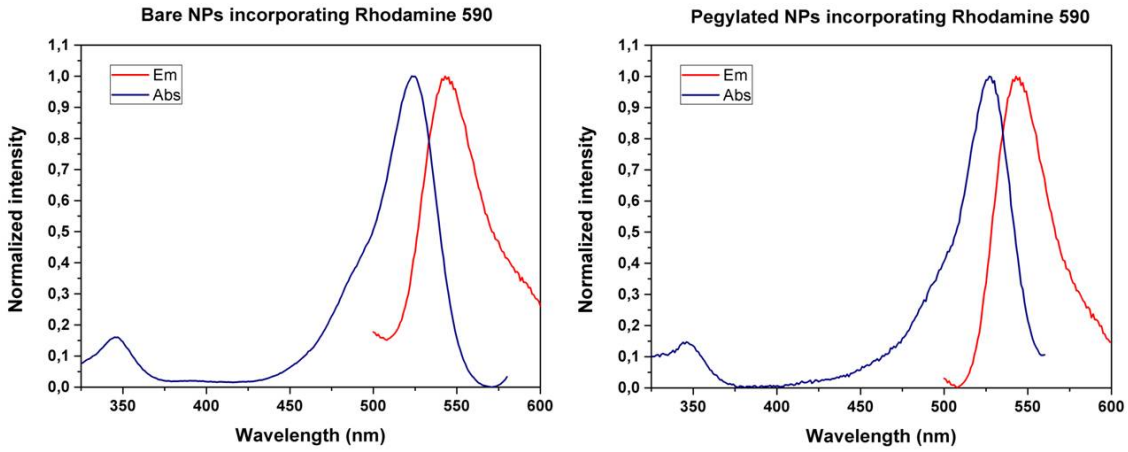

Figure 3.23: Emission and absorption of bare and pegylated NPs incorporating Rhodamine 590 (S2YRh, S2Y500aRh).

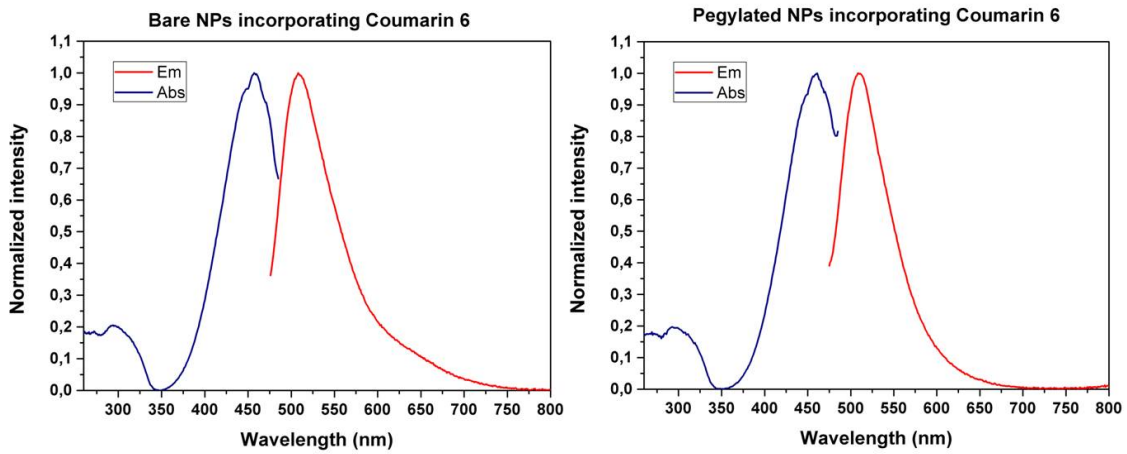

Figure 3.24: Emission and absorption of bare and pegylated NPs incorporating Coumarin 6 (S2YCu, S2Y500aCu).

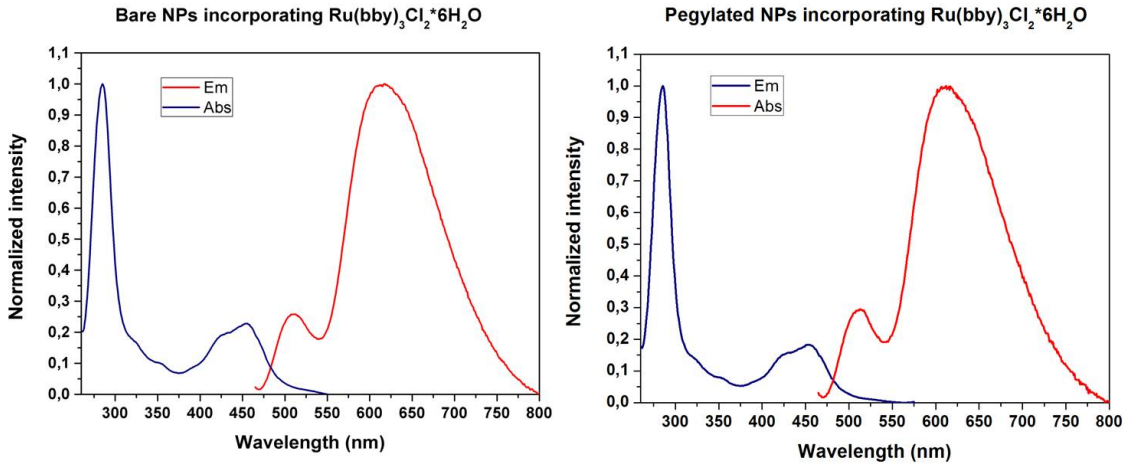

Figure 3.25: Emission and absorption of bare NPs incorporating $Ru(bby)_3Cl_2*6H_2O$ (S2YRu, S2Y500aRu).

In order to evaluate the size and the shape of the pegylated and bare NPs incorporating the dyes, SEM images were acquired. In figures 3.26 and 3.27 two representative images of fluorescent bare and pegylated NPs are shown. All the NPs had radii around 20 nm, and were easily dispersible, as in the previous synthesis.

In the light of above, the fluorescent bare and pegylated NPs were chosen for the next set of experiment in the biological field, such as the cells viability test, and the macrophages uptake.

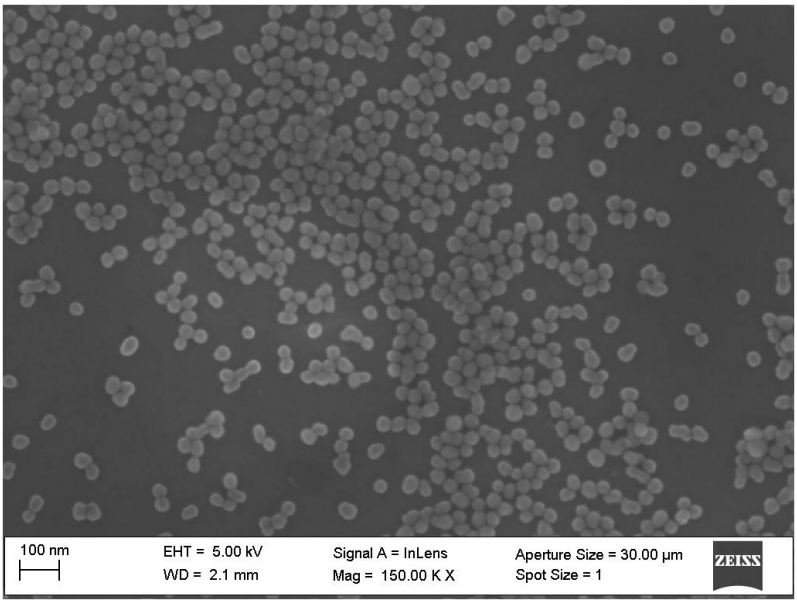

Figure 3.26: SEM image of fluorescent bare silica NPs incorporating Rhodamine 590 (S2YRh).

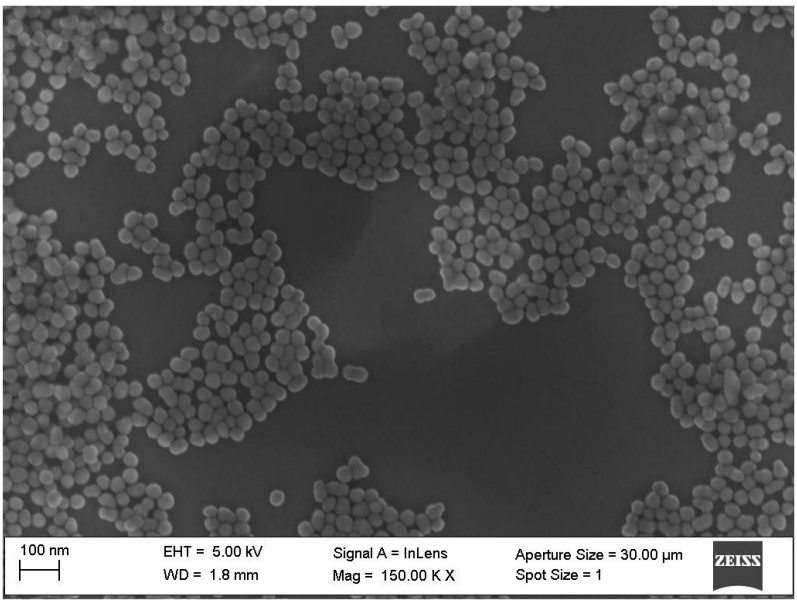

Figure 3.27: SEM image of fluorescent pegylated silica NPs incorporating Rhodamine 590 (S2Y500aRh).

3.2 Biological characterization

Six of the pegylated silica samples, respectively the more pegylated and the lower pegylated for each batch (S2y25a, S2y800a, S2y4b, S2y120b, S2y75a25b, and S2y25a75b) and the bare silica sample (S2y) were chosen for the biological characterization. Since they are supposed to show the more different behavior in the series, the pegylated samples were chosen in order to understand the effect of the PEG layer on the cells viability and the proteins adsorption on the NPs surface. In order to evaluate the cells viability after the

NPs incubation, three cell lines were used:

- RAW 264.7 murine macrophages;
- HEK 293 human embryonic kidney cells;
- Human fibroblasts.

All the samples were analyzed using the same conditions in terms of samples concentration and incubation days, in order to obtain an optimal reproducibility of the data. The viability test takes advantage of the change in colour due to the MTT reduction, metabolized only by the live cells, as described in the previous section. The orange colour produced by the mock-treated control cells, which are the cells that receive the same reagent treatment except for the NPs incubation, is quantified by means of absorption spectroscopy and corresponds to 100 % of cells viability. This reference value is reported in figures 3.28 and 3.29 for all samples at NPs concentration of 0,00 mg/ml. The cells viability of the NP treated cells was calculated as percentage between the optical density (OD) measured at each NP concentration with respect to the OD of the mock-treated control; the viability was evaluated after 24 hours and 48 hours from the NPs incubation. In figures 3.28 and 3.29 the viability data are shown after the NPs incubation with RAW 264.7 cells at 24 hours and 48 hours.

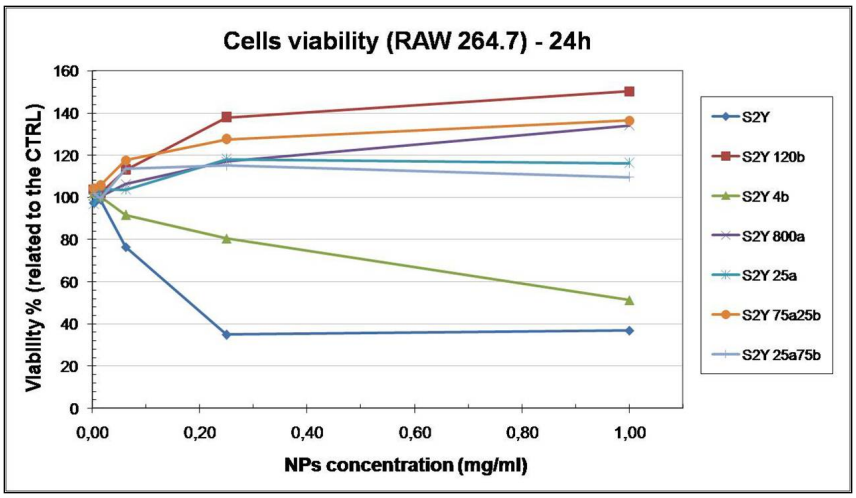

Figure 3.28: Viability data after the NPs incubation with RAW 264.7. The data were acquired after 24 hours.

After 24 hours, samples S2Y and S2Y4b seem to be the more toxic for the murine macrophages, while the other five samples (S2Y120b, S2Y800a, S2Y25a, S2y75a25b, and S2y25a75b) are better tolerated. In line with the data reported in the section 1.3, the more toxic samples are respectively the bare silica NPs and the one pegylated with the lower amount of PEG-silane 550. After 48 hours, the toxicity of all the samples is enhanced, in particular samples S2Y, S2Y4b, S2Y120b and S2Y25a are more toxic than the others.

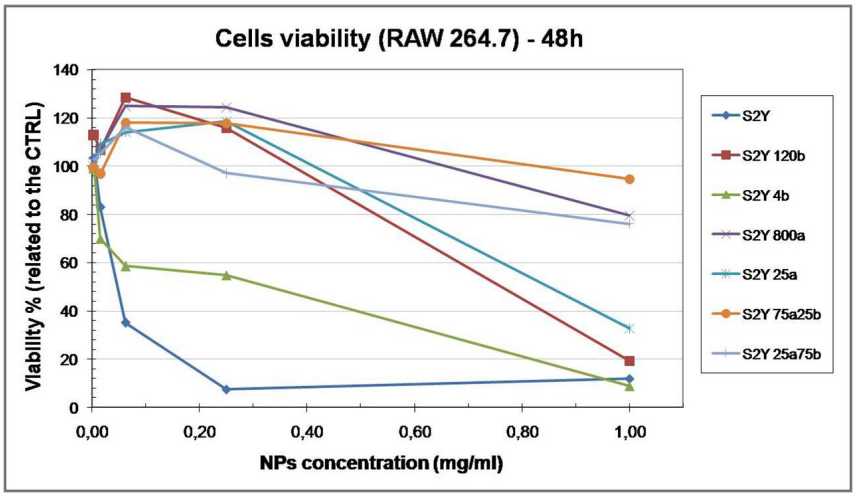

Figure 3.29: Viability data after the NPs incubation with RAW 264.7. The data were acquired after 48 hours.

The viability data were also acquired on the HEK 293 cells, as shown in figures 3.30 and 3.31. As in the previous viability test, the orange colour produced by by the mock- treated control cells, is taken as the reference value (NPs concentration 0,00 mg/ml).

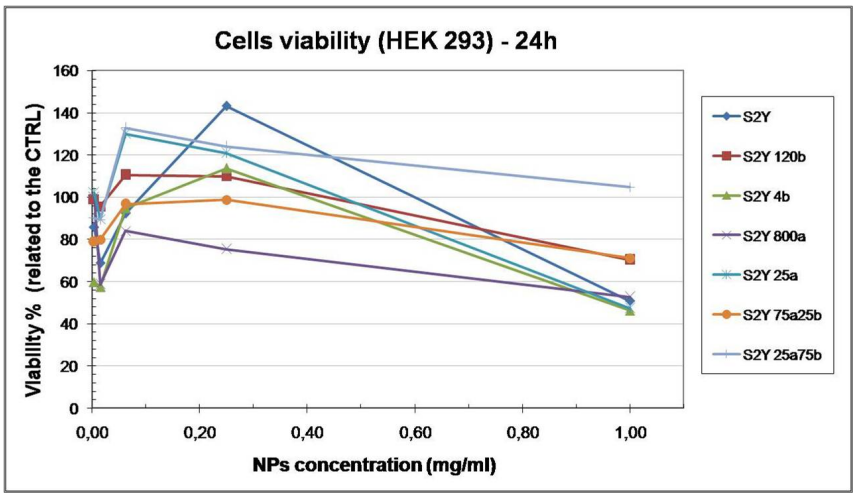

Figure 3.30: Viability data after the NPs incubation with HEK 293. The data were acquired after 24 hours.

As shown in figures 3.30 and 3.31, all the samples are quite biocompatible. Differently from the previous experiment, the NPs toxicity after 48 hours is not significantly enhanced compared to the toxicity after 24 hours.

In order to test the NPs toxicity on a healthy cell line, we worked on the fibroblasts cells. The data are shown in figures 3.32 and 3.33.

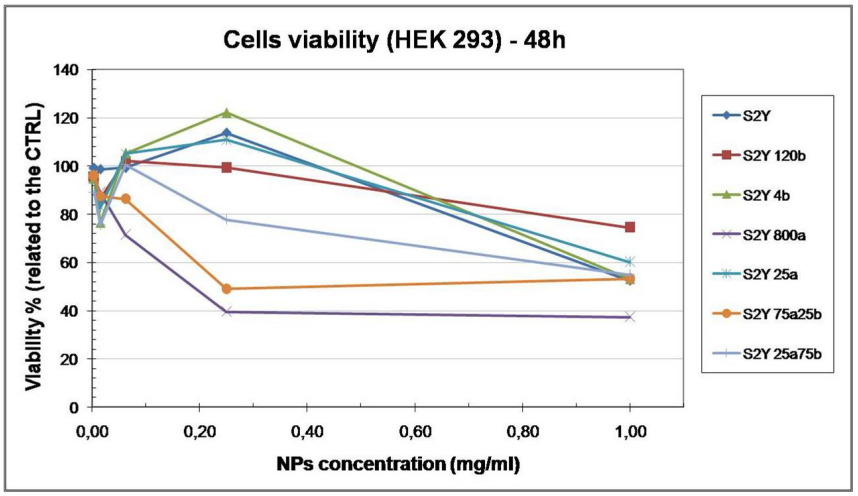

Figure 3.31: Viability data after the NPs incubation with HEK 293. The data were acquired after 48 hours.

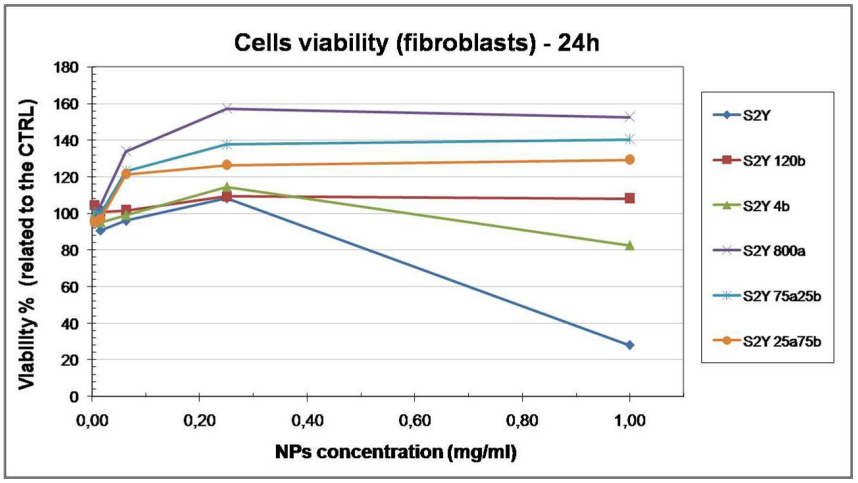

Figure 3.32: Viability data after the NPs incubation with human fibroblasts. The data were acquired after 24 hours.

Also in this experiment, such as in the previous ones, the orange colour produced by by the mock-treated control cells is taken as the reference value (NPs concentration 0,00 mg/ml). In figure 3.32 all the samples are biocompatible, except for the bare silica NPs (S2Y). After 48 hours (figure 3.33) the cells viability is quite similar to the viability measured at 24 hours.

Summarizing our results on the cell viability assays we can highlight some points. The RAW 264.7 macrophages are more prone to ingest the "non-self" compounds than the fibroblast and the HEK 293 cells, leading to a reduced viability after 48 hours, as shown in figure 3.28. The increasing in cell viability measured with the MTT assay may be due to some events. The ingestion or the interaction with NPs could stimulate the cellular redox system and therefore improve the staining of the medium. Moreover, the surface cell receptors could also be activated by the interaction with the NPs, leading to a change

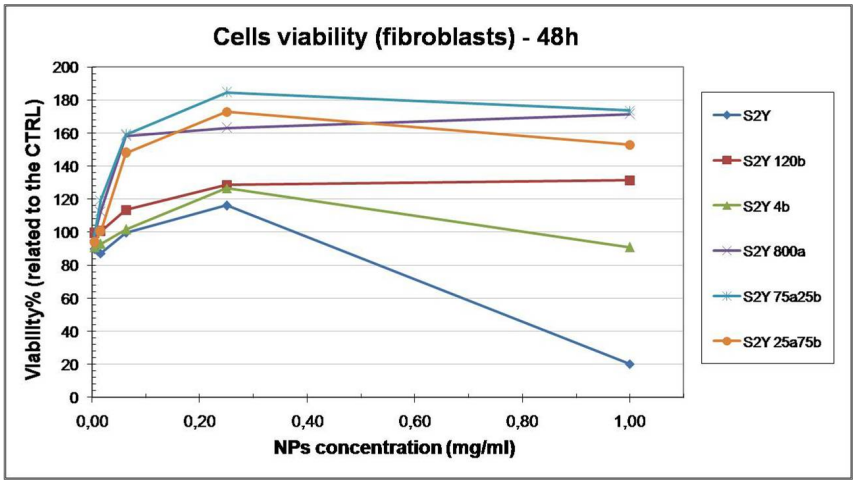

Figure 3.33: Viability data after the NPs incubation with human fibroblasts. The data were acquired after 48 hours.

in cellular homeostasis, and to an enhanced cellular proliferation. Therefore we have also analysed by optical microscopy the wells where we have measured higher cell viability with respect to the mock-treated control. We have observed that there were very low differences in the cell number among these wells. So we can conclude that the higher viability is not due to cell proliferation but to an increasing in the redox system activity.
In addition to these observations, for all the cell lines the NPs toxicity after 48 hours seems to be enhanced compared to the toxicity after 24 hours. We hypothesized that the reason should be due to the formation of a thick NPs layer over the cells surface,leading to an impair in their functions.
To sum up the results of the cells viability tests, the bare silica NPs (S2Y) and the samples pegylated with a lower amount of PEG (S2Y4b and S2Y25a) result more toxic for all the cell lines tested; therefore we can conclude that the masking of the NP surface with PEGs increase the biocompatibility.

As described in the previous section and reported in literature (section 1.2.2), the proteins adsorption onto the NPs surface affect the immune system response, the cellular uptake, the clearance, the biodistribution, and the internalization processes. Moreover the PEG coverage not only promote the internalization process, improve the stability, and make the NPs stealth, but also limit the proteins adsorption and the phagocytic process. In the light of above, in order to evaluate the different proteins adsorption onto bare and pegylated NPs surface, BSA and human serum proteins adsorption were tested. The analysis were performed using an SDS electrophoresis gel protocol.
The optimal BSA concentration for the experiment is reported in literature and is very similar to the albumin value measured in the human blood: $3,5$ g/dl - $5,5$ g/dl [47, 48]. The pegylated and bare NPs (same samples of the previous analysis), were incubated with BSA (50 mg/ml) at 37 °C for 1 hour, as described in the experimental section. Then the samples (40 µg of NPs) were loaded into the SDS electrophoresis gel together with the

three BSA standards (1 µg, 2 µg, 5 µg from a stock solution of BSA 50 mg/ml).

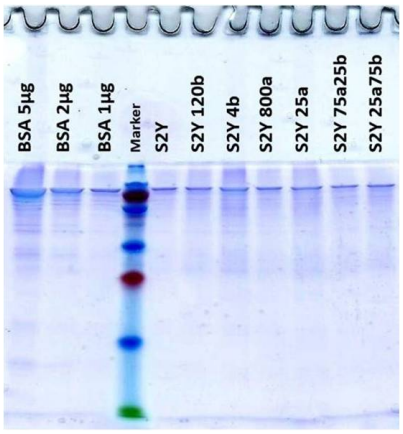

Figure 3.34: SDS-electrophoresis gel about the BSA adsorption onto the NPs surface.

As shown in figure 3.34, BSA was adsorbed onto the surface of all the samples analyzed. Specifically, the bare silica NPs (S2Y) and the ones pegylated with the lower amount of PEG (S2Y4b and S2Y25a) adsorbed an higher amount of BSA onto their surface. In order to make more clear this consideration, the data were processed using ImageJ. First the electrophoresis gel image (figure 3.34) was converted to a black and white image. Following, the brightness/contrast was adjusted, the grey amount of each bands was plotted as a peak-shape function, and then the area under the curve was calculated. The data obtained are shown as follows, in figure 3.35.

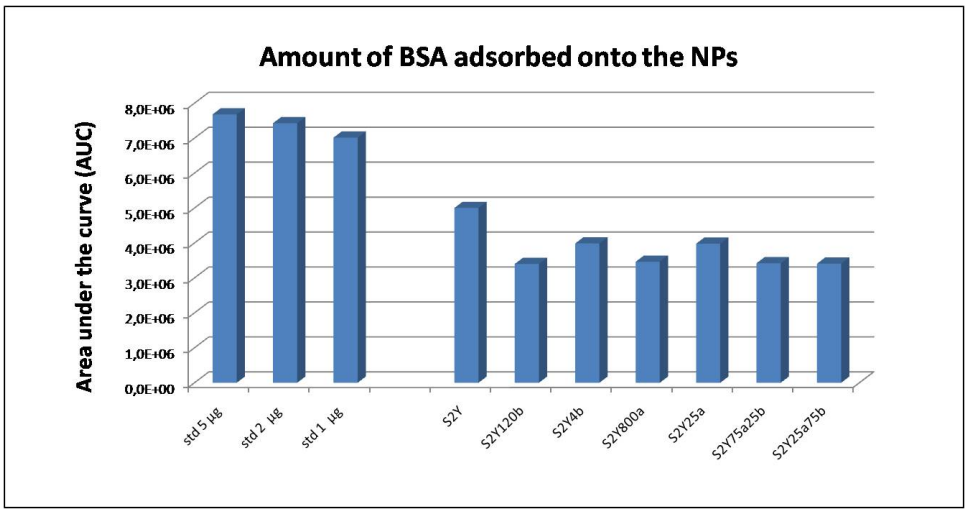

Figure 3.35: Data related to the BSA adsorption onto the NPs surface.

In order to make a semi-quantitative analysis of the amount of the adsorbed BSA, the samples data were compared to the BSA standard data and the result are shown in table 3.7.

Samples	BSA amount (µg)
S2Y	0.71
S2Y120b	0.48
S2Y4b	0.57
S2Y800a	0.49
S2Y25a	0.57
S2Y75a25b	0.49
S2Y25a75b	0.48

Table 3.7: BSA amount adsorbed.

To sum up, all the obtained data, the BSA adsorption is higher onto the bare sample (S2Y) and the lower pegylated (S2Y4b, S2Y25a) samples.
In order to confirm the data obtained using a commercial and purified BSA, the same protocol previously described, was used to test the interaction with human serum proteins. As described in section 1.3 the albumin is one of the most abundant proteins of the human serum, together with the fibrinogen, and the globulins. In figure 3.36 the data related to the human serum proteins adsorption are shown.

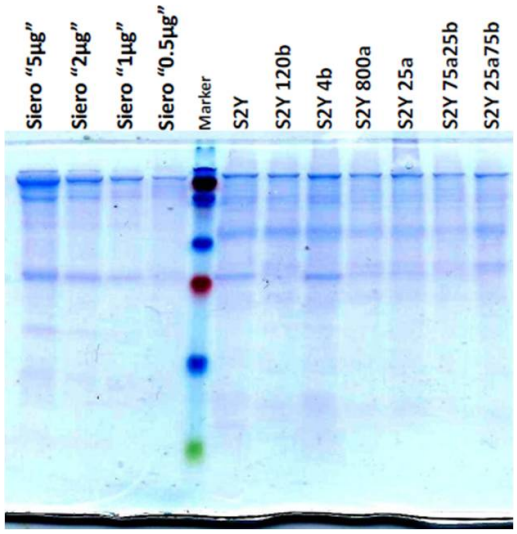

Figure 3.36: SDS-electrophoresis gel about the human serum proteins adsorption onto the NPs surface.

The gel data were than processed using ImageJ, using the same conditions described above, in order to obtain a semi-quantitative analysis. In figure 3.37 the results are shown. In table 3.8 the data related to the comparison between the samples and the standards are shown.

Samples S2Y and S2Y4b adsorb a higher amount of human serum proteins, confirming the data obtained in the previous experiment with BSA. As previously studied in literature

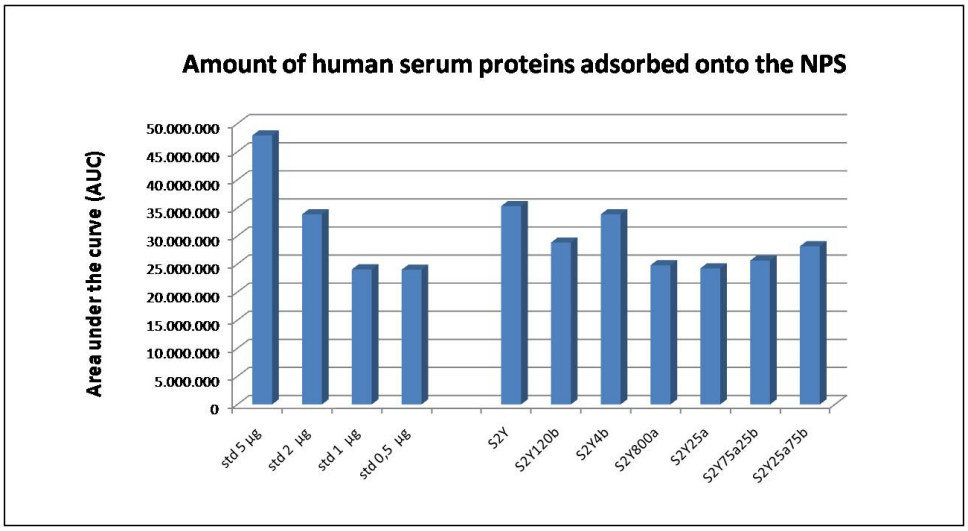

Figure 3.37: Data related to the human serum proteins adsorption onto the NPs surface.

Samples	BSA amount (µg)
S2Y	1.47
S2Y120b	1.19
S2Y4b	1.40
S2Y800a	1.03
S2Y25a	1.00
S2Y75a25b	1.06
S2Y25a75b	1.10

Table 3.8: Human serum proteins amount adsorbed.

[76], and in reference to the molecular weight of the marker, it is assumed that the other bands shown in figure 3.36 can be the globulins, another important component of the human serum.

Moreover, in order to evaluate if the insufficient PEG coverage can be made more effective by the BSA adsorption, the cells viability tests were repeated using a different protocol. After the NPs pre-incubation with BSA at 37 °C for 1 hour, the NPs were then incubated with the same cell lines used in the previous set of experiments. Only the more toxic samples were chosen for this experiment: the bare silica NPs (S2Y) and the pegylated ones (S2Y4b and S2Y25a). In order to make a comparison between the BSA adsorption onto the NPs and the related controls, which were not previously incubated with BSA, the NPs toxicity was evaluated for six samples (S2Y-BSA, S2Y4b-BSA, S2Y25a-BSA and S2Y, S2Y4b, S2Y25a). The data related to the NPs-BSA incubation with the RAW 264.7 macrophages are shown in figures 3.38 and 3.39.

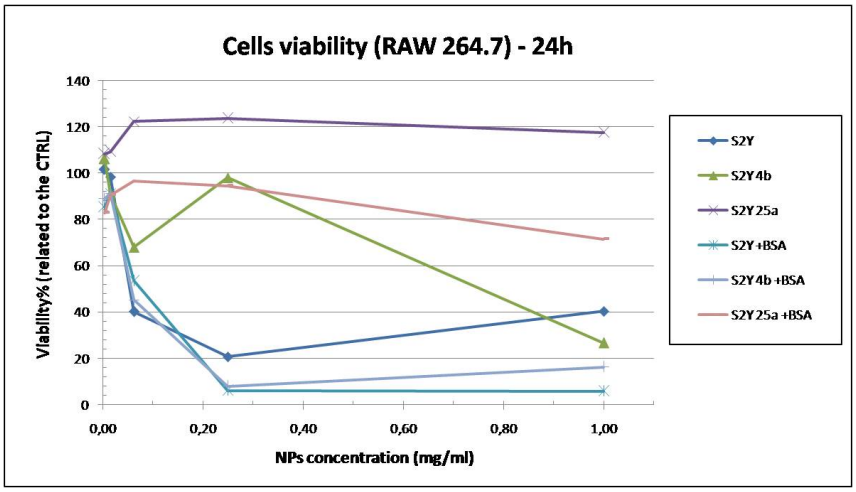

Figure 3.38: Viability data after the NPs-BSA incubation with RAW 264.7 macrophages. The data were acquired after 24 hours.

As shown in figure 3.38, all the samples incubated with BSA seem to be more toxic for the RAW 264.7 macrophages than the related controls (without BSA on their surface). The same situation is shown also in figure 3.39, after 48 hours. Actually the BSA coverage onto the NPs should have a masking effect towards the cells, as reported in the literature [77]. However, this phenomenon is in accordance with the data reported in the last decades literature about the macrophages. Poteser et al. in their experimental work demonstrate the presence of albumin receptors onto the macrophages surface [78], leading to a enhanced NPs-BSA phagocytosis, rather than the NPs without the BSA coverage.

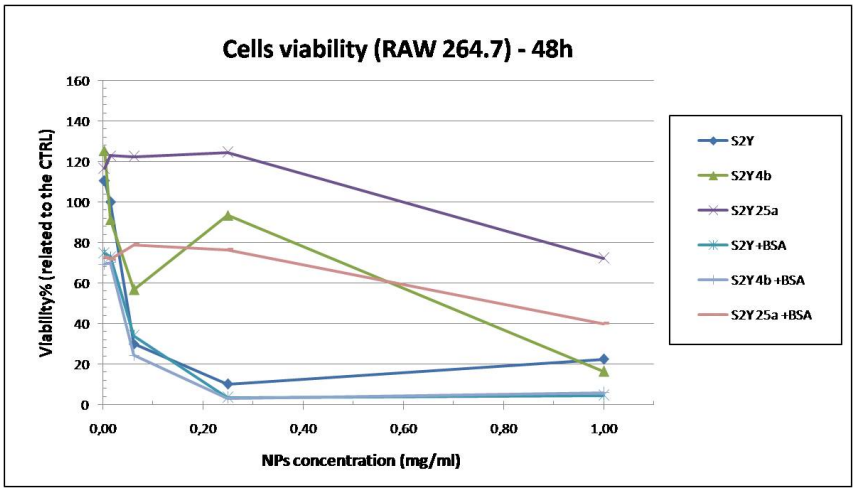

Figure 3.39: Viability data after the NPs-BSA incubation with RAW 264.7 macrophages. The data were acquired after 48 hours.

The same protocol was applied to the HEK 293 cells. The cells viability was acquired at the same conditions of the previous experiment, and the data related to the NPs incubation

with the HEK 293 cells, are shown in figures 3.40 and 3.41.

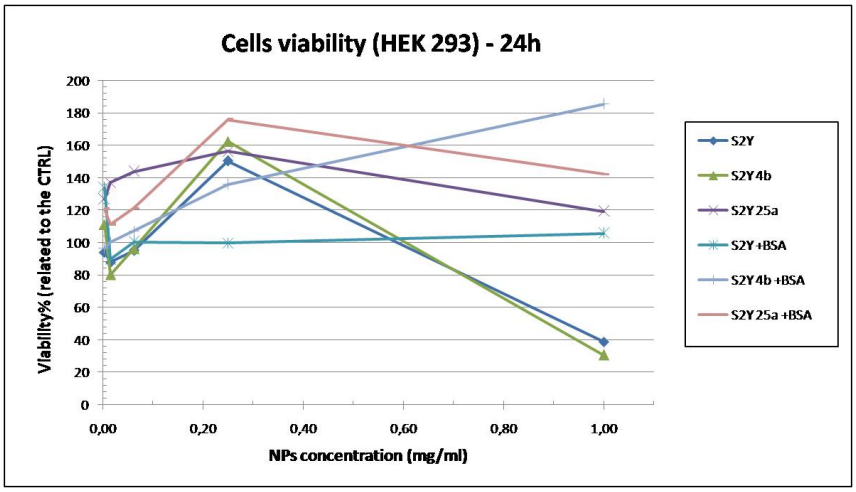

Figure 3.40: Viability data after the NPs-BSA incubation with HEK 293. The data were acquired after 24 hours.

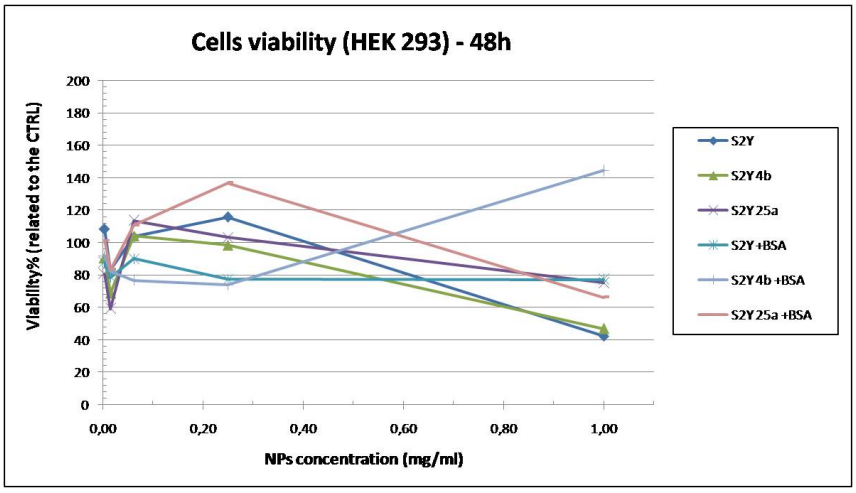

Figure 3.41: Viability data after the NPs-BSA incubation with HEK 293. The data were acquired after 48 hours.

Differently from the previous experiment, in which the macrophages were used, the toxicity of the NPs-BSA on the HEK 293 cells, is reduced, as shown in figures 3.40 and 3.41. This phenomenon is in accordance with the data reported in literature; Frölich et al. demonstrated that the BSA adsorption onto the NPs surface can mask them towards the cells, leading to a reduced NPs toxicity [77].
The same phenomenon is shown in figures 3.42 and 3.43, in which the cells viability was evaluated on the human fibroblasts. Samples S2Y, S2Y4b and S2Y25a are more toxic then the related samples with the BSA coverage (S2Y-BSA, S2Y4b-BSA and S2Y25a-BSA).

To sum up, all the samples adsorb BSA onto their surface, but samples S2Y, S2Y25a, and S2Y4b show a higher interaction with BSA. According to the literature [79], the BSA

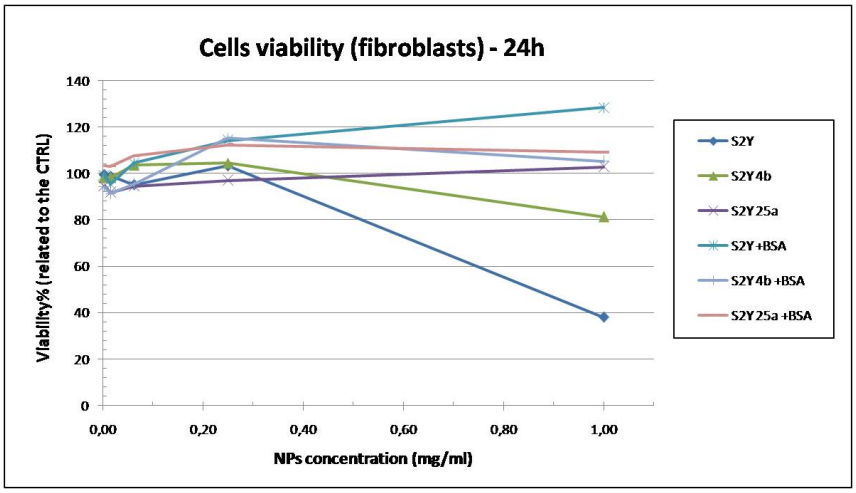

Figure 3.42: Viability data after the NPs-BSA incubation with human fibroblasts. The data were acquired after 24 hours.

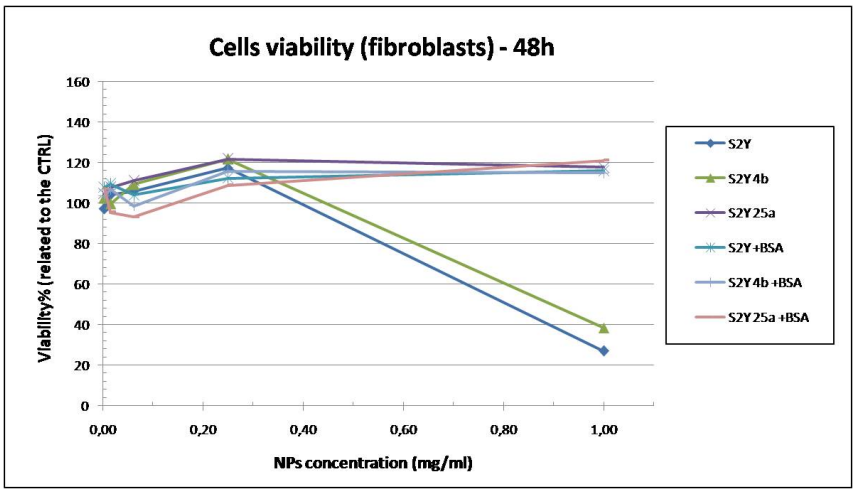

Figure 3.43: Viability data after the NPs-BSA incubation withhuman fibroblasts. The data were acquired after 48 hours.

adsorption can have a NPs masking effect towards the cells, leading to a less internalization, and consequently to a reduced NPs toxicity (figures 3.42 and 3.40). However, as described above, the BSA adsorption onto the NPs surface can cause an enhanced internalization by the macrophages, leading to a lower cells viability (figure 3.38). This phenomenon is shown only for the cells which have BSA receptors on their surface, such as the RAW 264.7 macrophages [78].

In order to test the potential applications of the silica NPs, such as the imaging, fluorescent bare and pegylated silica NPs were synthesized (S2Y and S2Y500a). Three different dyes were used, as described in experimental section: Rhodamine 590, Coumarin 6, and $Ru(bby)_3Cl_2$*$6H_2O$. First the cells viability after the incubation with the fluorescent NPs was evaluated using RAW 264.7 macrophages and human fibroblast. In figures 3.44 and

3.45 the cells viability data are shown.

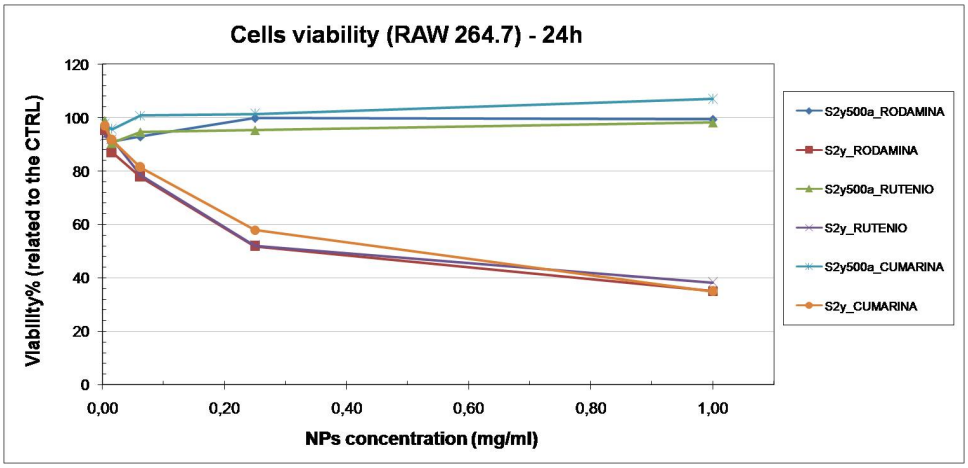

Figure 3.44: Viability data after the fluorescent NPs incubation with RAW 264.7 macrophages. The data were acquired after 24 hours.

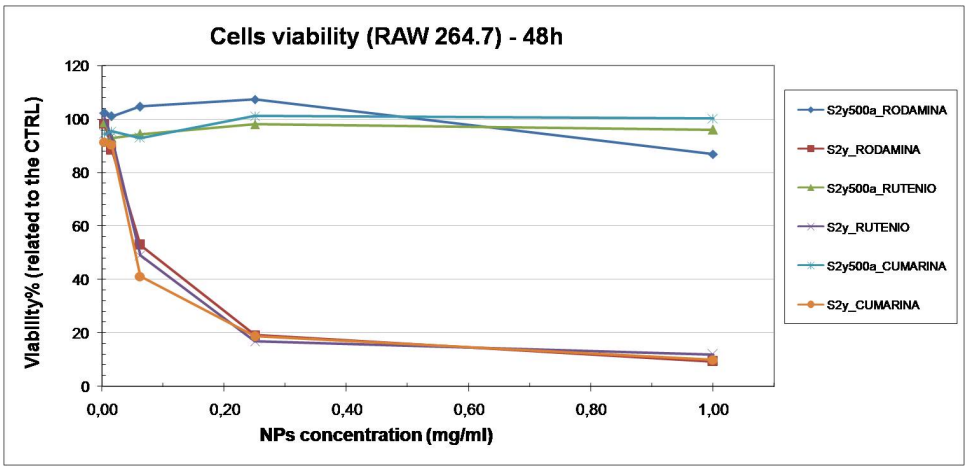

Figure 3.45: Viability data after the fluorescent NPs incubation with RAW 264.7 macrophages. The data were acquired after 48 hours.

At 24 hours, but also at 48 hours, all the bare fluorescent silica NPs are toxic for the macrophages, while the pegylated ones are totally biocompatible. The data related to the human fibroblasts viability after the fluorescent NPs incubation as shown as follows.

In figures 3.46 and 3.47 the toxicity of the bare fluorescent samples is shown, while the pegylated ones are totally biocompatible, confirming the data obtained in the previous set of experiments.

The NPs fluorescence was then analyzed using a flow cytometer and the data are shown in figure 3.48. After testing all the possibile combinations in terms of laser excitation and filters to be used, the phycoerythrin (PE) channel was choosen for subsequent analyses. Bare (S2Y) and pegylated (S2Y500a) silica NPs were tested using the same conditions in terms of sample concentration and excitation laser. As a reference value, non-fluorescent

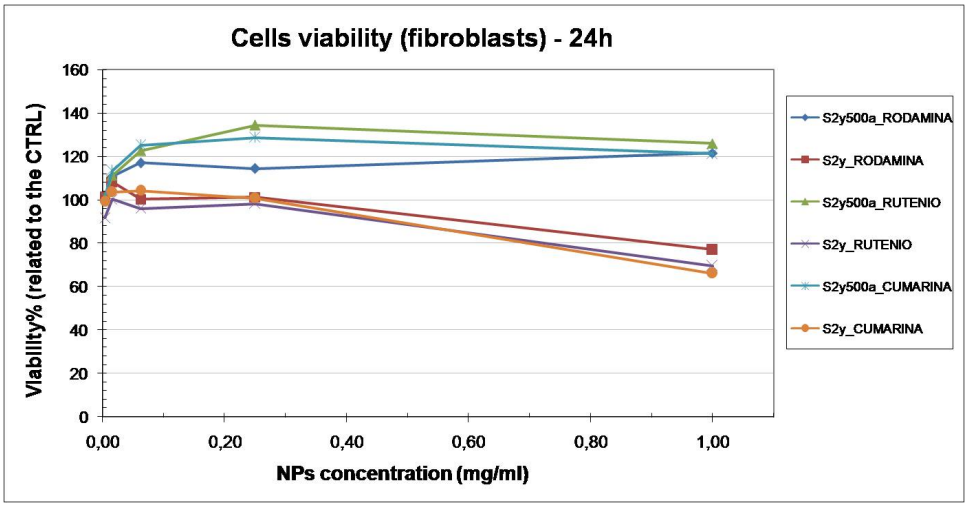

Figure 3.46: Viability data after the fluorescent NPs incubation with human fibroblats. The data were acquired after 24 hours.

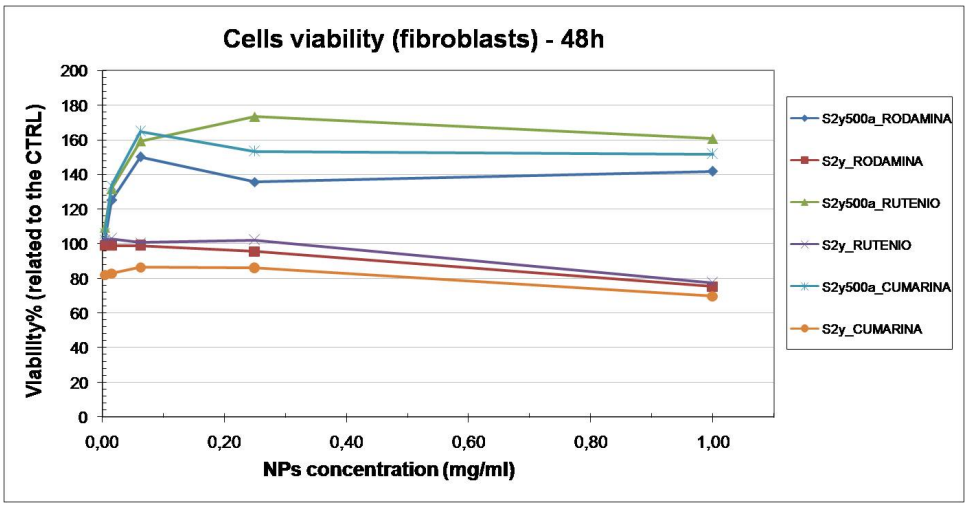

Figure 3.47: Viability data after the fluorescent NPs incubation with human fibroblasts. The data were acquired after 48 hours.

bare silica NPs were also tested.

In figure 3.48 the data related to the NPs fluorescence are shown. The fluorescence of all the samples is clearly visible related to their control, except for the samples incorporating Coumarin 6, which cannot be detected by the setting of the instrument used. Admittedly, the luminescence of the NPs synthesized in the presence of coumarin was hardly observable under a common UV-lamp. This suggests a rather poor incorporation of the dye in the silica network of the NPs.

The fluorescence of bare silica NPs incorporating Rhodamine 590 is enhanced of about 20-times with respect to the pegylated one. The reason should be searched in the thickness of the PEG layer around the NPs, which reduce the dye efficiency and the fluorescence emission. However, the fluorescence of bare and pegylated samples incorporating

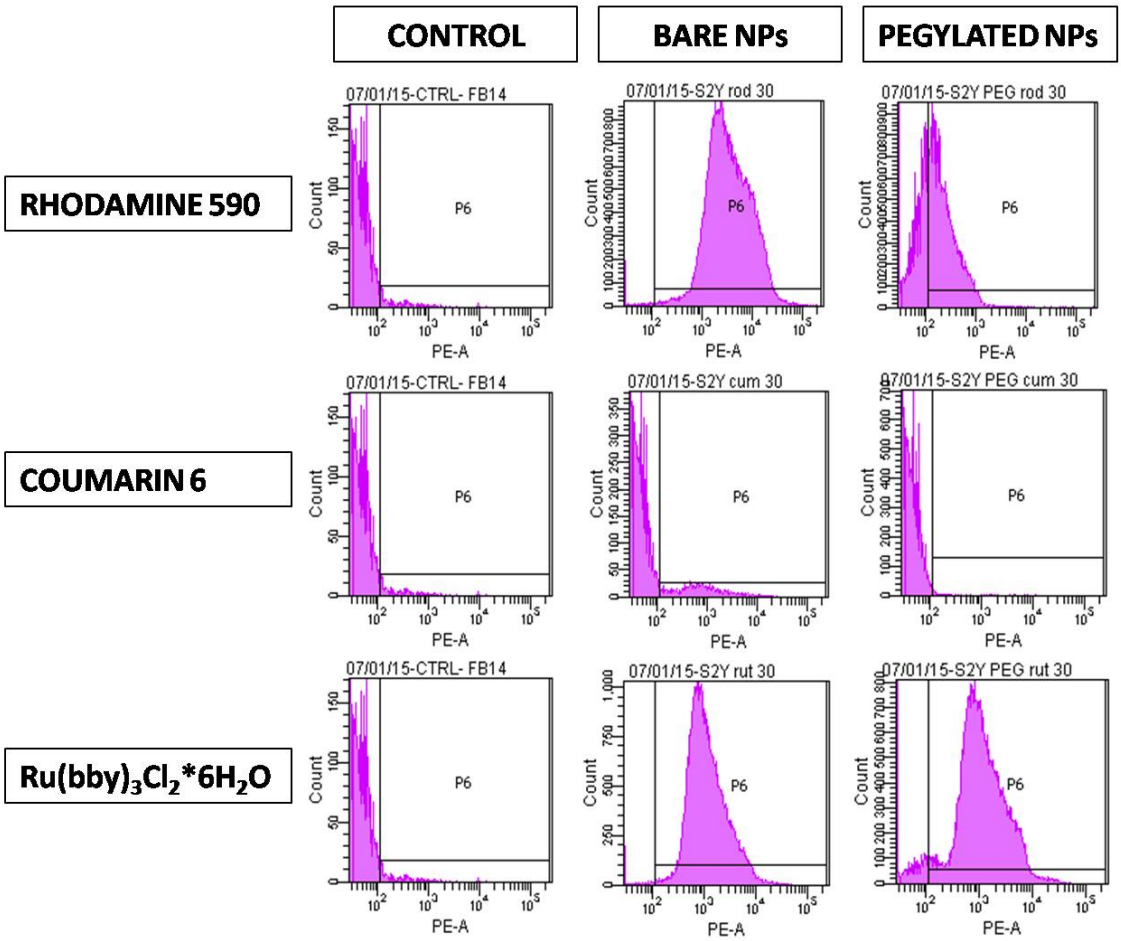

Figure 3.48: Data related to the NPs fluorescence obtained using the flow cytometer.

$Ru(bby)_3Cl_2*6H_2O$ is almost unchanged. The reason for this behavior is not clear. It is possible that Rhodamine 590 has tendency to remain in the outer shell of silica NPs or even adsorbed on their surface. In this view PEG chains might interact or even displace the dye molecule, leading to a reduced luminescence efficiency. In the case of $Ru(bby)_3Cl_2*6H_2O$ the metal center imparts a positive charge, which could promote a stronger interaction with the NPs during their growth. The metal complex could be embedded more homogeneously in the silica network, thus preventing the interaction with PEG chains. Further studies are needed to confirm these hypotheses.

As describe in sections 1.1.1 and 1.2.2, the PEG coverage can influence not only the cells viability and the proteins adsorption, but also the NPs uptake by the cells. In order to evaluate the different NPs uptake by the cells, bare and pegylated fluorescent silica NPs were used. In the light of the results obtained in figure 3.48, only the fluorescent silica NPs incorporating Rhodamine 590 and $Ru(bby)_3Cl_2*6H_2O$ were used. The uptake was evaluated after 24 hours from the incubation of the NPs (0.35 mg/ml) with the RAW 264.7 murine macrophages.

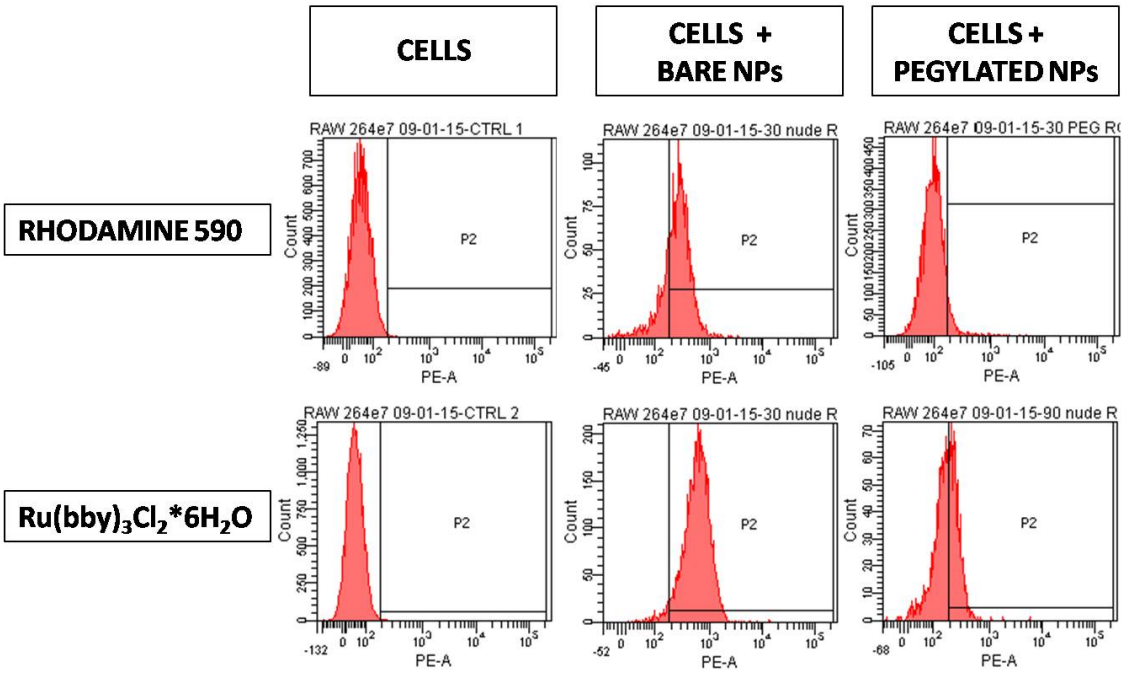

Figure 3.49: Data related to the NPs uptake by the macrophages obtained using the flow cytometer.

Confirming the data obtained in figure 3.48, also after the macrophages uptake, the bare silica NPs fluorescence is higher than the fluorescence of the pegylated one. The same phenomenon is shown for both the fluorescent samples. In order to evaluate the change in fluorescence after the NPs uptake by the macrophages, figures 3.48 and 3.49 were compared and the results as shown as follows (figures 3.50 and 3.51).

As shown in figure 3.50 the bare NPs fluorescence is drammatically reduced after the macrophages uptake, in great measure for the sample which incorporate the Rhodamine 590. The reason should be searched in the viability test, in which S2Y sample resulted toxic for the macrophages, leading to an enhanced cells mortality. Actually the flow cytometry analysis can be affected by cells mortality, because the dead cells are not screened by the instrument, leading to a loss of fluorescence. The same effect, even if less pronounced, is shown for the pegylated NPs, as shown in figure 3.51. The PEG layer around the NPs not only makes them biocompatible, leading to a reduced cells mortality, but also reduces the fluorescence. A similar situation is shown for the samples which incorporate the $Ru(bby)_3Cl_2*6H_2O$.

To sum up, all the samples were internalized by the macrophages, independently from the PEG coverage. Specifically, it has been demonstrated that the PEG layer affected the NPs toxicity and their fluorescence.

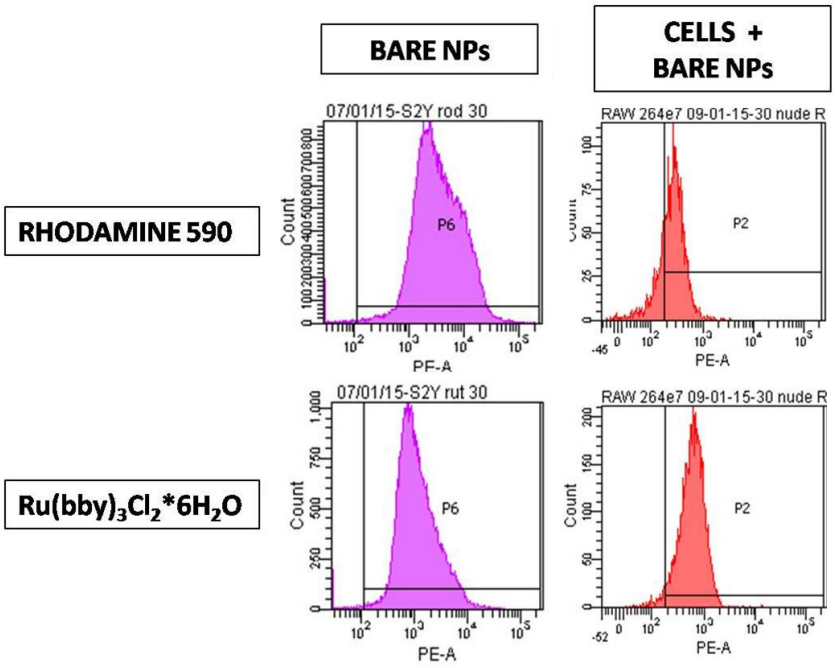

Figure 3.50: Data related to the comparison between the bare NPs fluorescence and the bare NPs fluorecence after the macrophages uptake.

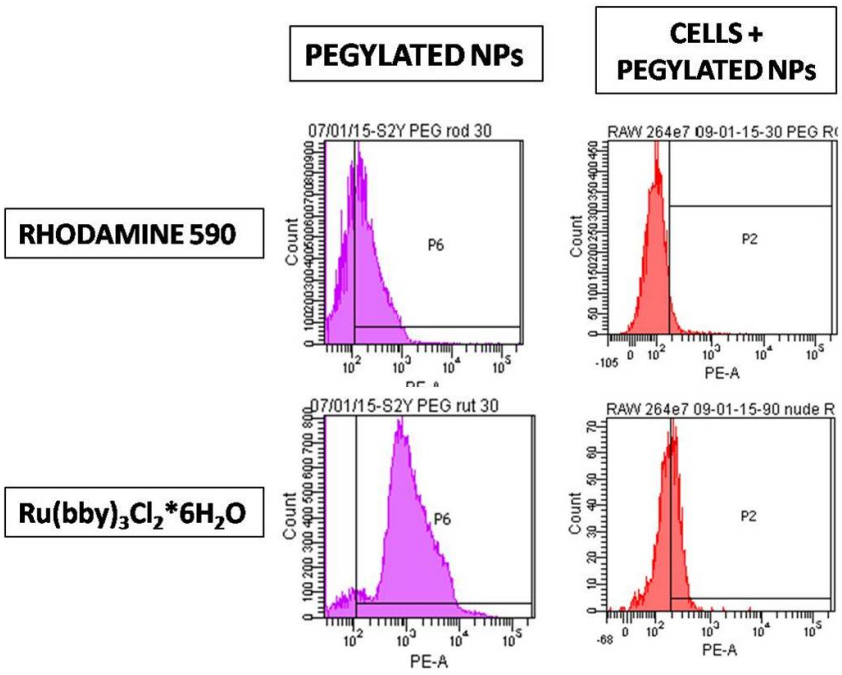

Figure 3.51: Data related to the comparison between the pegylated NPs fluorescence and the pegylated NPs fluorecence after the macrophages uptake.

Chapter 4

Conclusions

4.1 Resume of the work

In this thesis I have demonstrated an easy, reproducible, and economic synthesis protocol for pegylated Stöber silica NPsm confirming the effective PEG grafting onto the samples using the one-pot pegylation protocol, leading to the stability of the NPs in water and PBS. This pegylation protocol allows to obtain both pegylated and bare NPs from the same reaction batch, leading to the preservation of the NPs features, such as the size, the shape, and the size distribution. Moreover also the presence of different PEG amount grafted onto the NPs surface can be demonstrated using the TG and IR spectroscopy analyses.

The samples synthesized, both the bare and the pegylated NPs, have comparable radii, are easly dispersible, and free from large aggregation phenomenon, as confirmed by the SEM analyses. The stability of the samples in water is confirmed from DLS and ζ potential analyses.

According to the biological characterization, the NPs show a good biocompatibility with all the cell lines used, both tumoral and healthy cells, which confirm the masking effect of the PEG layer, except for the less pegylated samples and the bare ones, which show a higher toxicity against the same cell lines. Moreover, the PEG layer also limits the proteins absorption, such as the BSA, the most abundant protein in the human body, and the human serum proteins. In those cases in which the PEG coverage of the NPs surface is not sufficient, it can be made more effective using the BSA absorption. Actually, after the BSA absorption, also the lower pegylated samples show a reduced toxicity against the cells, except on the machropages cells, which have albumin receptors on their surface, leading to an enhanced NPs phagocytosis, thus leading to the cells death.

In the light of above, the pegylated silica NPs synthesized seem to be a good support to be used in the biological field, because of their low toxicity and the reduced proteins absorption, leading to a reduced immune system response against them. Regarding to

the cancer therapy, the size of the samples synthesized allow the passive entry into the tumor sites, taking advantage of the EPR effect. Moreover, the stability and the lack of aggregation, avoid the thrombus formation.

Regarding to the imaging, the fluorescent NPs synthesized preserve the same properties of the previous synthesis, such as the size, the shape, the narrow distribution, and the easily dispersibility. However an engineering of the system should be required, choosing a dye which allows to preserve the optical properties. In the light of above, the $Ru(bby)_3Cl_2*6H_2O$ seems to be the best candidate. In order to confirm this hypothesis, the incorporation of dyes, which have positive metal centers, into the silica NPs should be done.

Definitely, the NPs synthesized during my thesis work seem to be good candidates to use in biological applications, in particular the pegylated ones. Actually the PEG allows to make the NPs stealth, prevent the proteins absorption on their surface, and consequently avoid the opsonisation process. Theoretically, the PEG layer onto the NPs should reduce the cellular uptake by the macrophages, as described in literature. Actually, in this thesis work the differences between the uptake of the pegylated and bare NPs can not be well appreciated, because of the higher mortality of the macrophages during the incubation with bare NPs, which can be resolved using shorter experiment time.

4.2 Future perspectives

A lot of progresses was done in the study of NPs as a support to be used in the biomedical applications, such as the cancer treatment. In literature the antibody conjugation to the NPs support is described. In order to improve the features of the NPs in this field, a pegylation with a different PEGs can be undertaken, such as the PEG-diamine, which allow to attach easily the antibody.
Moreover, a biodistribution analysis using an animal model should be considered, in order to understand which are the more involved organs in the NPs elimination process. Also the dissolution test in biological fluids and in an animal model might be of interest. Specifically, using the fluorescent NPs incorporating the ruthenium complex, the dissolution can be followed by the ICP-MS, both in the biological media and in an animal model.

In order to use this silica supports in molecular imaging, the incorporation of QDs, which have absorption and emission in the therapeutic window, might be of interest.

Chapter 5

Appendix

5.1 Appendix A - Techniques of analysis

5.1.1 Thermogravimetry

Thermogravimetric analysis (TGA) is a method of analysis in which changes in physical and chemical properties of the materials are measured as a function of the temperature. TG analysis provides some information about physical and chemical phenomena, like vaporization, adsorption, desorption, dehydration, decomposition, oxidation and reduction.

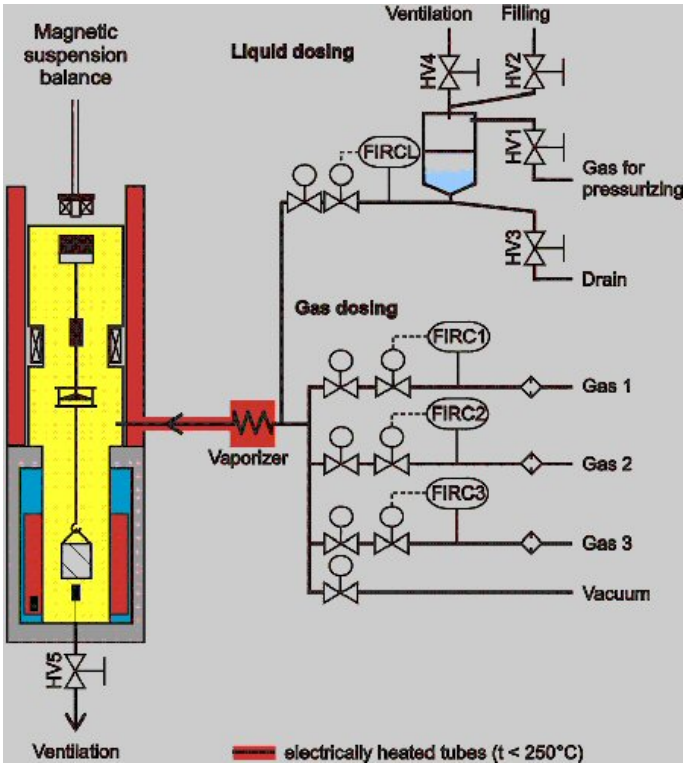

Figure 5.1: Scheme of a TG instrument for performing TG analyses.

Common applications of TGA are: analysis of the decomposition patterns, degradation mechanisms, kinetics, and determination of organic and inorganic content in the sample. This technique is well suited for the study of polymeric materials, like PEG. A TG analysis has three fundamental parameters: temperature, mass change, and temperature change. In order to obtain high degree of precision, an analitic balance and a programmable furnace, in terms of constant heating rate or constant mass loss with time, are required. Sample and reference sample are placed in a furnace, equipped with a thermocouple to monitor the temperature, and the atmospehere may be purged with nitrogen in order to prevent undesired reactions. While the temperature increases, the mass change is continuously mesaured. Results will be plotted with temperature on the X-axis and mass loss on the Y-axis. A scheme of TG instrument is shown in figure 5.1.

5.1.2 Infrared spectroscopy

Infrared spectroscopy technique is based on the specific absorption of the light, depending of the structure of the analyzed molecule. Infrared spectroscopy works in the infrared region of the spectrum and used low frequency ligth, whose wavelength is longer than the visible light. The infrared region can be divided in three parts: near (from $14\,000\,\mathrm{cm}^{-1}$ to $4000\,\mathrm{cm}^{-1}$), mid (from $4000\,\mathrm{cm}^{-1}$ to $400\,\mathrm{cm}^{-1}$) and far (from $400\,\mathrm{cm}^{-1}$ to $10\,\mathrm{cm}^{-1}$). The absorption of an infrared photon by a molecule leads to a transition from the vibrational ground state to the vibrational excited state. A linear molecule has 3N-5 vibrational modes, while a nonlinear molecule has 3N-6. The vibrational modes include changing of the bond angle (bending δ) and stretching of the chemical bond (stretching ν), as the most common. Moreover, changing of the angle between a group of atoms (rocking ρ), changing of the angle between the plane of a group of atoms (wagging ω), and changing of the angle between the planes of two groups of atoms (twisting τ) are characteristic IR vibrational modes as well. An IR spectrophotometer is composed of a light source, a monochromator that selects a specific wavelength, and a detector. Among the number of possible analysis configurations which are used, solid samples can be analyzed in the diffuse reflectance (DR) configuration: few milligrams of the sample are grounded with potassium bromide (KBr) and placed in the sample holder. An interferometer is used to record the spectrum (interferogram) which is in turn transformed via a Fourier transform in the final spectrum. This kind of analysis is known as Diffuse Reflectance Infrared Fourier Transform (DRIFT). Results will be plotted with wavelength on the X-axis and transmittance on the Y-axis. A scheme of Infrared spectroscopy (IR) instrument is shown in figure 5.2.

5.1.3 Scanning electron microscopy

SEM is a type of electron microscope that scans a sample, in a rectangular pattern, by a focused beam of electrons. When the electrons interact with the sample, they produce

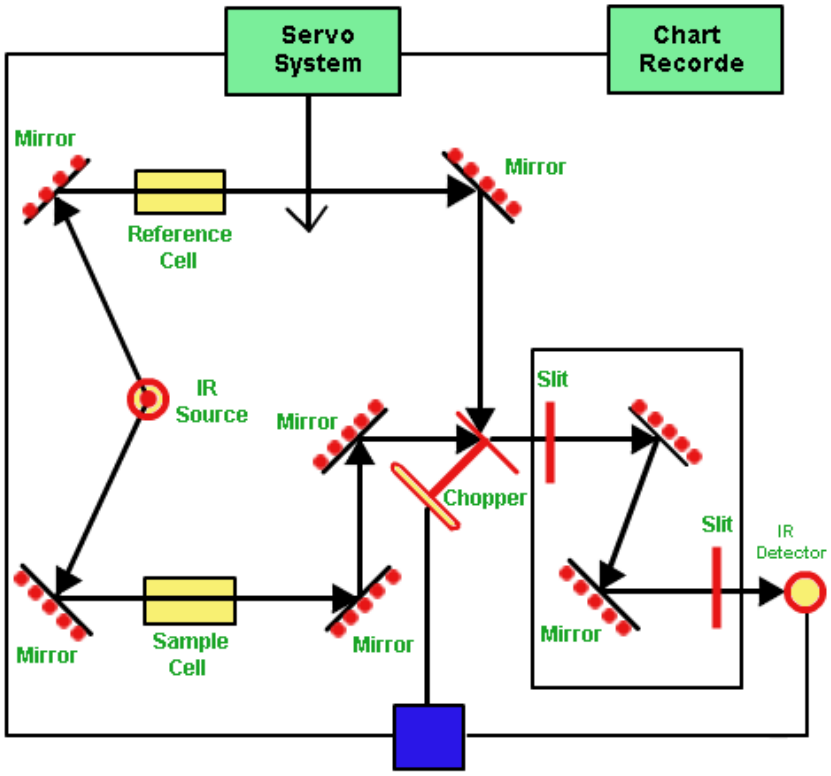

Figure 5.2: Scheme of a IR instrument for performing IR spectroscopy analyses.

various signals that will be different, depending on the composition and topography of the material. A SEM can produce different types of signals: back-scattered electrons, secondary electrons, X-rays and cathodoluminescence. The back-scattered electrons (BSE) are produced from the primary beam, by elastic interaction with the nuclei of the sample, so the signal will be proportional to the atomic number of the material. The secondary electrons (SE) are produced by the interactions between the valence electrons of the sample and the high energy electrons. They have an energy of about 50 eV, while the BSE have energies up to 50 keV. The SE belong to the surface of the material analyzed, which allow topographic measuraments, while the BSE, belonging to the deeper layers, are used for the compositional analyses. X-rays are used to understand the composition of the materials and measure the amount of the elements inside them, while the cathodoluminescence is the light emitted by the samples following the excitation by the electrons. A SEM reveals details of about 1 nm in size and because of the narrow beam, has a large depth of field. An electron microscope allows magnification 250 times higher than a light microscope and samples can be observed at different temperatures in wet conditions, high and low vacuum. A scheme of a SEM is shown in figure 5.3.

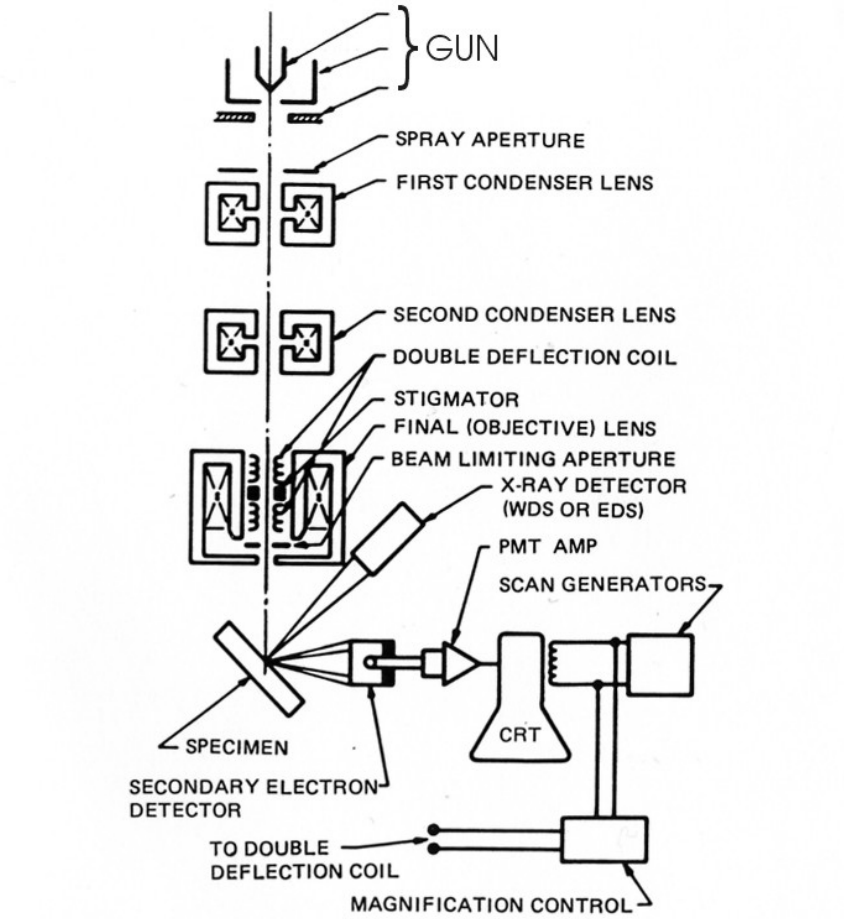

Figure 1.11. Schematic drawing of the electron and x-ray optics of a combined SEM–EPMA.

Figure 5.3: Scheme of a SEM for performing microscopy analyses.

5.1.4 Dynamic light scattering

DLS is a technique of physical characterization that is used to measure the hydrodinamic radius of the particles in solution. When the NPs are smaller than the wavelength used, the light is scattered elastically, a situation referred to as a Rayleigh scattering. The light intensity variation are produced by the Brownian motion, in which the smaller NPs move faster, while bigger ones are slower. This determines higher frequency of oscillations in the recorded scattered signal, while lower frequencies are observed in the signal from bigger NPs suspensions. The interpretation of these signals gives a correlation function which in turn gives the dimension of the NPs in the system.
During a DLS analysis, the PDI is really important, because it defines the uniformity of the size and distribution of the NPs. Values of PDI smaller than 0.4 are acceptable, while higher values reveal the presence of aggregates. Results are plotted with mean radius (nm) on the X-axis and the number of NPs on the Y-axis. Also the zeta potential can be evaluated, using a DLS instrument. ζ potential is measured at the "slipping plane": the interface between the charged surface of the particle and the media in which it is dispersed. It also

gives a measure about the colloidal stability of the particles and the repulsion between them. Interpretation of the values ofζ potential are shown in table 5.1. A DLS instrument is composed of a laser beam and a detector that received the scattered light, as shown in figure 5.4.

Zeta potential (mV)	Stability
from 0 to ±5	rapid flocculation
from ±10 to ±30	high instability
from ±30 to ±40	moderate instability
from ±40 to ±60	good stability
higher than ±60	high stability

Table 5.1: Stability of the particles related to their zeta potential (mV).

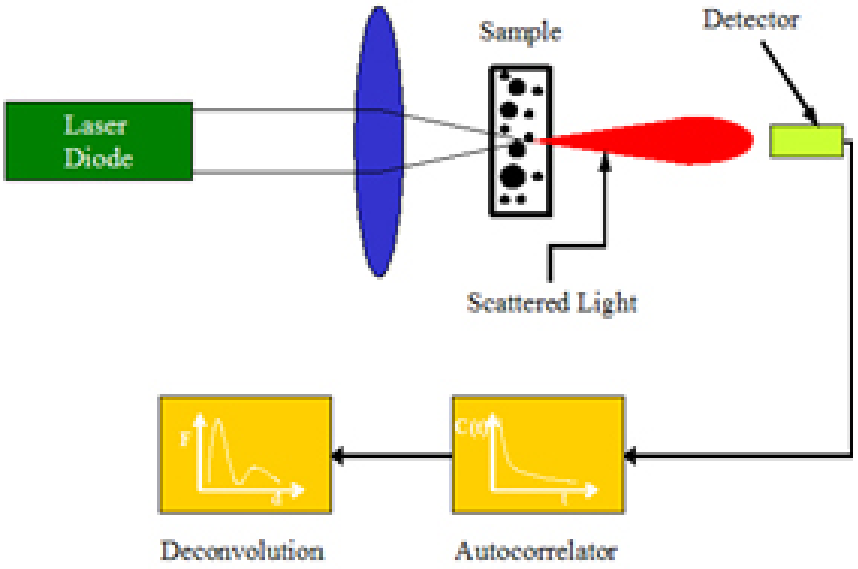

Figure 5.4: Scheme of a DLS instrument for performing size distribution and zeta potential analyses.

5.1.5 Small angle X-ray scattering

SAXS is a scattering technique that works in a range of angles between 0.1° and 10° and allows to obtain information about shape and size of the nanoparticles and pore sizes of the porous structures. This technique is based on the elastic scattering of the X-rays that have wavelengths between 0.1 nm and 0.2 nm. A SAXS instrument is composed of a monochromatic beam of X-rays and a detector that received the scattered X-rays as a bidimensional pattern (figure 5.5). Samples can be solid or liquid and simple to prepare. A SAXS analyses allow to study also lamellae and fractal materials and is a non-destructive

and accurate method of analyses.

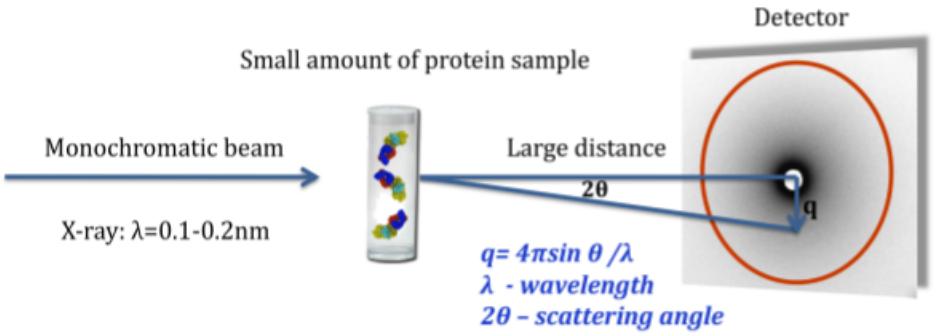

Figure 5.5: Scheme of a SAXS instrument for performing size and shape distribution analyses.

5.1.6 UV-visible spectrophotometry

UV-visible spectrophotometry is a technique based on the absorption of electromagnetic radiation, in a UV and visible range, by a molecule. A spectrophotometer is based on the Lambert-Beer law that states the absorbance (A) of a solution is proportional to its concentration and to the path length of the cuvette used :

$$A = \epsilon_\lambda \times l \times M \tag{5.1}$$

where ϵ_λ is the molar extinction coefficient, l the path length and M the molarity of the solution.
In a typical spectrophotometer there is a light source, a monochromator that choose the correct wavelength, a cuvette in which is contained the solution, a detector and a data analyses system, as shown in figure 5.6. A typical absorption spectrum shows the absorption versus the selected wavelength.

5.1.7 Flow cytometry

Flow cytometry is a laser-based techique that allows a real time cell sorting and cell counting. A flow cytometer is able to count thousand of cell every second and is composed of four different components:

- A liquid stream in which are dispersed the cell;
- A measuring and converting system;
- A computer;
- An amplification system.

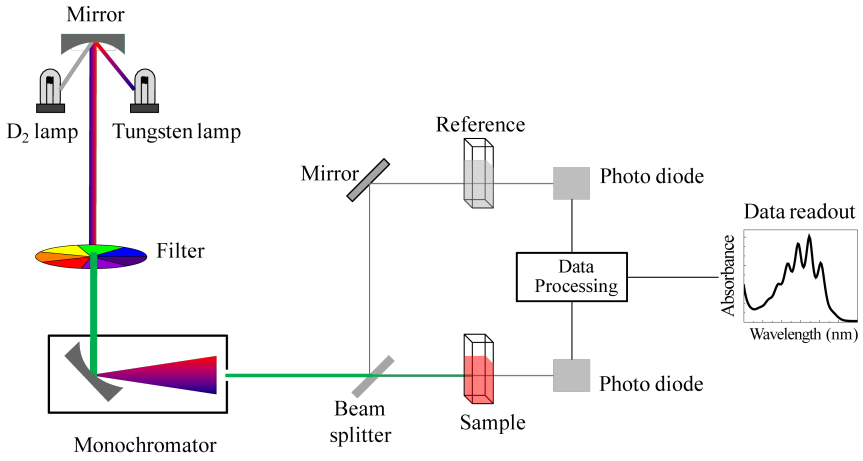

Figure 5.6: Scheme of a UV-visible spectrophotometer for performing absorption analyses.

Samples must have sizes between 0.2 µm and 14 µm and are labelled with a fluorescent dye, and excited by a laser. The emitted wavelengths are measured in order to obtain information about the type and the amount of the analyzed cells. Light signals are than converted into electronic signals by a converting system, ad subsequently to digital data. A scheme of a flow cytometer is shown in figure 5.7.

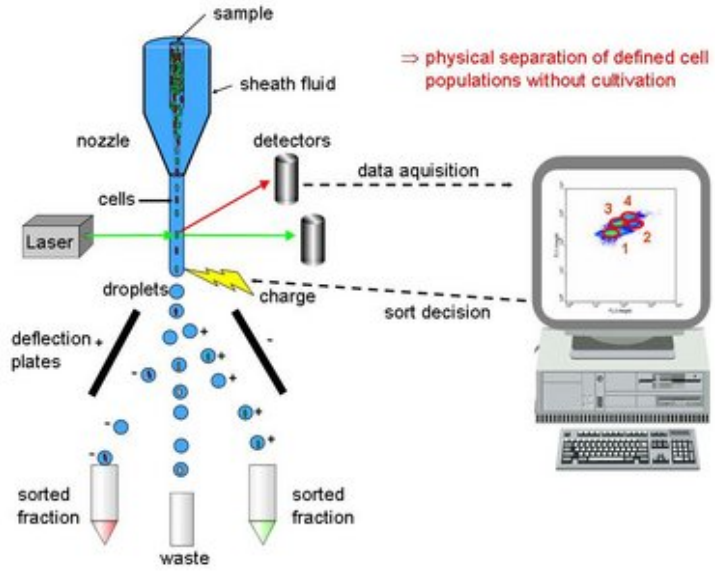

Figure 5.7: Scheme of a flow cytometer for performing cell sorting and counting analyses.

5.1.8 Gel electrophoresis

In order to analyse the macromolecules, such as ribonucleic acid (RNA), DNA and proteins, gel electrophoresis technique is used, which allows to separate them into different fragments. This separation is based upon the size and the charge of the macromolecules. There are two different type of gel: agarose and polyacrylamide. The first one is well suited to separate fragments between 0.2 Kb and 20 Kb, while the second better separate smaller fragments (< 1 Kb). Specifically, the electrophoresis gel techique allows to separate fragments which differ in only one base, leading to a higher resolution. A characteristic polyacrylamide gel is composed of acrylamide and bis-acrylamide (29:1), and contains urea, which establishes denaturating conditions. The molar ratio between acylamide and bis-acrylamide determines the size of the gel pores. Applying an electrical field, the macromolecules can move through the gel, leading to a migration of the fragments, which are negatively charged, towards the cathode (positively charged). In order to allow the fragments separation, the gel is placed into an electrophoresis chamber, in which an electrical field is applied. The heavier macromolecules move slowly than the lighter ones, leading to a separation based upon the molecular weight.

In order to analyse the proteins, a denaturating agent, the SDS is used, leading to the proteins linearization and the formation of a negative charge. This method, used in the previous analyses, is called SDS-PAGE (poly-acrylamide gel electrophoresis). In figure 5.8 is shown how a SDS-PAGE works.

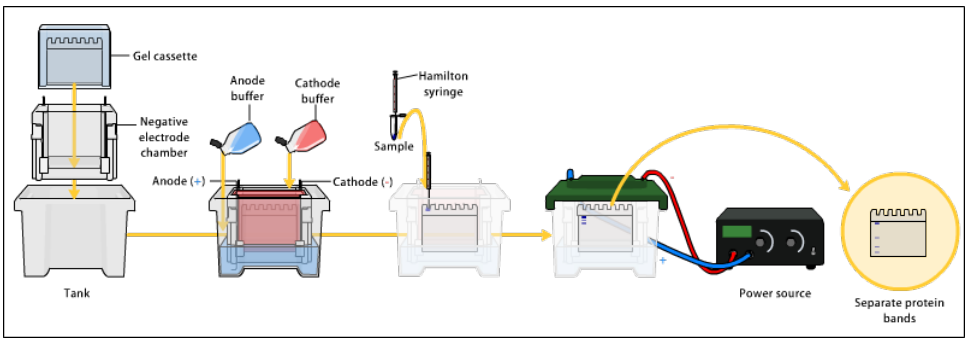

Figure 5.8: Representative scheme of a typical SDS-PAGE analysis.

Bibliography

[1] Europian Commission. *NANOTECHNOLOGIES: Principles, Applications, Implications and Hands-on Activities. A compendium for educators.* 2012.

[2] Robert a Freitas. "What is nanomedicine?" In: *Nanomedicine: nanotechnology, biology, and medicine* 1.1 (2005), pp. 2–9.

[3] Richard Feynman. "There's Plenty of Room at the Bottom". In: *Engineering and Science* 23 (1960), pp. 22–36.

[4] Shashi K. Murthy. "Nanoparticles in modern medicine: State of the art and future challenges". In: *International Journal of Nanomedicine* 2.2 (2007), pp. 129–141.

[5] P. JA. Borm. W.H.De Jong. "Drug delivery and nanoparticles: Applications and hazards". In: *International Journal of Nanomedicine* 3.2 (2008), pp. 133–149.

[6] C.M. Bhalgat S.R.Mudshinge, A.B. Deore, S. Patil. "Nanoparticles: Emerging carriers for drug delivery". In: *Saudi Pharmaceutical Journal* 19 (2011), pp. 129–141.

[7] H. Maeda J. Fang, H. Nakamura. "The EPR effect: Unique features of tumor blood vessels for drug delivery, factors involved, and limitations and augmentation of the effect." In: *Advanced Drug Delivery Reviews* 63 (2011), pp. 136–151.

[8] H. Maeda Y. Matsumura. "A New Concept for Macromolecular herapeutics in Cancer Chemotherapy: Mechanism of Tumoritropic Accumulation of Proteins and the Antitumor Agent Smancs". In: *Cancer Research* 46 (1986), pp. 6387–6392.

[9] Michael Edetsberger et al. "Detection of nanometer-sized particles in living cells using modern fluorescence fluctuation methods." In: *Biomedical and Biophysical Research Communications* 332.1 (2005), pp. 109–16.

[10] Byron Ballou et al. "Noninvasive imaging of quantum dots in mice." In: *Bioconjugate chemistry* 15.1 (2004).

[11] J. Cheng L. Tang. "Nonporous silica nanoparticles for nanomedicine application". In: *Nanoparticles for nanomedicine application* 8 (2013), pp. 290–312.

[12] L. Huang Y. ZHang, A. Satterlee. "In Vivo Gene Delivery by Nonviral Vectors: Overcoming Hurdles?" In: *The American SOciety of Gene & Cell Therapy* 20.7 (2012), pp. 1298–1304.

[13] G. Takeshi K. Kamimura, T. Suda and Zhang et Al. "Advances in Gene Delivery Systems". In: *Pharmaceutical Med.* 25.5 (2012), pp. 293–306.

[14] B.D. Ratner et al. J.M. Saul, M.P. Linnes. “Delivery of non-viral gene carriers from sphere-templated fibrin scaffolds for sustained transgene expression”. In: *Biomaterials* 28 (2007), pp. 4705–4716.

[15] José L Santos et al. “Non-Viral Gene Delivery to Mesenchymal Stem Cells : Methods , Strategies and Application in Bone Tissue Engineering and Regeneration”. In: *Current Gene Therapy* 11 (2011), pp. 46–57.

[16] Suzie Hwang Pun and Mark E. Davis. “Development of a Nonviral Gene Delivery Vehicle for Systemic Application”. In: *Bioconjugate Chemistry* 13 (2002), pp. 630–639.

[17] Gary D Luker and Kathryn E Luker. “Optical imaging: current applications and future directions.” In: *Journal of nuclear medicine* 49.1 (2008), pp. 1–4.

[18] Markus Aswendt, Joanna Adamczak, and Annette Tennstaedt. “A review of novel optical imaging strategies of the stroke pathology and stem cell therapy in stroke.” In: *Frontiers in cellular neuroscience* 8 (2014), pp. 1–10. ISSN: 1662-5102.

[19] Jean-Luc Coll. “Cancer optical imaging using fluorescent nanoparticles.” In: *Nanomedicine (London, England)* 6.1 (2011), pp. 7–10.

[20] Girish Katti, Syeda Arshiya Ara, and Ayesha Shireen. “Magnetic Resonance Imaging (MRI) âĂŞ A Review”. In: *International Journal of dental clinics* 3.1 (2011), pp. 65–70.

[21] By Hyon et al. “Inorganic Nanoparticles for MRI Contrast Agents”. In: 744 (2009), pp. 2133–2148.

[22] Z.A. Fayad D.P. Cormode, P.C. Naha. “Nanoparticle contrast agents for computed tomography: a focus on micelles”. In: *Contrast media & molecular imaging* 9 (2014), pp. 37–52.

[23] Anncatrine L. Petersen et al. “Positron emission tomography evaluation of somatostatin receptor targeted 64Cu-TATE-liposomes in a human neuroendocrine carcinoma mouse model”. In: *Journal of Controlled Release* 160.2 (2012), pp. 254 –263.

[24] Katharina Stockhofe et al. “Radiolabeling of Nanoparticles and Polymers for PET Imaging.” In: *Pharmaceuticals* 7.4 (2014), pp. 392–418.

[25] W. Stober. “Controlled Growth of Monodisperse Silica Spheres in the Micron Size Range”. In: *Journal of Colloid and Interface Science* 26 (1968), pp. 62–69.

[26] S.S. Cai Y. Geng P. Dalhaimer. “Shape effects of filament versus spherical particles in flow and drug delivery”. In: *Nature Nanotechnology* 2 (2007), pp. 249–255.

[27] Stephanie E a Gratton et al. “The effect of particle design on cellular internalization pathways.” In: *Proceedings of the National Academy of Sciences of the United States of America* 105.33 (2008), pp. 11613–8.

[28] Tian Yu, Alexander Malugin, and Hamidreza Ghandehari. “Impact of silica nanoparticle design on cellular toxicity and hemolytic activity.” In: *ACS nano* 5.7 (2011), pp. 5717–28. ISSN: 1936-086X.

[29] Norio Tsubokawa. "Surface Grafting of Polymers onto Nanoparticles in a Solvent-Free Dry-System and Applications of Polymer-grafted Nanoparticles as Novel Functional Hybrid Materials". In: *Polymer Journal* 39.10 (2007), pp. 983–1000.

[30] Mrityunjoy Kar et al. "Synthesis of Poly- L -glutamic Acid Grafted Silica Nanoparticles and Their Assembly into Macroporous Structures". In: *Langmuir* 27 (2011), pp. 12124–12133.

[31] Birgit Romberg, Wim E Hennink, and Gert Storm. "Sheddable coatings for long-circulating nanoparticles." In: *Pharmaceutical research* 25.1 (2008), pp. 55–71.

[32] Christina Graf et al. "Surface functionalization of silica nanoparticles supports colloidal stability in physiological media and facilitates internalization in cells". In: *Langmuir* 28.20 (2012), pp. 7598–7613.

[33] Hao Xu et al. "Room-temperature preparation and characterization of poly (ethylene glycol) -coated silica nanoparticles for biomedical applications". In: *Journal of Biomedical Materials Research - Part A* 66.4 (2003), pp. 870–879.

[34] Qianjun He et al. "The effect of PEGylation of mesoporous silica nanoparticles on nonspecific binding of serum proteins and cellular responses". In: *Biomaterials* 31.6 (2010), pp. 1085–1092.

[35] Yasuyuki Sadzuka et al. "Effects of mixed polyethyleneglycol modification on fixed aqueous layer thickness and antitumor activity of doxorubicin containing liposome". In: *International Journal of Pharmaceutics* 238.1-2 (2002), pp. 171–180.

[36] Joanne Manson et al. "Polyethylene glycol functionalized gold nanoparticles: the influence of capping density on stability in various media". In: *Gold Bulletin* 44.2 (2011), pp. 99–105.

[37] R.N. Zare J.V. Jokerst, T. Lobovkina and S.S. Gambhir. "Nanoparticle PEGylation for imaging and therapy". In: *Nanomedicine (London, England)* 6.4 (2012), pp. 715–728.

[38] Frank Alexis and Eric Pridgen. "Factors affecting the clearance and biodistribution of polymeric nanoparticles". In: *Molecular Pharmaceutics* 5.4 (2008), pp. 505–515.

[39] Jillian L. Perry et al. "PEGylated PRINT nanoparticles: The impact of PEG density on protein binding, macrophage association, biodistribution, and pharmacokinetics". In: *Nano Letters* 12.10 (2012), pp. 5304–5310.

[40] Vinod Babu Damodaran et al. "Conformational studies of covalently grafted poly(ethylene glycol) on modified solid matrices using X-ray photoelectron spectroscopy." In: *Langmuir : the ACS journal of surfaces and colloids* 26.10 (2010), pp. 7299–306.

[41] Mi Kyung Yu, Jinho Park, and Sangyong Jon. "Targeting strategies for multifunctional nanoparticles in cancer imaging and therapy." In: *Theranostics* 2.1 (2012), pp. 3–44.

[42] Donald E. Owens and Nicholas a. Peppas. "Opsonization, biodistribution, and pharmacokinetics of polymeric nanoparticles". In: *International Journal of Pharmaceutics* 307.1 (2006), pp. 93–102.

[43] Marina A Dobrovolskaia et al. “Preclinical studies to understand nanoparticle interaction with the immune system and its potential effects on nanoparticle biodistribution”. In: *Molecular Pharmaceutics* 5.4 (2009), pp. 487–495.

[44] Parag Aggarwal et al. “Nanoparticle interaction with plasma proteins as it relates to particle biodistribution, biocompatibility and therapeutic efficacy.” In: *Advanced drug delivery reviews* 61.6 (2009), pp. 428–37.

[45] Masoud Rahman et al. “Chapter 2- Nanoparticle and Protein Corona”. In: *Protein-Nanoparticle Interactions*. Vol. 15. Springer Series in Biophysics. Berlin, Heidelberg: Springer Berlin Heidelberg, 2013, pp. 21–45.

[46] Dmitri Simberg et al. “Differential proteomics analysis of the surface heterogeneity of dextran iron oxide nanoparticles and the implications for their in vivo clearance.” In: *Biomaterials* 30.23-24 (2009), pp. 3926–33.

[47] Pincus M.R. McPherson R.A. *Henry's Clinical Diagnosis and Management by Laboratory Methods: Expert Consult - Online and Print*. Saunders, 2011.

[48] Ashwood M.D. Burtis C.A. *Tietz Textbook of Clinical Chemistry*. Saunders, 1999.

[49] SP Boulos et al. “NanoparticleâĂŞProtein Interactions: A Thermodynamic and Kinetic Study of the Adsorption of Bovine Serum Albumin to Gold Nanoparticle Surfaces”. In: *Langmuir* 29 (2013), pp. 14984–14996.

[50] De-Hao Tsai et al. “Adsorption and conformation of serum albumin protein on gold nanoparticles investigated using dimensional measurements and in situ spectroscopic methods.” In: *Langmuir : the ACS journal of surfaces and colloids* 27.6 (2011), pp. 2464–77.

[51] “An integrated approach to the study of the interaction between proteins and nanoparticles.” In: *Langmuir : the ACS journal of surfaces and colloids* 26.11 (2010), pp. 8336–46.

[52] XJ Shi et al. “Spectroscopic investigation of the interactions between gold nanoparticles and bovine serum albumin”. In: *Chinese Science Bulletin* 57.10 (2012), pp. 1109–1115.

[53] Jinbin Liu et al. “Renal clearable inorganic nanoparticles: a new frontier of bionanotechnology”. In: *Materials Today* 16.12 (2013), pp. 477–486.

[54] S.M. Moghimi and J. Szebeni. “Stealth liposomes and long circulating nanoparticles: critical issues in pharmacokinetics, opsonization and protein-binding properties”. In: *Progress in Lipid Research* 42.6 (2003), pp. 463–478.

[55] T.M. Goppert. “Adsorption kinetics of plasma proteins on solid lipid nanoparticles for drug targeting.” In: *International journal of pharmaceutics* 302.1-2 (2005), pp. 172–86.

[56] Aaron R Folsom et al. “Serum albumin and risk of venous thromboembolism”. In: *Thromb Haemost* 104.1 (2011), pp. 100–104.

[57] Abraham Abuchowski et al. “Effect of Covalent Attachment of Polyethylene Glycol on Immunogenicity and Circulating Life of Bovine Liver Catalase *”. In: *The Journal of Biological Chemistry* 252.11 (1976), pp. 3582–3586.

[58] Voycheck C.L. Tan J.S. Butterfield D.E. “Surface modification of nanoparticles by PEO/PPO block copolymers to minimize interactions with blood components and prolong blood circulation in rats.” In: *Biomaterials* 14.11 (1993), pp. 823–833.

[59] Joseph M. DeSimone Robby A. Petros. “Strategies in the design of nanoparticles for therapeutic applications.” In: *Nature Reviews Drug Discovery* 9 (2010), pp. 615–627.

[60] Jason Park et al. “PEGylated PLGA nanoparticles for the improved delivery of doxorubicin”. In: *Nanomedicine : nanotechnology, biology, and medicine* 5 (2009), pp. 410–418.

[61] Jinlou Gu et al. “Targeted doxorubicin delivery to liver cancer cells by PEGylated mesoporous silica nanoparticles with a pH-dependent release profile”. In: *Microporous and Mesoporous Materials* 161 (2012), pp. 160–167.

[62] Gao F-Li Y. He Q. Zhang Z. “In vivo biodistribution and urinary excretion of mesoporous silica nanoparticles: effects of particle size and PEGylation.” In: *Small* 7 (2), pp. 271–280.

[63] Fangqiong Tang, Linlin Li, and Dong Chen. “Mesoporous silica nanoparticles: synthesis, biocompatibility and drug delivery.” In: *Advanced materials* 24.12 (2012), pp. 1504–34.

[64] K. PArk S. Jo. “Surface modification using silanated poly(ethylene glycol)s”. In: *Biomaterials* 21 (2000), pp. 605–616.

[65] ASTM International. *Standard Test Method for Silica in Water*. 1988.

[66] Yeoungsug Kim, Hessam Nowzari, and Sandra K. Rich. “Risk of Prion Disease Transmission through Bovine-Derived Bone Substitutes: A Systematic Review”. In: *Clinical Implant Dentistry and Related Research* 15.5 (2013), pp. 645–653.

[67] W. P. J. D. Cox C. T. Johnston Y. Wang A. M. Gillikin R. A. Palmer J. R. Schoonover Steckle Jr. *Humidity-dependent dynamic infrared linear dichroism study of a poly(ester urethane), Spectrochimica Acta Part A*. 2007.

[68] E. Bourgeat-Lami E. Duguet C. Delaite P. Dumas C. Flesch Y. Unterfinger. “Poly(ethylene glycol) surface coated magnetic particles”. In: *Macromolecular Rapid Communications* 26 (2005), pp. 1494–1498.

[69] J. Zhang et al. “On the chemical synthesis and drug delivery response of folate receptor-activated, polyethylene glycol-functionalized magnetite nanoparticles”. In: *Acta Biomaterialia* 4.1 (2008), pp. 40 –48.

[70] Ming Ma et al. “Preparation and characterization of magnetite nanoparticles coated by amino silane”. In: *Colloids and Surfaces A: Physicochemical and Engineering Aspects* 212.2âĂŞ3 (2003), pp. 219 –226.

[71] Ahmed. El-Fattah et al. "Amphiphilic methoxy poly (thylene glycol/poly-caprolactone diblock copolymers as biomaterials for methylene blue nanoencapsulation". In: *International Journal of Chemical and Applied Biological Sciences* 1.5 (2014), pp. 32–39.

[72] F. Branda et al. "Synthesis structure and stability of amino functionalized PEGylated silica nanoparticles". In: *Colloids and Surfaces A: Physicochemical and Engineering Aspects* 367.1-3 (2010), pp. 12–16.

[73] Laysan Bio Inc. *Material safety data sheet.* 2013.

[74] Kratky O. Glatter O. *Small-Angle X-ray Scattering.* Academic press, 1982.

[75] O. Navrotsky A. Rimer J.D. Trofymluk. "Kinetic and Thermodynamic Studies of Silica Nanoparticle Dissolution". In: *Chemistry of Materials* 19.17 (2007), pp. 4189–4197.

[76] B Y Ralph and Ambrose Kekwick. "THE ELECTROPHORETIC ANALYSIS OF NORMAL HUMAN SERUM". In: *Lister Institute, London* (1939), pp. 1122–1129.

[77] Eleonore Fröhlich. "The role of surface charge in cellular uptake and cytotoxicity of medical nanoparticles". In: *International Journal of Nanomedicine* 7 (2012), pp. 5577–5591.

[78] Michael Poteser and Ichiro Wakabayashi. "Serum albumin induces iNOS expression and NO production in RAW 267.4 macrophages." In: *British journal of pharmacology* 143.1 (2004), pp. 143–51.

[79] Arianna Marucco et al. "Interaction of fibrinogen and albumin with titanium dioxide nanoparticles of different crystalline phases". In: *Journal of Physics: Conference Series* 429 (2013), pp. 1–10.

Ringraziamenti

Si dice che sia il tempo che hai speso per la tua rosa, a fare della tua rosa un soggetto sí importante. Io di tempo per questa tesi ne ho speso parecchio, e non sempre é stato facile, non sempre é stato divertente, non sempre é stato leggero, ma ne é valsa la pena. Ne vale sempre la pena quando si tratta di cultura, di arricchire il proprio bagaglio personale, di imparare nuovi metodi di studio e lavoro, di mettersi in gioco. Ho imparato tanto durante questo percorso, lavorativamente ed umanamente parlando. Ho usato strumenti nuovi, cominciato ad essere un pó autonoma e, nonostante il poco tempo a disposizione, sottraendo quello del viaggio e del lavoro, sono riuscita anche a fare amicizia ed a condividere bei momenti con chi mi stava accanto. Tante sono le persone incontrate lungo questo percorso ed innumerevoli sarebbero le parole da spendere per loro.
Ringrazio il Prof. Riello, per avermi dato la possibilitá di svolgere il percorso di tesi all'interno del suo laboratorio, offrendomi il luogo adatto per poter crescere e sviluppare nuove idee. Ringrazio il Prof. Benedetti, per la collaborazione durante le analisi di SAXS, ed anche Tiziano, sempre disponibile a risolvere ogni problema.
Ringrazio il Prof. Colombatti, Giulio Fracasso e Marcella Pinto, per avermi seguita ed aiutata durante la parte svolta a Verona, per essere stati sempre presenti e disponibili per ogni chiarimento. Un ringraziamento speciale va anche alla Prof. Canton, per i suoi sorrisi e per gli incoraggiamenti lungo i corridoi di Via Torino. Ringrazio Riccardo Marin, il mio tutor, per avermi supportata e sopportata durante questo periodo, per non essersi arrabbiato quando ho maldestramento sabotato la sua reazione per poter poi salvare la mia, per avermi sovraccaricata di conti da fare e formulone da risolvere, in modo che io potessi imparare anche questo. Lo ringrazio per aver trovato il tempo di seguirmi, nonostante le innumerevoli cose da fare e talvolta anche la distanza. Ringrazio anche Gabriele, compagno di studio e paziente docente di LaTex, senza di lui probabilmente, questa tesi non avrebbe il layout che ha! Ringrazio Eleonora, per gli innumerevoli favori fatti durante questi mesi e per le piacevoli chiacchiere condivise durante le pause, per le risate, le parole di conforto e gli sfoghi. Grazie anche a Nicoló, per la pazienza nell'avermi spiegato l'utilizzo del SEM e per l'acquisizione delle immagini, ma anche Emmanuele, per le discussioni in ambito biologico, sempre costruttive. Ringrazio poi tutti coloro che hanno accompagnato questa mia esperienza, con utili consigli, idee e talvolta risate: Enrico, Michele, Gloria, Enrico, Davide, Anna, Marta, Laura, Giulia ed Irene. É probabile che io abbia dimenticato qualcuno, chiedo venia, siamo in troppi!!

Ringrazio Laura, per essersi fatta carico dei miei momenti di piú o meno pacata follia, per le merende e le grandissime risate via Skype, per il gossip che solo lei é capace di fare, e per il modo che ha di guardare alla vita: sempre sorridente ed autoironico.
Ringrazio poi i miei genitori, Maurizio ed Elisabetta, ultimi per ordine ma non per importanza. Li ringrazio per avermi permesso di studiare, di rincorrere i miei sogni, di apporre le basi per una futura carriera. Per aver sopportato i miei momenti no e la mia assenza, sia fisica che mentale, durante il periodo di tesi e la preparazione degli ultimi esami. Ringrazio anche mio fratello Gianluca, che con la sua propensione innata per qualunque attivitá in cui sia necessario l'intelletto, mi ha spronata a pretendere di piú da me stessa, e per avermi anche fatto compagnia durante le nottate passate a scrivere questa tesi!